# ATOMIC-SCALE SPECTROSCOPY AND MAPPING OF MAGNETIC STATES IN EPITAXIAL GRAPHENE

A Thesis
Presented to
The Academic Faculty

by

David L. Miller

In Partial Fulfillment
of the Requirements for the Degree
Doctor of Philosophy in
Physics

School of Physics
Georgia Institute of Technology
December 2010

# ATOMIC-SCALE SPECTROSCOPY AND MAPPING OF MAGNETIC STATES IN EPITAXIAL GRAPHENE

Approved by:


Professor Phillip N. First, Advisor
School of Physics
*Georgia Institute of Technology*

Professor Zhigang Jiang
School of Physics
*Georgia Institute of Technology*

Professor Walt A. de Heer
School of Physics
*Georgia Institute of Technology*

Dr. Joseph A. Stroscio
National Institute of Standards and Technology
*Center for Nanoscale Science and Technology*

Professor Markus Kindermann
School of Physics
*Georgia Institute of Technology*



Date Approved: 04 November 2010

*To my parents,*

*Dave and Ruth Miller.*

# ACKNOWLEDGEMENTS

I have worked with many people during my tenure at Georgia Tech. My work would not have been possible without their help and collaboration. I would first like to express my sincere gratitude to my thesis committee: Dr. Walt de Heer, Dr. Markus Kindermann, Dr. Zhigang Jiang, Dr. Joseph Stroscio and my advisor Dr. Phillip First. Special thanks to Dr. Walt de Heer and everyone in his lab: Claire Berger, Mike Sprinkle, Xiaosong Wu, Ming Ruan, Yike Hu and Holly Tinkey. Their hard work and vision is the backbone of epitaxial graphene at Georgia Tech. I also thank Joe and the crew at NIST-CNST. I appreciated the opportunity to work in his lab, and learned a lot during those months. Thanks to Dr. Edward Conrad for sharing his LEED expertise. Thanks to everyone in the graphene journal club for their insightful discussions, and specifically to Joanna Hass, Britt Torrance and Jeremy Hicks for their organizational leadership. Most importantly, I want to thank my advisor, Phil and my fellow lab mates: Greg Rutter, Joanna Hass, Nikhil Sharma, Kevin Kubista, Britt Torrance, Evan Green and Madeline Phillips.

I want to recognize the teachers and professors who inspired me in physics during my *formative* years. A big thank you to my high school physics teacher Dick Heckathorn, who made the subject seem both approachable and captivating. To my undergraduate advisor at Calvin College, Dr. Matthew Walhout, I am grateful for his guidance and personal interest in my education. And thanks to my undergraduate professor Dr. David Van Baak for sharing his passion for the field.

I also thank my friends who have supported me over these years: Adam Perkins, Jared Habeck, Daniel Borrero, Alex Wiener and Keri McCulty. Thanks to my siblings, who have always been there for me: Allison, Luke and Lillian Miller. I thank my grandparents, who have continuously expressed their pride in me and given me great confidence: my loving

grandmother Wilberta Weaver, my grammy Vivian Miller and my late grampy John Miller. Last but not least, I want to thank my wonderful parents, Dave and Ruth Miller who have always supported my academic “adventures.”

# TABLE OF CONTENTS

ACKNOWLEDGEMENTS . . . . . iv

LIST OF FIGURES . . . . . ix

LIST OF ABBREVIATIONS . . . . . xx

SUMMARY . . . . . xxii

I **Graphene** . . . . . 1

1.1 General Properties of Graphene . . . . . 1

1.1.1 Physical Properties . . . . . 2

1.1.2 Electronic Structure . . . . . 3

1.2 Graphene in a Uniform Magnetic Field . . . . . 6

1.2.1 Derivation of Landau Quantization . . . . . 7

1.3 Fabrication . . . . . 11

1.3.1 Exfoliation . . . . . 12

1.3.2 Chemical Vapor Deposition . . . . . 13

1.3.3 Epitaxial Growth on SiC . . . . . 14

II **Experimental Apparatus and Methodology** . . . . . 21

2.1 Scanning Tunneling Microscopy . . . . . 21

2.1.1 History . . . . . 21

2.1.2 Theory . . . . . 22

2.1.3 Equipment . . . . . 25

2.1.4 Topographic Imaging . . . . . 29

2.1.5 Spectroscopy . . . . . 30

2.2 Fabrication of a Digital STM Servo . . . . . 34

2.2.1 "*It's More Fun to Compute*" – Kraftwerk . . . . . 36

2.2.2 Trading Hardware for Software . . . . . 40

2.2.3 Results . . . . . 44

2.3 Python Open Source Scanning Microscopy (POSSM) . . . . . 44

2.3.1 Directory Structure . . . 45
2.3.2 Basic Operation . . . 47
2.3.3 Scan Window . . . 49
2.4 Rapid UHV Characterization and Growth Chamber . . . 50
2.4.1 Design and Operation . . . 50
2.4.2 LEED . . . 52
2.4.3 Auger . . . 53
2.4.4 RF Furnace . . . 56
III **Metrology of SiC($000\bar{1}$) Graphene using STM** . . . 63
3.1 Moiré Patterns on SiC($000\bar{1}$) Graphene . . . 63
3.1.1 Fourier Transform Analysis of Multiple Superperiods . . . 65
3.1.2 Multiple Bias Imaging . . . 68
3.2 Atomic moiré interferometry . . . 69
3.3 STS of SiC($000\bar{1}$) Graphene without a magnetic field . . . 74
IV **Scanning Tunneling Spectroscopy of Graphene in a Magnetic Field** . . . 77
4.1 Sample Treatment and Experimental Details . . . 77
4.2 Point Spectroscopy at Fixed Magnetic Fields . . . 77
4.3 Point Spectroscopy at Fixed Sample Bias . . . 82
4.4 Absence of Velocity Renormalization . . . 83
4.5 Density of States Mapping . . . 84
4.5.1 The Half-Integer Quantum Hall Effect . . . 85
4.5.2 Local Density of States in a Magnetic Field and the Quantum Hall Effect . . . 89
4.5.3 Analysis of Surface Topography . . . 90
4.5.4 Spatial Mapping of Magnetically Quantized Electronic States . . . 91
V **Concluding Remarks** . . . 112
5.1 Summary . . . 112
5.2 Further Considerations . . . 113

VITA . . . . . 135

# LIST OF FIGURES


1 Graphene atomic lattice structure. The basis vectors of a honeycomb net $\mathbf{a_1}$ and $\mathbf{a_2}$ make a hexagonal Bravais lattice with a lattice constant of $|a| = 2.46\,\text{Å}$. The red and blue dots are both carbon atoms, comprising two sublattices which are fully symmetric by inversion. Graphene sheets are principally terminated by either a zig-zag edge (edge atoms of one sublattice) or an arm-chair edge (edge atoms from both sublattices). . . . . 2

2 Graphene electronic structure. (a) Nearest neighbor tight-binding calculation for graphene ($\gamma_0 = -3\,\text{eV}, s_0 = 0.05$). The upper-left inset identifies symmetry points in the Brillouin zone, while the upper right inset shows a zoom-in of the graphene K point. At low energies near the K point, the band structure is linear (or conical in 3 dimensions), much like the energy-momentum relationships of photons and neutrinos. (b) A 3-dimensional rendering of the filled band. The Fermi surface of undoped graphene consists of a set of points at the verticies of a hexagon. . . . . 4

3 Stacking structures of graphene monolayers layers. In AA stacking, atoms from each layer stack over each other; however, the more energetically favored AB stacking of graphene layers is the common structure of graphite. AB stacking breaks the sublattice symmetry, because one sublattice always lies on top of a sublattice from the layer below, while the other sublattice overlaps the centers of the hexagons in the underlying sheet. . . . . 6

4 LL structure of $2DES_{conv}$ (left) vs. graphene (right). LLs in the $2DES_{conv}$ are equally spaced, with a gap at the center. The spectrum for graphene progresses as $\sqrt{|N|}$, centered at the Dirac point. There is a large gap between $N = 0$ and $N = \pm 1$, and the LLs get closer together at higher LL index. . . . . 10

5 Low energy electron diffraction images of graphene grown on the (a) Si face and (b) C face of SiC. Graphene on the Si face has a distinct spots graphene spots at $30^\circ$ to the SiC. The extra spots around the graphene are due to the $\left(6\sqrt{3} \times 6\sqrt{3}\right) R30^\circ$ reconstruction. Graphene on the C face shows quasi-ordered rotations with primary intensity around $0^\circ$ (a dip in intensity directly at $0^\circ$). A slight increase in intensity is seen at $30^\circ$ to the SiC spots. . . . . 14

6 Figures showing the stacking of graphene sheets with rotational domains. (a) A moiré cell at a rotation of 2 degrees. The low angle of rotation creates large areas in the film where stacking is similar to AA and AB stacking. AB stacked areas are complemented by BA stacked areas to preserve sublattice symmetry over the moiré cell. This is better seen in (b) where A and B atoms from different layers have been colored differently so that the AB/BA inversions can be easily seen as mostly red/yellow showing through from the bottom layer. . . . . 18

7 (a) ARPES measurement of graphene on SiC(000$\bar{1}$) showing the linear band structure. Bands from subsurface layers in the MEG stack can also be seen faintly and have linear bands as well due to electronic decoupling. Reprinted from [Sprinkle 2009] (b) Predicted renormalization of $c^*$ as a function of relative angle between two graphene sheets. For relative rotation angles below 5 °, the carrier velocity drops off sharply, while the higher angular rotations remain relatively unaffected. Reprinted from [Trambly de Laissardiere 2010]. . . . . 19

8 Potential applications of the field emission ultramicrometer. These include (a) a strain gauge, (b) a thermal expansion cell, (c) vibration detection and (d) a surface profile delineator. (Reprinted from [Young 1966].) (e) The surface profile delineator was later developed and named the "topografiner." [Young 1972] . . . . . 22

9 Schematic of a vacuum potential barrier when (a) the Fermi energy in the sample $E_F^S$ is equal to the Fermi energy in the tip $E_F^T$ (for materials with equal work functions), and (b) when a bias is applied $V_S$ such that $E_F$ in the tip and sample and not equal and tunneling current is generated. . . . . 23

10 Schematic of an STM tip close to a flat sample surface. Preparation of sharp tips is extremely important for obtaining atomic resolution. The lateral resolution of an STM can be approximated by the radius of the tip at the apex $R$ and the distance of the tip to the surface $d$. Reprinted from [Tersoff 1985]. . . . . 24

11 Images of the room temperature scanning tunneling microscope. (a) An exterior view of the UHV chamber. (b) A view inside the window at the actual STM device. The STM is suspended by double spring isolation for more effective high frequency damping. . . . . 25

12 Images of the NIST low temperature scanning tunneling microscope. (a) A schematic of the STM module. The entire STM is contained in a compact molybdenum cell. The sample is mounted on the bottom and approached toward the tip using a Pan-style stick-slip walker design. (b) An image of the entire STM system. The LTSTM is housed inside an acoustic enclosure and offset by air legs and an active vibration isolation system. . . . . 27

13 (a) Schematic of multiple tips causing tunneling events at the same location on the sample. This creates and artifact or "ghosting" in the image, where the same feature is seen multiple times. (b) Image is 1000 Å × 1000 Å ($V_S$ = 500 mV, $I_{set}$ = 100 pA, L_25561). Arrows point out ghosting of the same feature because of multiple tips. . . . . 29

14 (a) A sketched point $dI/dV$ spectrum. (b) When multiple point $dI/dV$ spectra are taken along a line, they can be stacked into a line scan. This gives a 2D image that contains spatial information about the point spectra. . 31

15 The stack of images in (a) comes from a grid of point spectra (b). Each point contains an entire $dI/dV$ spectrum. An individual image from the stack in (a) contains a 2D map of the local density of states at a discrete energy. . . . . 33

16 A diagram of a typical analog servo. The tunneling current is internally amplified (current → voltage, 0.1 V/$nA$) by the preamp and amplified again outside the system by the Stanford preamp. The rectifier takes the absolute value of the voltage to remove the sign of the current, determined by the sign of the bias. The log amplifier linearizes the signal before passing it to the feedback loop. The precision reference provides a stable voltage to control the tunneling current setpoint $I_{set}$, and the error voltage for the feedback loop is generated as the difference between the reference and signal. The output of the feedback loop is added to the offset voltage and amplified. Finally the resulting voltage is applied to the z-piezo to control the height of the tip. . . . . 35

17 A diagram of a typical digital servo. Most of the components from the analog servo can be implemented in software. The digital servo has a digital signal processor (ADSP-21369) to handle the signal from the STM. An ADC-1672 analog-to-digital converter digitizes the current and the logarithm is computed in software by the DSP. The feedback is calculated from a software PID loop with gains that are adjustable on the fly. Three DAC-9881 digital-to-analog converters are on board for generation of an output signal. Two of them are summed with different gains for a high and low gain scan mode. . . . . 36

18 Scanning the tip over atomic corrugation creates a sinusoidal modulation of the tunneling current. The frequency of the oscillations define a maximum input-to-output latency for the entire servo before the servo response is 180° out of phase. This is important to consider when choosing digital converters as many high resolution audio converters have very high associated filter latencies. . . . . 38

19 The main interface of POSSM. The scanning software is laid out in a notebook-style arrangement. Additional pages are opened when new scans begin. This client interface connects to a computer running the controller software so that scans can be run remotely from any computer, without the need to install hardware drivers. . . . . 48

20 The interface for the viewer and scan window. On the right side of the window, there are many tools available for image processing and data analysis. Most importantly, one can do line and plane subtraction while scanning, adjust the z-height based on a histogram of the image and take height profiles of the surface. . . . . 49

21 An image of the rapid characterization chamber. Samples are transferred into the system through the load locks (lower right area, not visible). The double load-lock design greatly reduces the transfer time into UHV from ~1 day (for single load lock systems) to ~1 hour. The magnetically coupled linear-rotary feedthrough transfers samples into the main chamber, where they can be characterized by using LEED and AES. If samples require heating or growth, they can be moved further into the RF induction furnace (upper left). . . . . 50

22 (a) An image of the LK LEED/Auger system. At the top are the grids. The electron gun is in the center of the spherical grids. The whole device can be translated to set the sample at the center of the grid sphere. In LEED mode, electrons are diffracted off of the surface. The voltage on $G_{23}$ filters the inelastically scattered electrons so that the diffraction pattern stands out on the phosphor screen. Similarly, $G_{23}$ in Auger mode acts as a high pass filter; however higher energy electrons from the gun knock out core electrons from atoms at the surface. Ionized atoms become doubly-ionized when the relaxation of higher level electrons drop to fill the vacant core-level state and a higher level Auger electron is knocked out. The detection of these events produces peaks in the collected current which are chemically sensitive. (b) A schematic of the LEED/Auger with typical operating voltages. The same equipment that is used for LEED can be operated with different voltages as a retarding field analyzer (RFA) Auger electron spectroscopy system. . . . . 52

23 An screenshot of pyAES, Auger control program. The large Auger peak shown is a graphitic carbon peak. The program interfaces with a data aquisiton card which controls and measures the AES signal from the control electronics. . . . . 55

24 (a) An image of the graphite sample holder. Green and red stars mark where Auger scans were taken in (c) and (d) respectively. The gray part at the back of the sample holder is molybdenum which was evaporated from the furnace suscepter. (b) A reference scan on a piece of molybdenum. (c) An Auger scan on the back of the sample holder showing molybdenum evaportion on the back. (d) An Auger scan on a clean graphite region. . . . 57

25 Calculated and actual power losses in the all-graphite furnace. At lower temperatures, the furnace loses efficiency mostly from conduction, but as the temperature, $T$, is increased in the furnace, the $T^4$ dependence of the blackbody radiation becomes the primary source of power dissipation. The predicted power losses diverge slightly from the actual at low temperatures. Conductive losses are significantly more difficult to predict. . . . . 60

26 An image of the pyTherm interface. The temperature of the furnace can be monitored two different ways (type C thermocouple and infrared pyrometer). The pressure is recorded during heating, and the maximum pressure can be set on the interface (so that the ion pump does not shut off). The interface has several heating stages which can be set. The temperature is controlled through a custom hybrid algorithm of PID feedback and a calibration curve. Plots of the pressure, temperature and supply current are simultaneously displayed as a function of time. . . . . 62

27 A few moiré patterns observed in STM on multilayer epitaxial graphene. (a) A 200 Å × 200 Å image with a "double moiré" and atomic corrugation visible at the fine scale ($V_S$ = 350 mV, $I_{set}$ = 100 pA, L_23543). (b) A 500 Å × 500 Å image, showing a low-angle grain boundary in a subsurface layer. The top layer is continuous (from atomic scale images), but a change of stacking in a subsurface layer causes the pattern to change ($V_S$ = 200 mV, $I_{set}$ = 100 pA, L_25987). (c) A 1500 Å × 1500 Å image showing the large, continuous spatial extent of the pattern ($V_S$ = 300 mV, $I_{set}$ = 100 pA, L_23470). (d-f) Height profiles from images in (a-c). . . . . 64

28 STM topographs of two moiré patterns on multilayer epitaxial graphene ($V_S$ = 0.5 V, $I_{set}$ = 100 pA). (a) Two similarly-sized moiré patterns interfering, resulting in a large superlattice unit cell. Layers 1 (surface layer) and 2, and layers 2 and 3 have comparable rotation angles in opposite directions (shown schematically in d). (b) High resolution image of a region in (a). (c) FT of (a). (d) Schematic of layer orientations based on the moiré pattern shown in (a, L_24336) and (b, L_24318). (e, L_25598) STM image of a different moiré superlattice. (f, L_25606) High resolution image from within the same area. (g) FT of (e). Spots on the dotted circle result from the interference of two moiré patterns (three graphene layers). The top-layer atomic reciprocal lattice from a FT of (f) determines which spots correspond to the moiré formed from layers 1 and 2 (see Eq. 48). (h) schematic of layer orientations based on the moiré pattern in (e). . . . . 66

29 Multibias imaging on the moiré pattern in Figure 28a. Each image is 5 nm × 5 nm, and was taken at the same spatial location and tunnel current (100 pA). In (a, L_24048), only the moiré pattern of the top two layers is imaged. (b, L_24044), (c, L_24045) show the transition as the tip moves closer to the surface. In (d, L_24047), the tip has pushed in far enough to only image the lower layer moiré pattern. We believe that by $V_S = -0.05$ V, the tip is actually in contact with the surface. . . . . 68

30 (Color online) Strain induced between two stacked hexagonal (real space) lattices in the case where one lattice (black/dashed line) is (a) stretched but not rotated and (b) stretched and rotated with respect to the undistorted lattice (blue/solid line). (c) displays equal strain for both lattices. For rotated lattices under relative strain, the angular change in the lattice vectors affect the interference pattern differently for each direction. As a result, the moiré pattern observed in STM will appear stretched or distorted. Significantly higher strain is required for similarly sized distortions if the lattices are equally strained along the same direction. At the low moiré angles ($\theta$), the lattice vectors (when equally strained) will obtain similarly sized angular distortions $\varphi_i$ which will nullify each other. . . . . 69

31 (Color online) Curves display the length distortion between two vectors of the moiré cell as a function of the moiré rotation angle $\theta$. The amount of distortion for a small strain rapidly increases with decreasing moiré rotation angles (i.e. when the rotation angle is comparable to the angular distortion, $\theta \sim \varphi$). . . . . 71

32 (Color online) (a, L_25800) STM image demonstrating the effect of strain on the moiré superlattice ($V_S = 0.35$ V, $I = 100$ pA). (b) FT of the image in (a). Five sets of moiré spots can be identified, requiring interactions from at least 4 layers. Strain may be caused by subsurface low-angle grain boundaries [marked approximately with green lines in (a)] or by nearby "pleats." . . . . 72

33 (Color online) (a) Large-area AFM image showing pleats; i.e., folds in the stacked graphene layers. Pleats tend to run along the SiC step or perpendicular to them. (b, L_25218) Atomically-resolved STM image on the top of a pleat. Tunneling conditions were $V_S = 350$ mV, $I_{set} = 100$ pA. (c) Schematic of a pleat in epitaxial graphene. Mismatches in the thermal contraction after growth can induce buckling of the graphene lattice causing pleats to form. . . . . 73

34 (a) Band structure of two twisted bilayers. For two (decoupled) AA stacked sheets, the Dirac cones line up on top of one another. As the layers are twisted toward 30 °, the bands spread apart in k-space. If there is interaction between layers, the crossing points cause band repulsion which modifies the band structure. (b) A fit to the model of the energy separation between the Van Hove singularities (Reprinted from [Li 2009a]). . . . . 74

35 (a) A double moiré pattern on MEG. Supercells are marked in blue (∼ 4.8 nm) and purple (∼ 8.3 nm) in the 400 Å × 400 Å image (L_23915). The blue line shows a (b) height profile with modulations due to the superperiodicity. (c) A $dI/dV$ spectrum taken from the center of the image in (a), showing Van Hove—like peaks in the density of states. The energy gap between the peaks as marked are $\Delta E_1 = 64\,\text{meV}$ and $\Delta E_2 = 202\,\text{meV}$. Tunneling conditions were $V_S = 0.5\,\text{V}$, $I_{set} = 100\,\text{pA}$. . . . . 75

36 (a) A simulation of the LL structure in graphene (dark color represents high density of states). The dotted line shows the location of density of states profiles taken along the (b) energy direction and (c) magnetic field direction. Peaks seen in (c) are a result of the LL passing through the sample bias $V_S$, resulting in an increase in the density of states. . . . . 78

37 (a) dI/dV scan of MEG in a strong magnetic field ($B = 5\,\text{T}$). (b) The LL structure linearizes with $sgn(N)\sqrt{|N|B}$ as expected. When interlayer coupling is included ($\gamma_1$, black and blue lines), the data is not well fit, implying that the top layer has completely decoupled. . . . . 79

38 (a) $dI/dV$ measurements at 1 T intervals. The curves are offset vertically so that they can be easily seen. (b) A linearization of the data from (a). The slope of the light blue fit line gives the the carrier velocity as $c^* = 1.128 \pm 0.004 \times 10^6\,\text{m/s}$. The inset shows the energy variation of $LL_0$ as a function of magnetic field. . . . . 81

39 (a) A $dI/dV$ measurement at a fixed sample bias $V_S = -65\,\text{meV}$. The magnetoconductance oscillates due to the passing of LLs through the tunneling bias. (b) A reconstruction of the low-energy band structure using TMCO measurements. If a circular cross-section is assumed, spectroscopy measurements can reproduce the energy band structure. Data is symmetrized about the $k = 0$ line. (c) A schematic of the conical graphene band structure in a magnetic field. The application of a perpendicular magnetic field forms discs (circles) due to LL formation. The red dotted circle represents the energy of the tunneling bias. As the magnetic field is increased, the LLs move through the circle, creating peaks in TMCO measurements. . . . . 82

40 (a) A 3.8 nm moiré pattern (L_23626). (b) A line scan through the center of the image, showing the largely $\sqrt{|N|B}$ dependence of the spectra. Spectra are unaffected by the position of the tip relative to the moiré pattern. (c) Averaged spectra from (b). The inset shows the linearization of the LL peaks when plotted vs. $\sqrt{|N|B}$. The slope yields a value of $1.13 \pm 0.07 \times 10^6\,\text{m/s}$. Spectra shows interesting negative differential conductivity at the edge of the LLs. This feature is occasionally observed when the tip is very sharp. Tunneling conditions for (a,c) were $I_{set} = 100\,\text{pA}$, $V_S = 300\,\text{mV}$. . . 84

41 (a) A schematic of a six terminal quantum Hall device. Terminals 1 and 4 provide the current that travels along the edges when $E_F$ is between LLs (marked by arrows). The direction of the current is determined by the magnetic field. As shown, the magnetic field would be directed into the page. The longitudinal resistivity $\rho_{xx}$ is measured between 2 and 3 or 5 and 6, while the Hall conductivity is measured between 2 and 6 or 3 and 5. (b) Quantum Hall measurement on carbon face epitaxial graphene (reprinted from [Wu 2009]). . . . . 85

42 (a) In a magnetic field, the size of wavefunctions are on the order of the magnetic length. As the magnetic field ($B_i$) increases, the wavefunction size decreases. As a result, the wavefunction can more deeply probe hills and valleys in the electrostatic potential. (b) Localized and extended states in a inhomogeneity broadened Landau level. . . . . 86

43 (a) The Landau level structure of graphene as a function of energy and magnetic field. The Fermi energy is shifted off of the Dirac point (and $LL_0$) either by using a back gate or from doping. LLs disperse to higher energies as the magnetic field is increased. When the magnetic field is set so that $E_F$ is between LLs, the graphene is in a localized state. Electrons at $E_F$ cannot traverse the sample due to localization around extrema in the electrostatic potential and must travel along the edge as in (b). Because of this, the longitudinal resistivity $\rho_{xx}$ drops. The crossing of a LL through $E_F$ reduces the filling factor $\nu$ (the number of filled LLs *times* the degeneracy). This increases the Hall resistivity $\rho_{xy}$ by quantized amounts and produces plateaus, (d) blue line. During this transition, the graphene is in an extended state, as in (c). The current follows saddle-point equipotentials in the sample and connects the terminals at contacts on opposite sides. Electrons drift along equipotential lines (yellow lines) while spinning in cyclotron motion (black spirals). . . . . 87

44 Topographic STM images of the multilayer epitaxial graphene sample grown on SiC. (a, L_25082) A 100 nm × 100 nm real-space image of the surface studied, taken at a sample bias of $V_s = 0.35$ V and a tunnel current $I_s = 400$ pA. This image was acquired simultaneously with the 8 T $dI/dV$ maps shown in Fig. 46. Periodic height variations are a moiré pattern of $\approx 4$ nm period. A defect at bottom-center distorts the topograph due to an electronic perturbation. Arrows label the line corresponding to the spectral profiles of Fig. 52. (b, L_24993) A 5 nm × 5 nm image ($V_s = 0.10$ V, $I_s = 100$ pA, $x, y$ sampling increment 25 pm) showing the atomic lattice. c) A height profile showing the topographic variations in (a). The line cut goes through a defect at the lower/center part of the image in (a). The sample surface is very smooth with variations tip height due to the moiré pattern on the order of 10 pm RMS. . . . . 91

45 Spectra of $LL_0^{av}$ at magnetic fields of 4 T, 6 T and 8 T averaged over the area in Fig. 44a. Energy is $eV_s$, where $V_s$ is the sample voltage bias. Labels at marked energies (open circles) correspond to the displayed maps. The energy spacing between points is 4 meV, and the energy of the peak for $LL_0^{av}$ is labeled *#3* for each magnetic field spectra. Each number corresponds to a map which is displayed in Fig. 46. Lines are spline interpolants of the raw data (filled circles). . . . . 92

46 Spatial local density of states measurements at energies around $LL_0^{av}$ showing the extended states at the $LL_0^{av}$ peak energy and localized states at energies above and below the peak energy. Each row is a set of four maps at a single magnetic field and each column (1-4, marked in Fig. 45) are chosen at comparable energies along $LL_0^{av}$ for each magnetic field. STS $dI/dV$ maps of the 100 nm × 100 nm region are displayed for magnetic fields of 4 T (top row, L_25094), 6 T (middle row, L_24875), and 8 T (bottom row, L_25084). These maps (taken from a larger data set) were selected at energies bracketing $E_0^{av}$ for each magnetic field (note that areas probed at different fields are not in exact registry; the defect position can be used as an alignment guide). The magnetic lengths ($\ell_B$, shown in the right most column) correspond to values of 13 nm,10.5 nm and 9 nm, respectively. Following the maps down columns shows that $dI/dV$ features sharpen due to decreasing $\ell_B$. Left to right across rows, the maps show the change from states localized in potential energy minima, to extended states at $E_0^{av}$, to states localized around potential energy maxima (note the inversion of $dI/dV$ intensity from $E_0^{av} - 4$ meV to $E_0^{av} + 4$ meV). Rings at upper-left in columns (1) and (2) can be viewed as tracing equipotential lines that differ by 4 mV. At energy $E_0^{av}$, the drift state follows an equipotential that may span the sample. In 6 T and 8 T maps, patches with large pixel-to-pixel intensity variation appear. . . . . 94

47 Cross-correlation maps for magnetic fields of (a) 4 T and b) 8 T (energy range is the same for both maps, $dI/dV$ spectra shown above each map). Both planar axes are $dI/dV$ energy, and each pixel of the cross-correlation map represents the normalized cross-correlation of two $dI/dV$ maps at energies $E_i$ and $E_j$. Blue represents maps of high correlation, while red represents anti-correlation. The solid blue diagonal line is the cross correlation of maps with themselves (representing maximal correlation). The map in (b) has dashed lines drawn to indicate where $LL^{av}$ peaks occur. The intersection of two LLs always has the same structure: high correlation in directions parallel to the center-diagonal, and anti-correlation in directions which are perpendicular. This behavior is described in (c). The correlation of maps on the same side of any two LLs have a high correlation, while the correlation of maps on opposite sides are anti-correlated. This behavior is expected within the drift state localization picture. . . . . 96

48 Multifractal analysis of the maps shown in Fig. 46 (8 T only) (a) A plot of the numerator vs. the denominator equation 67, the fractal dimension $\alpha$, for various values of q. Similar plots are used for $f(q)$, and the slopes of the fit lines are used to plot $f(\alpha)$. (b) The resulting plot of $f(\alpha)$ for various maps around $E_0^{av}$. The apex of the parabolic curve at the center of $LL_0^{av}$ gives a value of the scaling parameter $\alpha \approx 2.0$. . . . . 98

49 Small scale fluctuations seen in the raw $dI/dV$ data acquired at a magnetic field of 8 T. Images were taken (a) at 52 meV, $\approx$ 4 meV below the $LL_0^{av}$ peak (see Fig. 45), and (b) at 60 meV, $\approx$ 4 meV above the $LL_0^{av}$ peak. In (a)/(b), zero differential conductance is shown as black and the maximum differential conductance of 5 nS is red/green. (c) The sum of red and green images in (a) and (b). The speckled patch marked by a white box is shown expanded in (d). . . . . 101

50 Maps of $E_0(x, y)$ for magnetic fields (a) 4 T, (b) 6 T, (c) 8 T. In (a) there are no apparent small scale fluctuations. As the field is increased in (b) and (c), the fluctuations in the peak of $LL_0$ become apparent. The influence of inhomogeneities is also apparent in this map. In (c), over much of the area, $E_0$ varies smoothly, reaching a maximum at the position of the defect seen in Fig. 44a (omitting the defect core). A second maximum (top-right) and a minimum (top-center) could be due to unresolved defects. Several speckled patches can be seen, where $E_0$ varies over distances shorter than the 0.4 nm sampling distance. . . . . 102

51 Closer inspection of Fig. 50c. (a) The $E_0$ tracking map for 8 T. (b) Expanded view of the speckle displaying large pixel-to-pixel variations of $E_0$. (c) Histograms of $E_0$ values from boxes I & II in part (a). In the speckled patch I, the histogram (top) has two distinct peaks (A & B) separated by 6 meV. A single peak is found in the bottom histogram from unspeckled region II. (d) Average $dI/dV$ spectrum obtained from pixels in the high-count bin (52.5 meV $< E_0 <$ 52.75 meV) under histogram peak A (blue) and from pixels in the high-count bin 58.5 meV $< E_0 <$ 58.75 meV) under peak B (green). We associate these with the valley-split $LL_0$ LDOS on sublattices A and B. . . . . 103

52 Magnetic field dependence of the spatially varying $LL_0$ peak energy. $dI/dV$ magnitude (color) versus energy (vertical) and position (horizontal) along the line marked by arrows in Fig. 44a. The yellow arrows in Fig. 44a correspond to the location of the line cuts in (a-c), while the green arrows correspond to the location of the line cuts in (d-f). The spectral profiles were extracted from $dI/dV$ maps at (a,d) 4 T, (b,e) 6 T, and (c,f) 8 T. The bright $dI/dV$ peak is $LL_0$. Within a speckled patch (centered at 35–40 nm in d-f), an energy gap is observed for fields above 4 T. The $dI/dV$ intensity of the two bands is anticorrelated: At any spatial position (pixel), large $dI/dV$ in one band corresponds to small $dI/dV$ in the other. Note that the $\approx 5$ nm intensity modulation of the bands is an aliasing artifact due to undersampling of the graphene lattice. . . . . 104

53 Gap maps ($\Delta(x, y)$) for magnetic fields of (a) 4 T, (b) 6 T, (c) 8 T. The quasi-hexagonal figures in (b) and (c) are identical. Note that maps at different magnetic fields are not in exact registry; the defect (bottom-center) can be used to judge positional displacement between maps. . . . . 105

54 The 8 T gap map of Fig. 53c (black outline) shown on top of the same map shifted in position by a superlattice period (white arrow). This illustrates that the positions of the gaps at the edges of the map are consistent with a continued hexagonal distribution. . . . . 106

55 (a) Model of the moiré alignment of two graphene sheets. The top model layer (green) is aligned with the sample crystallographic axes, but the atomic unit cell is larger for illustration. The second model layer (blue) is slightly rotated with respect to the top layer and strained uniaxially by 0.25%. The model shows that the observed quasi-hexagonal symmetry in Fig. 53 follows naturally from a large moiré superlattice with small relative strain [Miller 2010a]. The valley-split patches in Fig. 53(b,c) correspond to AB/BA patches in the model. Since this large moiré superlattice is not seen in the topography, the energy gaps are most likely a consequence of interaction between the first (top) and third graphene layers. (b) Schematic of an orientation of the top three layers that would produce the observed short-period (STM) and long-period (STS) moire patterns. . . . . 109

56 (a) Schematic wavefunctions of $LL_0$ in graphene. A and B label the sublattice atoms; blue denotes states from the $K_+$ valley of the graphene Brillouin zone and green corresponds to states from the $K_-$ valley. (b) Schematic of $LL_0$ states at the $K_\pm$ points with zero potential difference between sublattices (zero staggered potential). (c) $LL_0$ states at the $K_\pm$ points with nonzero staggered potential. . . . . 111

# LIST OF ABBREVIATIONS

| Abbreviation | Description |
|---|---|
| STM | scanning tunneling microscope/microscopy |
| STS | scanning tunneling spectroscopy |
| RTSTM | room temperature scanning tunneling microscope |
| LTSTM | low temperature scanning tunneling microscope |
| RCC | rapid ultra-high vacuum characterization chamber |
| AFM | atomic force microscope/microscopy |
| DFM | dynamic force microscopy |
| LEED | low energy electron diffraction |
| AES | Auger electron spectroscopy |
| UHV | ultra-high vacuum |
| TSP | titanium sublimation pump |
| 2DES | 2-dimensional electron system |
| LDOS | local density of states |
| ML | monolayer |
| MEG | multilayer epitaxial graphene |
| HOPG | highly oriented pyrolytic graphite |
| $2DES_{conv}$ | conventional 2-dimensional electron system |
| LL | Landau level |
| $LL_0$ | Landau level with index ($N = 0$) |
| $LL^{av}$ | spatially averaged Landau level |

| Abbreviation | Description |
|---|---|
| TMCO | tunneling magneto-conductance oscillations |
| SdHO | Shubnikov de Haas oscillations |
| DSP | digital signal processor |
| PID | proportional integral and derivative feedback loop |
| RF | radio frequency |
| RMS | root-mean-square |

# SUMMARY

The unique electronic structure of single layer graphene stems from its strong in-plane bonds and unperturbed out-of-plane $\pi_z$ orbitals. The ideal low-energy linear band structure is only realized for a truly free-standing sheet of graphene where the $\pi_z$ orbitals cannot interact with nearby atoms. This poses a significant challenge to the future of graphene based electronics. Any material to be used commercially should be mechanically robust and scalable, neither of which describes exfoliated suspended monolayers of graphene. It is, however, possible to choose a substrate which minimizes interactions, permitting an electronic band structure similar to that of an isolated single layer.

Single or multilayer graphene samples can be grown on either the (0001) or (000$\bar{1}$) faces of a SiC crystal. When SiC is heated, the crystal structure thermally decomposes. The silicon preferentially evaporates, leaving behind carbon atoms which reform into graphene sheets. Unlike graphite which contains bulk stacking in Bernal configuration, the graphene layers grown on SiC (000$\bar{1}$), called multilayer epitaxial graphene (MEG), stack in quasi-ordered rotations that preserve lattice symmetries over the superlattice unit cell and produce larger interlayer spacings. This material was first recognized to behave like a stack of decoupled graphene layers based on magnetotransmission infrared experiments.

To investigate the electronic properties, I use a cryogenic ultra-high vacuum scanning tunneling microscope (STM). Spectra of the local differential conductance are collected by fixing the tip-sample distance and sweeping the bias voltage. Using a lock-in amplifier to modulate the sample bias, the resulting signal ($dI/dV$ vs. $V$) is obtained. This technique (also called scanning tunneling spectroscopy or STS) provides information about the local density of states (LDOS), and when combined with a magnetic field, can be used to map the band structure, measure Landau levels (which give rise to the quantum Hall effect),

map the quantum Hall states to identify broken degeneracy, and measure the electrostatic potential fluctuations.

# CHAPTER I

# GRAPHENE

## *1.1 General Properties of Graphene*

Graphene is often described as a "chicken wire" of carbon atoms or 2-dimensional graphite. The single sheet of hexagonally arrayed carbon atoms yields many fantastic properties which make it an interesting candidate for study and application. Recently, graphene has been demonstrated as a transparent conductor to replace indium tin oxide (ITO) in touch-screen displays and in flexible organic light-emitting diode (OLED) displays. The transmittance of visible light in graphene is greater than 97.7% [Nair 2008], while the resistivity is very low [Chen 2008]. In the short term, graphene may prove most useful as a transparent conductor and as interconnects to replace copper in microchips; the zero-gap band structure of pristine graphene stands in the way of it replacing gapped semiconductors in transistor devices.

However, great strides have been achieved in demonstrating its potential for use in other electronic devices. Groups at Georgia Tech and IBM have successfully shown that epitaxially grown graphene can be used for radio frequency transistors at frequencies higher than 100 GHz . This is already faster than current high-end silicon RF transistors which top out around 40 GHz (though 500 GHz devices have been demonstrated [Krithivasan 2006]). Such discoveries should interest the telecom industry, as these transistors are mostly useful in amplifying antenna signals. Many more applications are also expected, stemming from its flexibility, high carrier mobility and long spin lifetimes. Indeed, one of the most incredible attributes of graphene is that these properties persist even at room temperature.

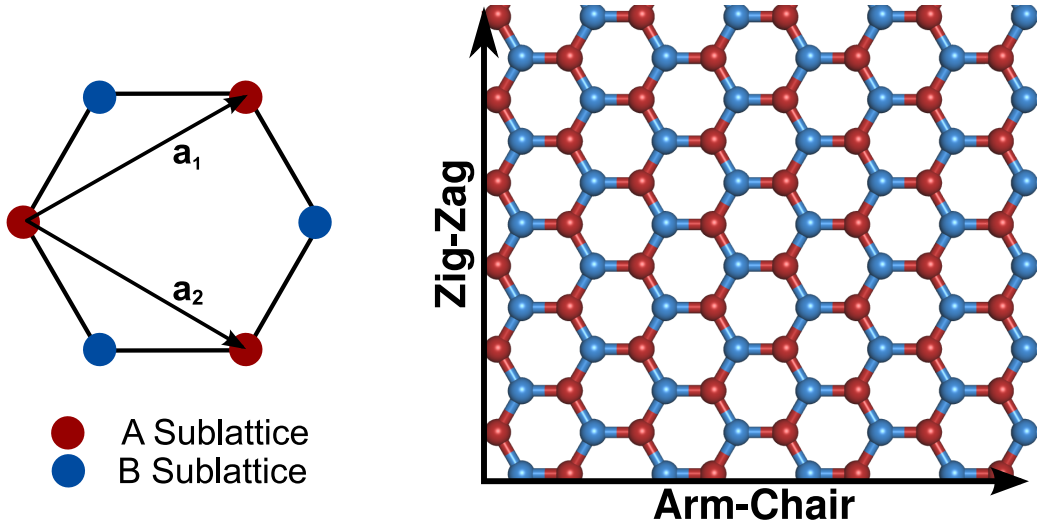


Figure 1: Graphene atomic lattice structure. The basis vectors of a honeycomb net $\mathbf{a_1}$ and $\mathbf{a_2}$ make a hexagonal Bravais lattice with a lattice constant of $|a| = 2.46$ Å. The red and blue dots are both carbon atoms, comprising two sublattices which are fully symmetric by inversion. Graphene sheets are principally terminated by either a zig-zag edge (edge atoms of one sublattice) or an arm-chair edge (edge atoms from both sublattices).

### 1.1.1 Physical Properties

The graphene unit cell is made up of two carbon atoms, spaced by 1.42 Å. In plane, each carbon atom is connected to three other carbon atoms by $\sigma$ bonds ($sp^2$ hybridization of the $2s$, $2p_x$ and $2p_y$ orbitals). The atoms are strongly bonded, with an atomic coupling of $\gamma_0 \approx -3.0\,\text{eV}$ [Wallace 1947]. Such strong bonding is primarily the reason graphene has been measured as the stiffest planar material to date [Lee 2008]; nonetheless, graphene bends easily in response to out of plane stresses making it also very flexible. Such flexibility permits graphene sheets to easily conform to the substrate it is placed on, an attribute that has proved quite significant to the resulting electronic structure [Lui 2009, Lundeberg 2010]. Perpendicular to the plane, the ideal graphene sheet has unperturbed $\pi$ orbitals which are highly important to the electronic structure; the $\pi$ bands cross at the Fermi energy $E_F$, making them primarily responsible for the unique conduction characteristics. Because the orbitals that most affect the electronic structure near the Fermi energy are oriented out of the plane of the sheet, preservation of the ideal properties of

graphene requires careful substrate selection. Interactions with a substrate cause the band structure to deviate from ideal graphene.

Two-dimensional honeycomb structures can be represented as hexagonal Bravais lattices using a two-atom basis [Ashcroft 1976]. The two basis vectors can be chosen to connect the verticies of one triangular sublattice, separated by an angle of 60° (Fig. 1a). The basis vectors for graphene can be written:

$$\begin{aligned} \mathbf{a_1} &= \frac{a}{2}(\sqrt{3}\hat{\mathbf{x}} + \hat{\mathbf{y}}) \\ \mathbf{a_2} &= \frac{a}{2}(\sqrt{3}\hat{\mathbf{x}} - \hat{\mathbf{y}}), \end{aligned} \tag{1}$$

where $a$ is the lattice constant 2.46 Å. These vectors translate into the reciprocal space vectors:

$$\begin{aligned} \mathbf{b_1} &= \frac{2\pi}{a}(\frac{1}{\sqrt{3}}\hat{\mathbf{x}} + \hat{\mathbf{y}}) \\ \mathbf{b_2} &= \frac{2\pi}{a}(\frac{1}{\sqrt{3}}\hat{\mathbf{x}} - \hat{\mathbf{y}}). \end{aligned} \tag{2}$$

The two triangular Bravais *sub*lattices of graphene are symmetrically identical by inversion (the red/blue atoms in Fig. 1b make up two identical triangular sublattices). The nature of this structure and its symmetries give graphene its distinctive electronic structure.

### 1.1.2 Electronic Structure

The electronic properties of graphene are unlike that of conventional 2-dimensional electron systems ($2DES_{conv}$). The low-energy band structure is analogous to that of a massless neutrino near the $K_+$ and $K_-$ points of the Brillouin zone ($E = pc^*$, where $c^*$ is the velocity of charge carriers). Electrons in graphene obey the Dirac-Weyl equation [DiVincenzo 1984, Semenoff 1984], meaning they are massless and travel with constant group velocity [Miller 2009]. The band structure that describes the dynamics of electrons in graphene can be calculated within a simple nearest neighbor tight-binding approximation. The result gives an analytic solution to the $\pi$ band structure, which reasonably matches

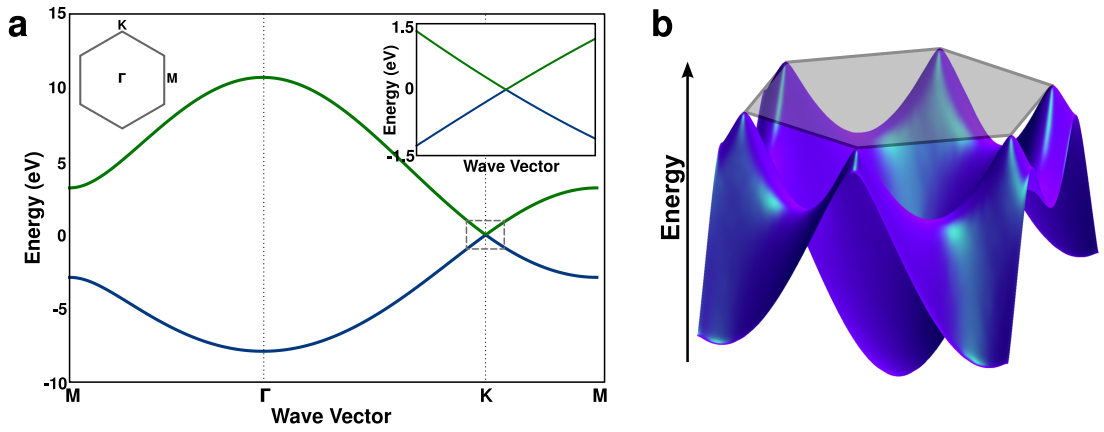


Figure 2: Graphene electronic structure. (a) Nearest neighbor tight-binding calculation for graphene ($\gamma_0 = -3\,\mathrm{eV}, s_0 = 0.05$). The upper-left inset identifies symmetry points in the Brillouin zone, while the upper right inset shows a zoom-in of the graphene K point. At low energies near the K point, the band structure is linear (or conical in 3 dimensions), much like the energy-momentum relationships of photons and neutrinos. (b) A 3-dimensional rendering of the filled band. The Fermi surface of undoped graphene consists of a set of points at the verticies of a hexagon.

more exact calculations. The energy bands from the nearest neighbor tight-binding calculation are [Reich 2002, Wallace 1947]:

$$E(k_x, k_y) = \pm\gamma_0 \sqrt{1 + 4\cos\frac{\sqrt{3}k_x a}{2}\cos\frac{k_y a}{2} + 4\cos^2\frac{k_y a}{2}} \tag{3}$$

Figure 2a shows a plot of the valence and conduction bands in graphene along lines through the Brillouin zone. The 3-dimensional plot of the conduction band is shown in Fig. 2b. The Fermi surface consists of the $K$ points in a hexagonal arrangement. If we Taylor expand $E$ around one of the $K$ points ($K = \frac{4\pi}{3a}\hat{\mathbf{y}}$) via the substitution $E(\mathbf{k}) \rightarrow E(\mathbf{K} + \mathbf{k})$ (continuum limit), then for small $\mathbf{k}$ around $\mathbf{K}$ ($|\mathbf{k}|a \ll 1$) we find that the energy band is linear in $\mathbf{k}$:

$$E(\mathbf{K} + \mathbf{k}) = \pm\frac{\sqrt{3}}{2}\gamma_0 a|\mathbf{k}|. \tag{4}$$

For this reason, the band structure around $E_F$ is commonly referred to as the *Dirac cone*. The crossing point of the $\pi$ valence and $\pi^*$ conduction bands at zero energy is known as the *Dirac point*, and the velocity of electrons (carrier velocity, $c^*$) is taken from the slope of the energy-momentum relation $c^* = \sqrt{3}\gamma_0 a/2\hbar \approx 10^6\,\mathrm{m/s}$. A zoomed in view of the low energy bands at the $K$ point is shown in the inset of Fig. 2a. At higher $\mathbf{k}$

values, cross sections of the band structure become triangular (rather than circular). This is commonly referred to as *trigonal warping*, but this effect is fairly insignificant within an electron volt of the Dirac point [Saito 2000]. The $\sigma$ bands are typically neglected in electronic band structure calculations. The smallest gap for these bands occurs at the $\Gamma$ point of the Brillouin zone (center of the hexagon), and is $\approx 11\,\mathrm{eV}$ [Reich 2004], making them insignificant for conduction.

Using the effective mass approximation in the continuum limit, the Hamiltonian can be written as [Slonczewski 1958, Ando 1998]:

$$H = c^* \mathbf{p} \cdot \sigma = c^* \begin{pmatrix} 0 & p_x - ip_y \\ p_x + ip_y & 0 \end{pmatrix}, \tag{5}$$

where $\sigma$ refers to the Pauli matrices. The $2 \times 2$ Hamiltonian and the two-component eigenfunctions reflect the valley symmetry of the Brillouin zone, stemming from the two equivalent sublattices.

The two identical carbon atoms in the unit cell are related by inversion symmetry. Because of this, they can be considered constituents of identical but distinct triangular sublattices, a fully symmetric bipartite lattice. The crystal symmetry is reflected in the Hamiltonian and the two-component wavefunctions and permits a conserved quantity called chirality. The new index created by the *spinor-like* wavefunctions describes a spin for the unique sublattices, called *pseudospin*. Chirality is the relative alignment of the pseudospin vector with the momentum vector, and can be configured in parallel (electrons) or antiparallel (holes) arrangements. The required conservation of this quantity permits fantastic quantum effects such as Klein tunneling, or the absence of normal backscattering ($\mathbf{k} \rightarrow -\mathbf{k}$) [Ando 1998, Katsnelson 2006].

It is customary to label the atoms of the symmetric triangular sublattices $A$ and $B$ (Fig. 3). If graphene sheets are stacked in a graphitic configuration (also called Bernal or AB stacking), the inversion symmetry is broken. Bernal stacking is created by taking two aligned graphene sheets (also called AA stacked sheets, shown in the left panel of

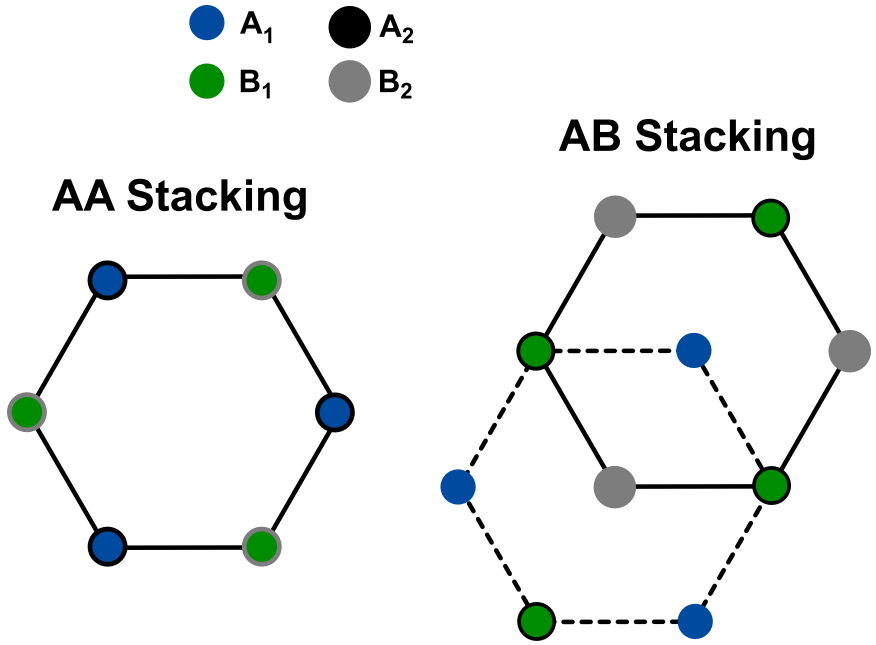


Figure 3: Stacking structures of graphene monolayers layers. In AA stacking, atoms from each layer stack over each other; however, the more energetically favored AB stacking of graphene layers is the common structure of graphite. AB stacking breaks the sublattice symmetry, because one sublattice always lies on top of a sublattice from the layer below, while the other sublattice overlaps the centers of the hexagons in the underlying sheet.

Fig. 3) and rotating one lattice exactly 60 °. In Bernal stacking, the *A* atom has no neighbor directly beneath it, unlike the *B* atom. As one might suspect, the loss of symmetry results in dramatic changes to the band structure. Bilayer graphene, stacked in Bernal configuration, has a hyperbolic (parabolic) dispersion rather than linear [McCann 2006]. Comparisons to other bipartite lattices are often used as illustrations as well. Hexagonal boron nitride (h-BN) has a similar structure to graphene; however the distinguishability of the boron and nitrogen atoms does not allow the same sublattice symmetry as graphene. Consequently, it does not exhibit a linear band structure and has a band gap [Novoselov 2007].

## *1.2 Graphene in a Uniform Magnetic Field*

Application of a magnetic field perpendicular to the graphene plane causes the circulation of electrons in cyclotron orbits. The resulting quantization of energies produces a series of peaks in the density of states, called “Landau levels.” The linear band structure

of graphene produces an unconventional spectrum of quantized cyclotron energies, leading to distinctive signatures in experimental measurements such as the so-called "half-integer" quantum Hall effect. In the sections that follow, we derive the Landau level (LL) structure for graphene and discuss the quantum Hall effect as it pertains to STS measurements presented in Chapter 4.

### 1.2.1 Derivation of Landau Quantization

#### *1.2.1.1 Parabolic Energy Dispersion*

Initially, the Landau level dispersion for 2-dimensional free electron systems ($2DES_{conv}$) will be derived. Using ladder operators ($\Pi_{\pm}$), the eigenstates can be solved and the operators will be re-used to calculate the Landau level dispersion for graphene.

For free electrons in a $2DES_{conv}$, the Hamiltonian $H$ is written as:

$$H = \frac{p_x^2}{2m_e} + \frac{p_y^2}{2m_e}. \tag{6}$$

In this equation, $\mathbf{p}$ is the momentum and $m_e$ is the mass of the electron. We then introduce a magnetic field along the $\hat{\mathbf{z}}$ direction. The magnetic field introduces a vector potential $\mathbf{B} = \nabla \times \mathbf{A}(\mathbf{r})$ which can be accounted for by using a Peierls substitution [Goerbig 2009]. We replace the momentum $\mathbf{p}$ with the dynamical momentum $\mathbf{\Pi}$ in the Hamiltonian, $\mathbf{\Pi} = \mathbf{p} + e\mathbf{A}(\mathbf{r})$ giving [Jackson 1998, Tőke 2006]:

$$H = \frac{1}{2m_e}(\Pi_x^2 + \Pi_y^2). \tag{7}$$

Note that $\mathbf{\Pi}$ is gauge invariant. This must be the case, because we do not choose a gauge and will derive a result that is gauge independent. Thus, if the vector potential transforms as $\mathbf{A} \rightarrow \mathbf{A} + \nabla\lambda$, then the momentum must be $\mathbf{p} \rightarrow \mathbf{p} - e\nabla\lambda$. We construct the ladder operators in the same way as the angular momentum ladder operators ($J_{\pm}$) [Goerbig 2009]. Formally,

$$\Pi_{\pm} = \Pi_x \pm i\Pi_y. \tag{8}$$

These operators have a common set of eigenkets, defined as $\mid N\rangle$. Application of $\Pi_+$ and $\Pi_-$ to the eigenkets gives:

$$\Pi_+ \mid N\rangle = \frac{\sqrt{2}\hbar}{\ell_B}\sqrt{N+1} \mid N+1\rangle \tag{9}$$

$$\Pi_- \mid N\rangle = \frac{\sqrt{2}\hbar}{\ell_B}\sqrt{N} \mid N-1\rangle \tag{10}$$

In order to rewrite the Hamiltonian in terms of the ladder operators, we rearrange them as:

$$\Pi_x = \frac{1}{2}(\Pi_+ + \Pi_-), \tag{11}$$

$$\Pi_y = \frac{-i}{2}(\Pi_+ - \Pi_-). \tag{12}$$

Thus, the Hamiltonian can now be written as:

$$H = \frac{1}{4m_e}(\Pi_+\Pi_- + \Pi_-\Pi_+) \tag{13}$$

This is further reduced by determining the commutator of the ladder operators,

$$[\Pi_+, \Pi_-] = [\Pi_x + i\Pi_y, \Pi_x - i\Pi_y] = -2i[\Pi_x, \Pi_y] = -2\frac{\hbar^2}{\ell_B^2}. \tag{14}$$

The resulting Hamiltonian is:

$$H = \frac{1}{2m_e}(\Pi_+\Pi_- + \frac{\hbar^2}{\ell_B^2}). \tag{15}$$

And the Landau level energy ($E_N$) is given as:

$$E_N \mid N\rangle = H \mid N\rangle = \frac{\hbar^2}{m_e\ell_B^2}(N+\frac{1}{2}) \mid N\rangle = \hbar\omega_c(N+\frac{1}{2}) \mid N\rangle \tag{16}$$

where $\omega_c$ is the cyclotron frequency.

#### *1.2.1.2 Graphene*

For graphene, the negligible mass of the electrons at energies around the Dirac point would cause the $2DES_{conv}$ Hamiltonian in equation 7 to become unbounded. Therefore, we use the form of the Dirac-Weyl Hamiltonian for the $\mathbf{K}^+$ valley [DiVincenzo 1984]:

$$H = c^*\mathbf{p}\cdot\sigma = c^*\begin{pmatrix} 0 & p_x - ip_y \\ p_x + ip_y & 0 \end{pmatrix} \tag{17}$$

which is the Hamiltonian from the effective mass approximation in equation 5 [Ando 1998]. In this formalism, we use $c^*$ to indicate the velocity of charge carriers and $\sigma$ are the Pauli matrices. Once again, we use the Peierls substitution when we apply a magnetic field perpendicular to the sheet [Goerbig 2009, Tőke 2006]:

$$H = c^*\mathbf{\Pi}\cdot\sigma = c^*\begin{pmatrix} 0 & \Pi_x - i\Pi_y \\ \Pi_x + i\Pi_y & 0 \end{pmatrix} = c^*\begin{pmatrix} 0 & \Pi_- \\ \Pi_+ & 0 \end{pmatrix} \tag{18}$$

To diagonalize this $2\times 2$ Hamiltonian, we need to construct a spinor eigenbasis:

$$\psi_N = \begin{pmatrix} u_N \\ v_N \end{pmatrix} \tag{19}$$

which, when used as an eigenstate of the Hamiltonian gives a system of equations to solve. The components $u_N$ and $v_N$ relate to the A and B sublattices, respectively.

$$c^*\Pi_- v_N = \epsilon_N u_N \tag{20}$$

$$c^*\Pi_+ u_N = \epsilon_N v_N \tag{21}$$

We can solve for $u_N$ in the first equation and substitute it into the second equation, yielding:

$$(c^*)^2\Pi_+\Pi_- v_N = \epsilon_N^2 v_N \tag{22}$$

and after applying the ladder operators, we find the energy dispersion for Landau levels in graphene

$$\epsilon_N = \pm c^*\frac{\hbar}{\ell_B}\sqrt{2|N|} = \pm c^*\sqrt{2e\hbar B|N|}. \tag{23}$$

#### *1.2.1.3 Discussion*

Graphene boasts a markedly different LL structure than that of a $2DES_{conv}$. The LLs progress in energy as $E_N \propto \sqrt{|N|B}$ rather than maintaining a linear proportionality. Qualitatively, a $\sqrt{|N|}$ LL structure makes sense. The density of states in such a system must be proportional to the energy $\rho(E) \propto |E|$. If one naïvely assumes that each LL contains an

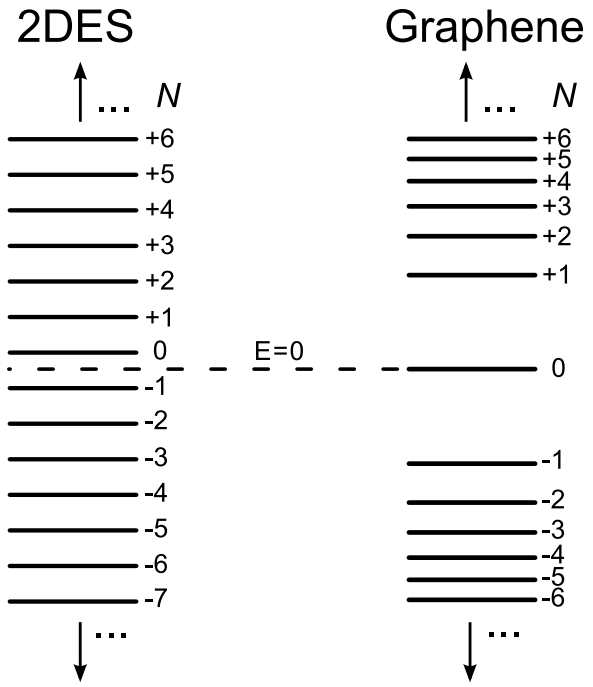


Figure 4: LL structure of $2DES_{conv}$ (left) vs. graphene (right). LLs in the $2DES_{conv}$ are equally spaced, with a gap at the center. The spectrum for graphene progresses as $\sqrt{|N|}$, centered at the Dirac point. There is a large gap between $N = 0$ and $N = \pm 1$, and the LLs get closer together at higher LL index.

equal number of states (has equal degeneracy), then dividing $\rho$ into equal areas yields the appropriate structure.

This LL dispersion is unique to Dirac fermions, and measurement of such a spectrum demonstrates their existence in the material. Interestingly, we find that unlike the $2DES_{conv}$, graphene has a unique non-dispersing zero-energy state at the center of the spectrum ($LL_0$) (see Fig. 4). The rapidly increasing gaps in the density of states between $LL_0$ and $LL_1$ could provide enough energy separation to demonstrate the quantum Hall effect at room temperature, which would be useful for a room temperature quantum Hall resistance standard. These Landau levels also have a valley degeneracy which comes from the identical band structure around the $K_+$ and $K_-$ points in the Brillouin zone. Counting spin, symmetries account for a total factor of 4 in degeneracy, differing from the factor of 2 in *most* $2DES_{conv}$.

Of note, we find interesting behavior from the $N = 0$ wavefunction $\psi_0$. We can choose

$v_N$ to be $|\ 0\rangle$. Since the lowering operator cannot be applied to the $|\ 0\rangle$ wavefunction, $u_N = 0$. Therefore, we arrive at an interesting conclusion. The wavefunction, $\psi_0$ takes the form:

$$\psi_0^{(+)} = \begin{pmatrix} 0 \\ |\ 0\rangle \end{pmatrix}, \tag{24}$$

$$\psi_0^{(-)} = \begin{pmatrix} |\ 0\rangle \\ 0 \end{pmatrix}. \tag{25}$$

If we continue solving for LL wavefunctions with index $|N| > 0$, the raising and lowering operators produce *at least* some wavefunction density in each of the $K_+$ and $K_-$ valleys:

$$\psi_{|N|>0}^{(+)} = \frac{1}{\sqrt{2}} \begin{pmatrix} |\ N-1\rangle \\ sgn(N)\ |\ N\rangle \end{pmatrix}, \tag{26}$$

$$\psi_{|N|>0}^{(-)} = \frac{1}{\sqrt{2}} \begin{pmatrix} sgn(N)\ |\ N\rangle \\ |\ N-1\rangle \end{pmatrix}. \tag{27}$$

This, however, is not the case for the $LL_0$ wavefunction. As we see from equations 24 and 25, $LL_0$ is special in that the wavefunction density does not overlap between valleys. Spatially, this manifests itself in a complete polarization of the A and B sublattices where each of the orthogonal wavefunctions have concentrated density over the individual A and B sublattice sites.

## *1.3 Fabrication*

Several methods have been devised for the production of graphene samples. What follows is a description of some of the more prominent techniques for graphene production. Most attention will be given to preparation of epitaxially grown graphene, as it was the method that was used to prepare samples for the work in this thesis.

### 1.3.1 Exfoliation

First published in 2004, the technique of mechanical exfoliation has been one of the most widely applied methods of isolating graphene sheets [Novoselov 2004]. The most appealing aspect of this technique is the relative ease with which one can begin to prepare graphene flakes. Starting with a high-quality piece of highly oriented pyrolytic graphite (HOPG), Kish graphite or natural graphite, the research enthusiast presses a piece of tape against the surface. The tape is then pulled from the surface and the process of removal causes thin graphitic pieces to detach from the surface.

Following the procedure described in the original paper [Novoselov 2004], the flakes are exfoliated into a beaker of acetone. A wafer of $SiO_2$ (300 nm thick) on doped Si is dipped into the solution. The dispersed flakes stick onto the surface and the wafer is then washed to remove thicker flakes. Normally thin graphitic flakes are optically transparent, but because of the selected thickness of the $SiO_2$ layer, monolayer and bilayer graphene flakes can be distinguished using an optical microscope. Since the original paper, researchers have typically simplified the method so that thin graphitic flakes are exfoliated directly to the substrate and graphene pieces are identified optically.

The ease of quality graphene production and the ability to control the charge density using a back-gate led to rapid verification of some of the unique properties of graphene. Shortly following the 2004 paper on the exfoliation and verification of graphene, the half-integer quantum Hall effect was observed [Novoselov 2005, Zhang 2005].

Despite the high quality of exfoliated graphene, $SiO_2$ is not the most ideal substrate. Charge trapping at the interface leads to large electron and hole puddles [Martin 2008]. Scattering from these impurity sources limits the mobility and affects the minimum conductivity at the Dirac point [Geim 2007, Bolotin 2008]. Another limiting source in the mobility of graphene on $SiO_2$ is the electron interaction with optical phonons at the $SiO_2$ surface [Chen 2008]. Similar problems exist for other choices of substrate; however stiffer,

less polarizable crystals such as SiC will reduce the interaction [Fratini 2008]. Additionally, graphene samples exfoliated onto $SiO_2$ exhibit nanometer sized ripples. These ripples were conjectured to be *intrinsic* [Fasolino 2007], but are not observed in epitaxially grown samples or samples exfoliated onto mica [Lui 2009]. The corrugations of the sheet contribute effective magnetic fields of $B \sim 0.1 - 1\,\mathrm{T}$ which significantly broaden the LLs [Guinea 2009].

Suspension of the graphene sheet over open holes provides a nearly ideal research solution to problems associated with the $SiO_2$ substrate. Very high quality samples have been produced with mobilities as high as $200{,}000\,\mathrm{cm}^2/\mathrm{Vs}$ [Bolotin 2008]. Ripples in the graphene sheet can be smoothed by thermal annealing, and as a result, led to the observation of fractional quantum Hall states [Bolotin 2009, Du 2009].

Though this method of graphene isolation has been extremely useful as a research tool, it is not likely to extend beyond that domain. Industries require a scalable method of commercial production, which is not feasible given the tedious process behind exfoliation and thickness identification. For this reason, other methods of making graphene have also found great success in concurrent research.

### 1.3.2 Chemical Vapor Deposition

More recently, graphene has also been produced by chemical methods. The exciting potential of this method is that very large graphene sheets can be produced. Sheets as large as 30 inches have been produced, and the technology is quickly being adapted for commercial use [Bae 2010].

Graphene is produced at low temperatures ($< 1000\,^\circ\mathrm{C}$) by heating metals in ambient pressures of hydrocarbon gases. This has been successful on a number of metals including Ir(111), Ru(0001), or Pd(111)[Marchini 2007, N'Diaye 2008, Kwon 2009]. On copper foils, the low solubility of carbon in copper causes the growth process to be self-limiting [Li 2009b]. Large area films can be produced with mostly monolayer coverage (95%).

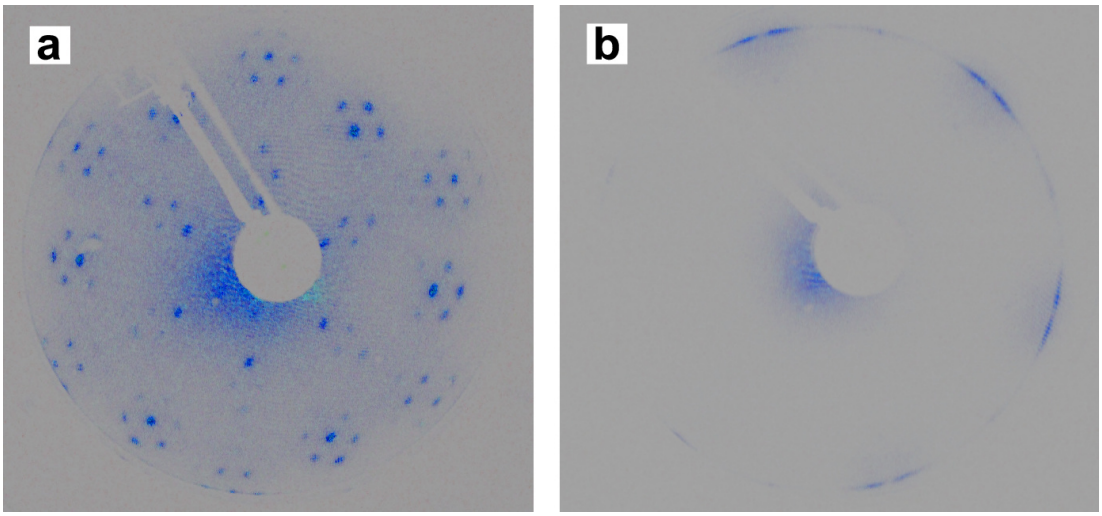


Figure 5: Low energy electron diffraction images of graphene grown on the (a) Si face and (b) C face of SiC. Graphene on the Si face has a distinct spots graphene spots at 30 ° to the SiC. The extra spots around the graphene are due to the $\left(6\sqrt{3}\times 6\sqrt{3}\right)R30°$ reconstruction. Graphene on the C face shows quasi-ordered rotations with primary intensity around 0 ° (a dip in intensity directly at 0 °). A slight increase in intensity is seen at 30 ° to the SiC spots.

Typically these films do not display high mobilities (100-2000 $cm^2/Vs$). This is likely due to grain boundary scattering within the sheet [Reina 2009].

### 1.3.3 Epitaxial Growth on SiC

It has been known for many years that the thermal decomposition of SiC produces graphitic films [Bommel 1975, Forbeaux 1998]. In 2004, researchers at Georgia Tech extended this research as an avenue toward scalable graphene production for use in nanoelectronic applications [Berger 2004, Berger 2006]. Since that time, many of the expected properties of graphene have been verified and mobilities as high as those of suspended graphene have been measured [Sprinkle 2009, de Heer 2007, First 2010, Orlita 2008].

Most of the research in graphene grown on SiC has focused on the SiC(0001) and SiC(000$\bar{1}$) crystallographic faces. Silicon and carbon are tightly bonded in a Si/C bilayer. When cut into wafers along the SiC(0001) (or SiC(000$\bar{1}$)) direction, this necessarily means that opposite sides of the wafer will be terminated with different atoms (i.e. silicon on one side, carbon on the other). The SiC(0001) is Si terminated (often called *silicon face*), while

SiC(000$\bar{1}$) is C terminated (*carbon face*). Unfortunately, the process of growth and cutting of silicon carbide leaves the wafers too thick for backgating ($\gtrsim 350\mu m$). While backgating would be preferred for a number of research applications, industrial application through top and side gating has been demonstrated [Moon 2009, Li 2010]. Silicon carbide comes in many polytypes including cubic, hexagonal and rhombohedral forms. Hexagonal polytypes (4H- and 6H-) are often selected for their close registry with the graphene lattice. Single crystal wafers are commercially available from a variety of manufacturers in varying quality. The quality of SiC wafers has steadily improved over the past several years, enabling the growth of better graphene films.

The process of growth is unusual compared to standard film production techniques, but is quite simple to describe. When a piece of SiC is heated above a certain temperature ($\sim 1300\,^{\circ}$C), the crystal begins to decompose. Silicon atoms preferentially leave the surface due to a higher vapor pressure than the carbon [First 2010]. The remaining carbon atoms reform into graphene sheets which are a thermodynamically stable phase at the growth temperature. Coverage of graphene grown on SiC is generally edge-to-edge. This greatly simplifies many characterization techniques and is the reason epitaxial graphene is so well characterized.

Growing high quality films is more complex, but is becoming increasingly more understood. Film quality from growth in high- and ultra high-vacuum (UHV) has never been very good. The monolayer growth temperature is fairly low (as low as $\sim 1200\,^{\circ}$C). The SiC(0001) films undergo significant pitting and step etching, while SiC(000$\bar{1}$) films suffer from small domains (tens of nanometers) and substrate roughening [Hass 2008a]. The film on the carbon face appears cracked under AFM, yet the silicon signal under Auger electron spectroscopy (AES) and spots in low energy electron diffraction (LEED) suggest that there is a significant quantity of silicon at or near the surface. I am inclined to believe that this is not representative of the graphene thickness, but rather indicative of the small, separated size of the domains which leave bare SiC over a large fraction of the surface.

It is clear from experiment that supression of the silicon evaporation rate is an extremely important factor in achieving high quality films. By suppressing the evaporation of Si from the surface, the graphene growth temperature increases. There are several ways to achieve this. The most successful growth methods have been stagnant atmosphere low-vacuum techniques [Berger 2006] and directed flow of Ar or $SiH_4$ (or $Si_2H_6$) [Emtsev 2009, Tromp 2009]. Kinetic growth modeling shows that the geometry of the furnace is critical. In a stagnant atmosphere hot-wall design, it is important to have a well enclosed geometry so that the cell can obtain a reasonable silicon vapor pressure [Torrance 2010]. While not the main focus of this thesis, Chapter 2.4.4 presents details of a furnace designed to achieve these goals

In the next two sections, I will discuss the specifics of films grown on each surface. Because most of my research focused on carbon face films, I will go into more extensive detail about the growth and morphology of that face.

#### *1.3.3.1 Properties of SiC(*0001*) Films*

Traditionally, this face has been given more attention because it is crystallographically aligned with the substrate. The growth of graphene is also generally slower and easier to control on the Si face than on the carbon face. SiC(0001) can undergo a number of stable surface reconstructions during thermal annealing. Phases most commonly observed in LEED are ($\sqrt{3} \times \sqrt{3}$)R30° and ($3 \times 3$) [Starke 1999, Heinz 2000], and annealing above 1100 °C leads to the ($6\sqrt{3} \times 6\sqrt{3}$)R30° phase (seen in Fig. 5a) [Owman 1996, Berger 2006, Starke 2009]. Between the bulk SiC and the first graphene layer, there is a *buffer layer*. The buffer layer is consistent with a ($6\sqrt{3} \times 6\sqrt{3}$)R30° reconstruction.

The buffer layer (or *layer 0*) is a carbon rich ($6\sqrt{3} \times 6\sqrt{3}$)R30° partially covalent layer [Rutter 2007, Hass 2008b]. This interface layer is a complex arrangement of structures, showing a pattern of apparent tetramers and hexagons in STM, and in STS, revealing a gap around $E_F$ [Rutter 2007]. The tetramers are thought to be pyramidal structures in registry

with the $1 \times 1$ lattice, while the hexagons are ordered with the $(\sqrt{3} \times \sqrt{3})R30^\circ$ lattice. This reconstruction is a precursor to the growth of the first layer, but is not itself a graphene layer as indicated by the lack of continuous $\pi$ bands around the $K$ point [Starke 2009]. Recently, this buffer layer has been decoupled from the SiC through passivation by hydrogen intercalation [Riedl 2009]. Passivation recovers the $\pi$ bands, resulting in a quasi-free-standing graphene layer.

Growth on the silicon face tends to be slow. After a few monolayers (ML) of coverage, the growth process seems to stop (it is self-limiting for a given temperature) [de Heer 2007]. When multiple graphene layers are present, the film is Bernal stacked as in graphite or few-layer exfoliated graphene films (FLG). The first layer is highly doped by the interface ($n \approx 10^{12}\,/\mathrm{cm}^2$), and mobilities are generally around 1000-2000 $\mathrm{cm}^2/\mathrm{Vs}$. Very early on, oscillations in the longitudinal resistance $R_{xx}$ (called Shubnikov deHaas Oscillations) verified the $\sqrt{|N|B}$ LL structure of the half-integer quantum Hall effect [Berger 2006], which has since been fully demonstrated [Shen 2009].

#### *1.3.3.2 Properties of SiC($000\bar{1}$) Films*

More recently, much attention has been turned to the growth of films on the carbon terminated face (also called multilayer epitaxial graphene or MEG). Unlike the silicon face, films on the carbon face grow rapidly and seemingly without limit. Film thicknesses in excess of 100 layers have been achieved in carbon face growth. Recent efforts have shown that very thin films, down to a few layers or even a single monolayer, are possible in a well calibrated furnace [Wu 2009].

Graphene grown on the carbon face attains very high quality. The material is very flat ($\lesssim 0.5$ Å corrugation) and continuous over the SiC steps. Often pleats are found on the surface (ridges up to 9 nm in height) as a residual manifestation of the thermal contraction mismatch. Upon cooling after the growth process, the graphene buckles to relieve stress, but the graphene sheet remains continuous. Domains between the pleats are rather large,

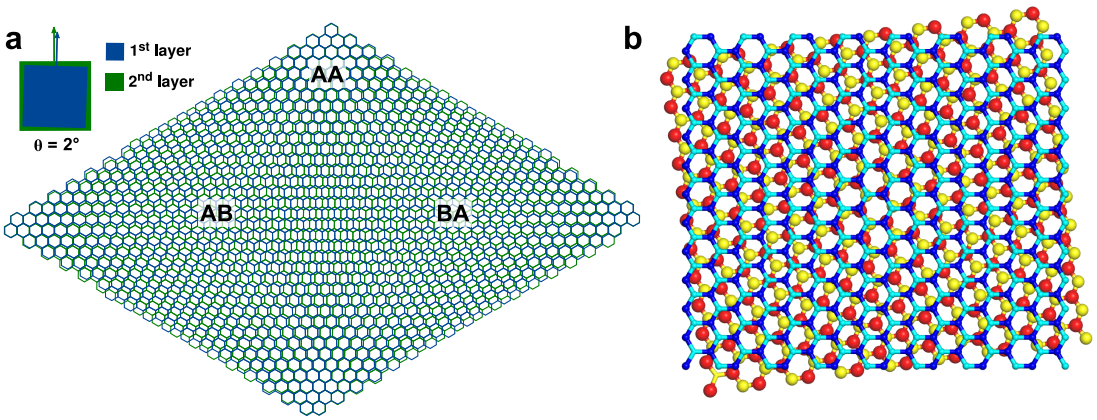


Figure 6: Figures showing the stacking of graphene sheets with rotational domains. (a) A moiré cell at a rotation of 2 degrees. The low angle of rotation creates large areas in the film where stacking is similar to AA and AB stacking. AB stacked areas are complemented by BA stacked areas to preserve sublattice symmetry over the moiré cell. This is better seen in (b) where A and B atoms from different layers have been colored differently so that the AB/BA inversions can be easily seen as mostly red/yellow showing through from the bottom layer.

typically several microns.

The first layer of carbon face graphene is also significantly doped ($n \approx 5 \times 10^{12}$ /cm$^2$). Infrared spectroscopic measurements have been used to characterize the screening length and found an exponential drop off in the charge density with the number of graphene layers, yielding a charge screening length of $\approx$ 1 layer [Sun 2010]. This leaves most layers of thicker samples nominally undoped.

One of the most unique features of multilayer films on SiC$(000\bar{1})$ is the unusual layer stacking. While graphene on the silicon face stacks in a very ordered Bernal configuration, stacks of graphene on the carbon face are only quasi-ordered (see Fig. 5b). X-ray and LEED experiments (see Fig. 5b) find broad peaks corresponding to rotations of $\pm 2.2^\circ$ and $30^\circ$ to the SiC lattice, implying only a weak preference for the orientation of the sheet [Hass 2007]. A number of other rotations are allowed which result in commensuration of the graphene hexagon over a larger supercell [Hass 2008a, Trambly de Laissardiere 2010].

Consequently, the supercell created by the slight rotation of two graphene lattices introduces new symmetries. Each supercell contains regions of AA-like alignment and AB-like alignment. Unlike pure Bernal stacking, the AB-like alignment is complemented by an

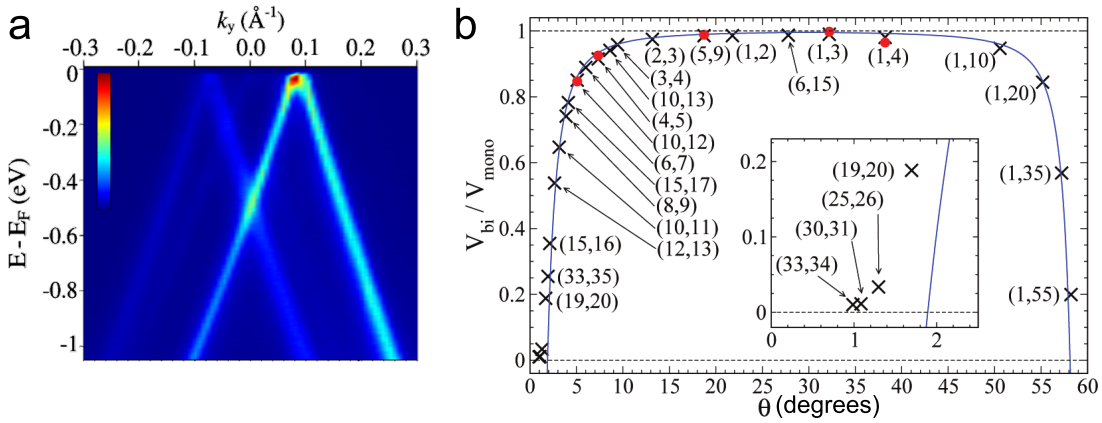


Figure 7: (a) ARPES measurement of graphene on SiC(000$\bar{1}$) showing the linear band structure. Bands from subsurface layers in the MEG stack can also be seen faintly and have linear bands as well due to electronic decoupling. Reprinted from [Sprinkle 2009] (b) Predicted renormalization of $c^*$ as a function of relative angle between two graphene sheets. For relative rotation angles below 5 °, the carrier velocity drops off sharply, while the higher angular rotations remain relatively unaffected. Reprinted from [Trambly de Laissardiere 2010].

inversion (BA-like alignment) within the same supercell (see Fig 6). Despite the local distinguishability of the AB atomic structure, a new symmetry is formed on the length scale of the twisted-layer supercell.

The consequences of this rotation are quite profound. Studies have shown that rotated layers lead to an increased layer separation [Hass 2008c], linearity of the band structure around the $K$ points (Fig. 7a) [Sprinkle 2009] and $\sqrt{NB}$ Landau levels [Sadowski 2007, Miller 2009]. These measurements suggest a *decoupling* or electronic isolation of the graphene layers, where each layer in the multilayer stack acts as a single layer. This is an important detail, because one might expect the same behavior in HOPG where the top layer(s) is often rotated with respect to the bulk [Pong 2005b]; however, the bulk 3D behavior is present or sometimes coexistent with Dirac fermions in HOPG due to primarily Bernal stacking in the bulk [Li 2007]. In multilayer graphene, this has not been found to be the case.

The rotated stacking may not be entirely without effect (as will also be shown experimentally in Chapter 4). Theoretical studies predict a renormalization of the carrier velocity around the Dirac point (Fig. 7) [Lopes dos Santos 2007, Trambly de Laissardiere 2010].

As one might expect, the closer the rotation is to that of Bernal stacking (0 or 60 °), the lower the renormalized velocity. Lower rotation angles have a larger unit cell with spatially larger regions of AB and BA stacking. Still another theory predicts different behavior depending on the type of commensuration that exists at the given rotation angle [Mele 2010]. These can be classified as even or odd coincidence lattices, where even lattices have a gap and odd lattices do not; however, these predictions have not been confirmed in angle-resolved photoemission experiments which did not find either velocity renormalization or the presence of a gap [Sprinkle 2009].

# CHAPTER II

# EXPERIMENTAL APPARATUS AND METHODOLOGY

A variety of techniques were used to characterize and produce epitaxial graphene at both Georgia Tech and NIST facilities. These methods are briefly discussed in this chapter.

## *2.1 Scanning Tunneling Microscopy*

### 2.1.1 History

The first scanning tunneling microscope is considered to have been invented in 1981 by Gerd Binnig and Heinrich Rohrer. Their work on this device would later win them the 1986 Nobel prize in physics [Binnig 1987].

In earlier years, similar "precursor" devices had been invented. In 1965, a *field emission ultramicrometer* was created, which utilized the exponential sensitivity of field emission current with respect to the emission probe's proximity to a metallic surface [Young 1966]. Proposed applications for this device included a strain gauge, thermal expansion cell, vibration measurement apparatus and a *surface profile delineator*. Young described a *constant current* operational mode, whereby the bias voltage between the emitter and the sample could be adjusted in order to keep the field emission current constant.

A few years later, Young adapted this technology to a device which could read the height profile of surfaces with very fine vertical resolution [Young 1972]. His device, called the *topografiner*, included piezos for motion in all spatial directions enabling height measurements within 30 Å of resolution. His proposed constant current mode was adapted so that the separation between the emitter and sample (conventionally labeled the z direction) stayed constant, while the bias voltages was held constant. By keeping the current constant while rastering the probe across the surface, he was able to measure variations in a diffraction grating. This method of constant current scanning is still the preferred operating mode

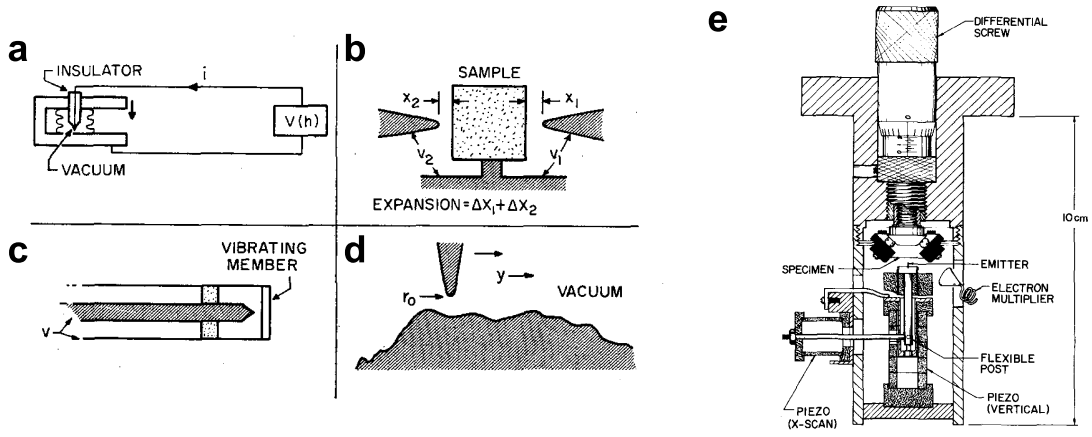


Figure 8: Potential applications of the field emission ultramicrometer. These include (a) a strain gauge, (b) a thermal expansion cell, (c) vibration detection and (d) a surface profile delineator. (Reprinted from [Young 1966].) (e) The surface profile delineator was later developed and named the "topografiner." [Young 1972]

of scanning tunneling microscopists today.

Young's topografiner was an important step toward the modern scanning tunneling microscope. Binnig and Rohrer greatly improved on his work by utilizing the phenomenon of vacuum tunneling. Tunneling requires that the sharp emitter (now simply called a tip) be brought within a few angstroms of the surface so that the tails of the wavefunctions from electrons in the sample overlap onto the tip. When this happens, quantum mechanical probabilities suggest that a measurable number of electrons can penetrate the vacuum barrier and tunnel into the tip. The advantage of vacuum tunneling over field emission is an increase in both vertical and horizontal resolution greater than three orders of magnitude! The extremely fine resolution of the scanning tunneling microscope is primarily the reason that it has become such a popular technique in surface science today; however, the full potential of the device was realized shortly after, when more extensive theoretical descriptions revealed its versatility in spectroscopic techniques.

### 2.1.2 Theory

The theory of scanning tunneling microscopy at this point is well understood. The vacuum between the tip and the sample can be viewed as a rectangular potential barrier; therefore,

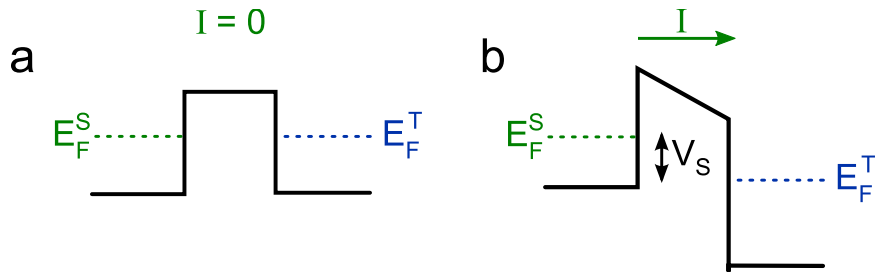


Figure 9: Schematic of a vacuum potential barrier when (a) the Fermi energy in the sample $E_F^S$ is equal to the Fermi energy in the tip $E_F^T$ (for materials with equal work functions), and (b) when a bias is applied $V_S$ such that $E_F$ in the tip and sample and not equal and tunneling current is generated.

we can view the wavefunctions of the electrons as having exponential decay inside the potential barrier. The closer the tip is to the surface, the higher the probability of tunneling.

In the quantum mechanical description, we consider the Schrodinger equation in a simple 1-D model, where the potential, $V(z)$, varies perpendicular to the sample surface. In this case, we have:

$$-\frac{\hbar}{2m}\frac{\partial^2\psi(z)}{\partial z^2} + V(z)\psi(z) = E\psi(z), \tag{28}$$

where m is the mass of the electron. Inside the tip or the sample, electrons have an energy greater than the potential ($E > V(z)$), and the equation is solved with plane waves. In the vacuum, the potential barrier is large, so $E < V(z)$, and the wavefunctions take the form

$$\psi_n = C_n e^{-\kappa z} \tag{29}$$

where,

$$\kappa = 2m(V - E)/\hbar^2. \tag{30}$$

Notice that $n$ is present in equation 29 to denote the $n^{th}$ electron state for materials which have many electrons. Since we know the form of the wavefunction, we can easily calculate the probability for transmission of the $n^{th}$ electron:

$$\mathcal{P}_n = |C_n|^2 e^{-2\kappa d}. \tag{31}$$

In this equation, we consider a finite distance between the tip and sample $d$ which represents the width of the potential barrier. Materials consist of electron states up to their

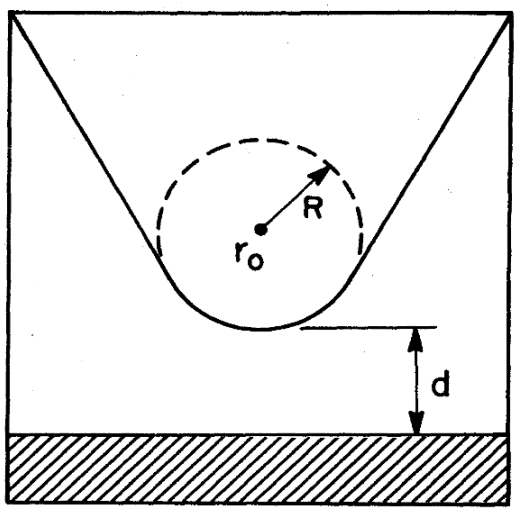


Figure 10: Schematic of an STM tip close to a flat sample surface. Preparation of sharp tips is extremely important for obtaining atomic resolution. The lateral resolution of an STM can be approximated by the radius of the tip at the apex $R$ and the distance of the tip to the surface $d$. Reprinted from [Tersoff 1985].

Fermi energy $E_F$, and in order for an electron to tunnel from one material to another, the electron state must not be occupied. For this reason, materials with equal work functions will not induce tunneling when no bias is applied. To establish a tunneling current, a bias $V_S$ is applied between the tip and the sample in order to change $E_F$ in the tip with respect to $E_F$ in the sample (see Fig. 9). The sign of $V_S$ establishes the direction of current flow. The tunneling current $I$ is then proportional to the sum of all the transmission probabilities from electron states that are allowed to tunnel [Chen 1993, Stroscio 1993]:

$$I \propto \sum_{E_F}^{E_F+eV_S} |C_n|^2 e^{-2\kappa d}. \tag{32}$$

More generally, it can be shown that if the density of states is known for the tip $\rho_T$ and sample $\rho_S$, then the tunneling current is [Bardeen 1961, Tersoff 1985, Lang 1986]:

$$I \propto \int_0^{eV_S} dE \left[\rho_T(E_F + E)\rho_S(E_F - eV_S + E)e^{-2\kappa d}\right]. \tag{33}$$

This exponentially increasing tunneling current is the reason why tunneling works extremely well for scanning surfaces. Small changes in the height of the surface produce

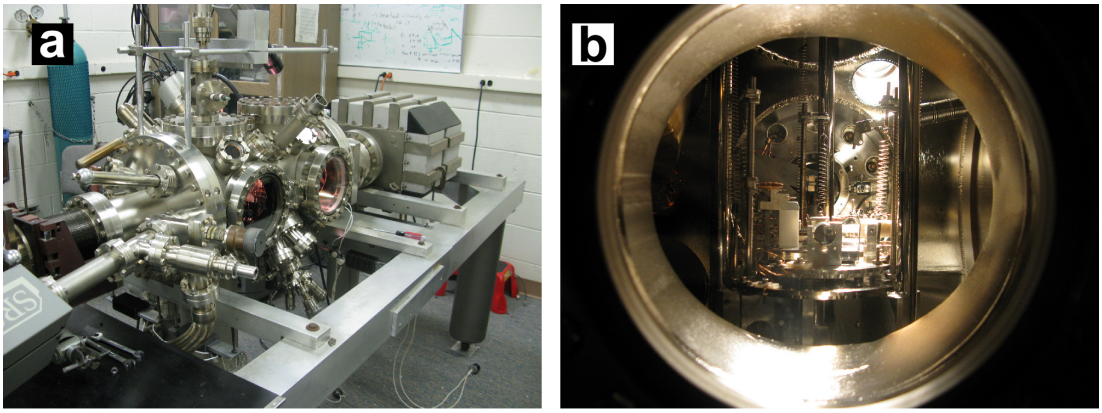


Figure 11: Images of the room temperature scanning tunneling microscope. (a) An exterior view of the UHV chamber. (b) A view inside the window at the actual STM device. The STM is suspended by double spring isolation for more effective high frequency damping.

large changes in the tunneling current. More importantly, it provides very fine resolution in the lateral dimensions. On flat surfaces, the tunneling drops off very quickly for features which are not directly underneath the apex of the tip. Tersoff and Hamann famously derived a simple approximation for the lateral resolution of the tip [Tersoff 1985]:

$$\Delta x = \sqrt{2\,\text{Å}(R+d)} \tag{34}$$

where $R$ is the radius of the tip at the apex and $d$ is the distance to the sample, Fig. 10. A typical tip-sample distance is $d \approx 10\,\text{Å}$, so for an atomically sharp tip, the resolution is still $\sim 4\,\text{Å}$. Because individual atoms are often resolved in STM, this is generally considered to be an upper limit.

### 2.1.3 Equipment

This section provides specific details on the electrical and mechanical operation of scanning tunneling microscopes, including the design of the microscopes used in this thesis. Casual readers may choose to skip this section.

#### *2.1.3.1 Room Temperature Scanning Tunneling Microscope*

The room temperature scanning tunneling microscope (RTSTM) is located at Georgia Tech. The vacuum chamber of the microscope is typically kept at a ultra-high vacuum (UHV)

base pressure of $1\times10^{-10}$ Torr. Ultimate pressure is important for studying sample surfaces, because it determines how long the sample surface will remain clean. A good rule of thumb for a lower bound on the time it takes to obtain monolayer coverage of a clean surface is $Pressure \times 1\,\mathrm{s}/10^{-6}$ Torr. This assumes a 100 % *sticking probability* for species impinging on the surface, so most materials will generally stay clean longer. Graphite for instance, is often imaged in STM under ambient conditions because the sticking probability is extremely low. At $1 \times 10^{-10}$ Torr, a surface can generally stay clean for at least several hours.

The RTSTM uses a Pfeiffer turbomolecular pump and a Perkin Elmer ion pump to achieve UHV pressures. Additionally, it is equipped with a liquid nitrogen-cooled Varian titanium sublimation pump (TSP). The TSP is operated intermittently, immediately following tip or sample heating stages in order to rapidly recover the base pressure. The RTSTM is also equipped with an electron beam heater for cleaning sample surfaces. Temperature is monitored during the heating process using an optical pyrometer.

The tip is approached to the sample surface by a Burleigh inchworm piezo device. The inchworm pushes out a rod that slides the sample forward. The movement is done through a series of clamp and release cycles, where the piezos *inch* the rod forward or backward. During each movement cycle, the tip is pulled all the way back by the electronics. Once the inchworm has moved, feedback is turned on and the tip moves toward the surface until it finds a tunneling current. If there is no tunneling current within the z range of the piezo, then the inchworm movement cycle is repeated.

The system implements feedback through a circuit called the *servo*. The servo controls the z position (height) of the tip, and attempts to maintain a constant tunneling current through a PID loop. The PID loop is the most widely used method of implementing feedback to a control system. PID is an acronym for *proportional, integral and derivative*. A control voltage is generated from the error using the sum of these three terms with their respective gains. Traditionally, an analog servo has been used to control the tip; however,

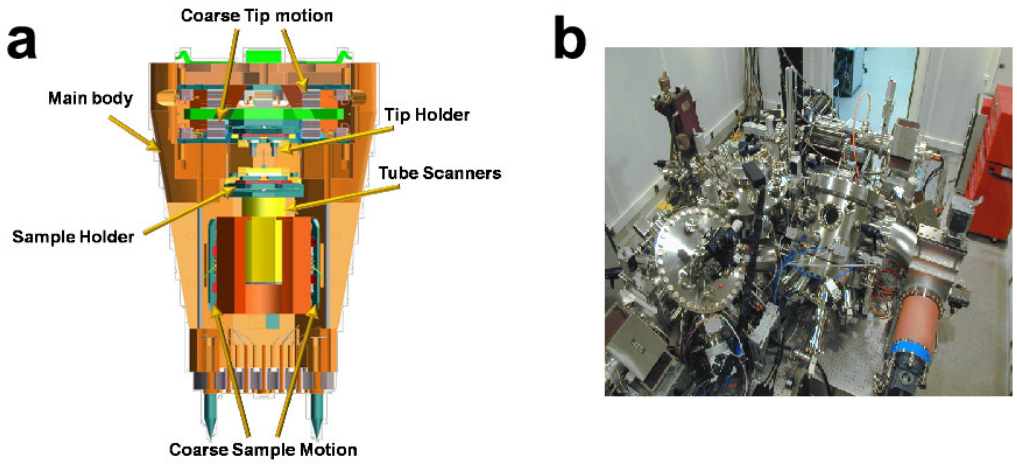


Figure 12: Images of the NIST low temperature scanning tunneling microscope. (a) A schematic of the STM module. The entire STM is contained in a compact molybdenum cell. The sample is mounted on the bottom and approached toward the tip using a Pan-style stick-slip walker design. (b) An image of the entire STM system. The LTSTM is housed inside an acoustic enclosure and offset by air legs and an active vibration isolation system.

recently we have started controlling the tip position digitally using a digital signal processor (DSP). Readers who are interested in technical details about the digital servo should continue onto section 2.2, where this piece of equipment is discussed in detail.

The STM tip is prepared *ex situ* by electrochemical etching. Typically, we prepare polycrystalline tungsten tips and electrochemically etch them using a 1 M KOH solution under an optical microscope. The vacuum chamber is equipped with a load-lock for quick transfer of samples into and out of the system without having to break vacuum inside the main chamber. Tips can be cleaned *in situ* by heating with an electron beam, and they can be characterized using field emission microscopy (FEM).

The RTSTM is also equipped with low energy electron diffraction (LEED) and Auger electron spectroscopy (AES). This allows users to characterize samples to ensure their quality prior to study with the STM. The operation of these devices is deferred until later in section 2.4.2 and 2.4.3.

#### *2.1.3.2 Low Temperature Scanning Tunneling Microscope*

The majority of the measurements done in this work were taken using the low temperature scanning tunneling microscope (LTSTM) located at the National Institute for Standards and Technology (NIST) in Gaithersburg, Maryland (Fig. 12). The LTSTM has a unique design which is extremely rigid toward external vibrations. All of the mechanics of the STM are built inside a rigid, compact molybdenum cell (see Fig. 12a). The sample and tip are placed inside the module, and the sample is approached toward the tip using a stick-slip walker design [Pan 1999]. The sample can be scanned along the x-y plane and servoed in the z direction using a pair of tube piezos mounted underneath the sample. The LTSTM is actively isolated from vibrations through a piezo driven vibration measurement system and passively damped using air legs. It is also protected by an acoustic enclosure which doubles as a Faraday cage, protecting against unwanted electromagnetic interference. All of these mechanisms are designed to produce an extremely quiet, stable environment for taking measurements.

Low temperatures are desirable in STM for several reasons. The LTSTM is equipped with two cryogenic superconducting magnets, which require low temperatures for operation. One magnet can produce a 10 T field perpendicular to the plane of the sample, and the other can create an in-plane 1.5 T magnetic field. Also, thermal drift strongly inhibits the ability to consistently measure atomic scale features over the course of several days. At 300K, atomic lattices must be imaged within a few minutes or the atomic lattice will appear distorted. At 4.2K, the common operating temperature of the LTSTM, one can perform long measurements spanning several days. The only limitation is the boil-off rate of the liquid helium in the 100 L cryostat (which must be refilled on a weekly basis). Spectroscopic features are also limited in energy resolution by thermal broadening. Higher temperatures lead to increased Gaussian broadening, so low temperature spectroscopic measurements can resolve electronic features on much finer energy scales than at room temperature. This is discussed further in section 2.1.5.

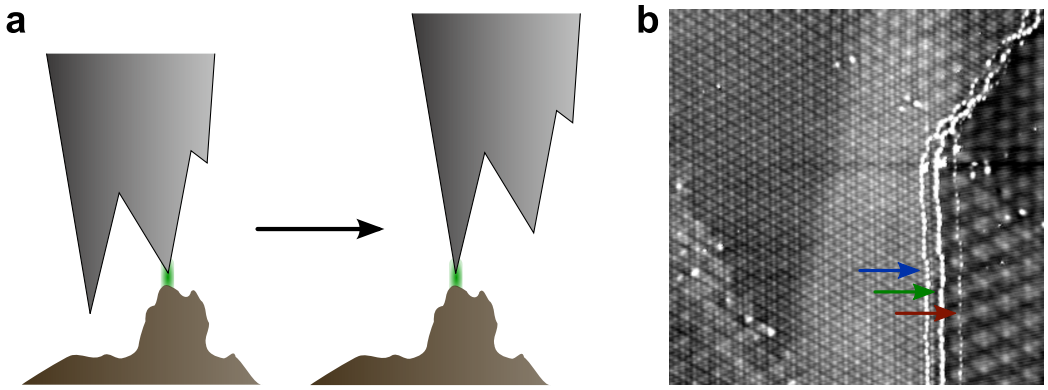


Figure 13: (a) Schematic of multiple tips causing tunneling events at the same location on the sample. This creates and artifact or "ghosting" in the image, where the same feature is seen multiple times. (b) Image is 1000 Å × 1000 Å ($V_S$ = 500 mV, $I_{set}$ = 100 pA, L_25561). Arrows point out ghosting of the same feature because of multiple tips.

### 2.1.4 Topographic Imaging

Topographic images are obtained by scanning the tip over a surface, while using the servo to hold the tunneling current constant. The voltage that is applied to the z-piezo then corresponds to the changes in height on the surface. In fact, this is only partially true. When spatial variations are taken into account, equation 33 should instead be written:

$$I(x,y) \propto \int_0^{eV_S} dE \left[\rho_T(E_F + E)\rho_S(E_F - eV_S + E, x, y)e^{-2\kappa d}\right]. \tag{35}$$

The density of states in the tip $\rho_T$ will remain constant; however the other terms, $\rho_S$ and the exponential term will both vary as the tip is moved. The tunneling current is kept at a constant setpoint, $I_{set}$, so if the sample density of states is not constant over the surface, the tip-sample distance will be adjusted by the servo until $I_{set}$ is reached. Consequently, the resulting image does not just reflect the topography, but will invariably be tied to $\rho_S$.

Topographic images are always a mixture of the surface characteristics and the electronic structure because the tunneling phenomenon is dependent on the local density of states. On a geometrically flat surface, a scanning tunneling microscope may still show oscillations corresponding to fluctuations in the density of states. Sometimes it is hard (if not impossible) to distinguish these features from real surface structural corrugations. This is

often noticeable when trying to image the atomic lattice around defects. The atomic structure is obscured by the localization of charge around the defect, and the increased electron density and dangling bonds affect the imaging.

One technique for differentiating density of states effects from topographic features is to image the same area using different tunneling conditions. Often, simply changing $V_S$ reveals details of the atomic structure that are hidden in the density of states. This, for instance is especially noticeable in bilayer graphene where the stacking asymmetry leads to a different low energy density of states at each atom in the unit cell. At the low energies, one atom is preferentially imaged [Rutter 2008]. Increasing $V_S$ to higher energies yields an equal density of states at each atom in the unit cell, and each atom is imaged equally.

Other times, the tip can introduce features in topography. If the tip is not perfectly smooth near the apex, sharp protrusions in the topography can often lead to *ghosting* or multiple imaging (shown schematically in Fig. 13a). This is commonly observed because nearly all STM tips have additional microtips. The protruding structures induce tunneling with the secondary microtip, creating an identical image of the same structure at a location which is offset by the distance from the primary microtip to the secondary microtip. An example of ghost images appears in Fig. 13b. The multilayer graphene surface has a defect line from a subsurface low angle grain boundary. The top graphene sheet is constant, but the boundary line creates a line of points that are imaged three times (indicated by the red, green and blue arrows) by various microtips.

### 2.1.5 Spectroscopy

This section covers a variety of spectroscopic measurement techniques for STM. Some of these methods (specifically I-V spectra and conductance maps) will be frequently referred to in Chapter 3 of this work.

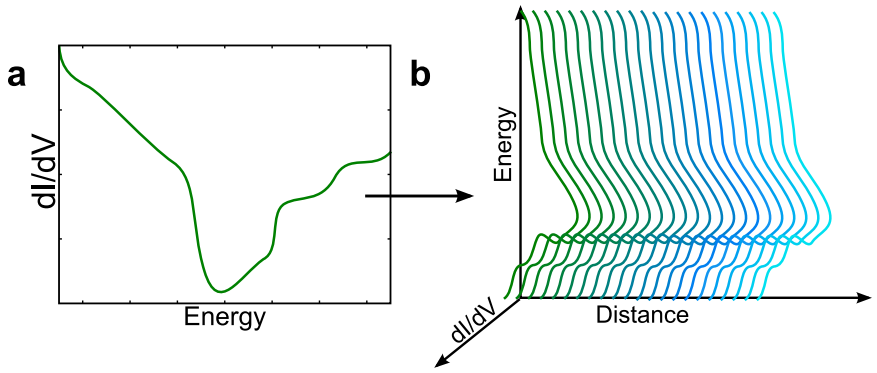


Figure 14: (a) A sketched point $dI/dV$ spectrum. (b) When multiple point $dI/dV$ spectra are taken along a line, they can be stacked into a line scan. This gives a 2D image that contains spatial information about the point spectra.

#### *2.1.5.1 Point I-V Spectra*

One of the most important techniques of the STM is the I-V or more commonly applied $dI/dV$ spectra. More generally, this method of operating an STM is referred to as scanning tunneling spectroscopy (STS). In this method, the servo equilibrates the tip-sample separation ($d$) so that $I_{set}$ is reached. Then, the servo loop is opened (tip is placed in *hold*) so that the tip remains at a fixed distance with respect to the surface. The sample bias $V_S$ is then swept over a specified voltage range and the tunneling current is collected, resulting in an $I$ vs. $V$ curve.

It is typical to also use a lock-in amplifier for a concurrent $dI/dV$ vs. $V$ measurement. The lock-in amplifier sinusoidally modulates $V_S$ by an amplitude $V_{mod}$ at a specified frequency $f_{mod}$. The lock-in then collects the AC component of the tunneling current. The part of the AC current which is in-phase with the the modulation gives $dI/dV$. If we look back at equation 33, we can see why this is important. Typically, metals used for the tip are selected such that they have a constant density of states at low energies around $E_F$. Additionally, $d$ is held constant by the servo, so equation 33 can be reduced:

$$I \propto \int_0^{eV_S} dE \left[\rho_S(E_F - eV_S + E)\right]. \tag{36}$$

Differentiating the tunneling current gives [Chen 1993, Morgenstern 2003a]:

$$\frac{dI}{dV} \propto \rho_S(E_F - eV_S). \tag{37}$$

Thus, by using a lock-in amplifier, we can measure the differential conductance ($dI/dV$), which is directly proportionally to the density of states in the sample.

The energy resolution of the $dI/dV$ is limited by both $V_{mod}$ and the thermal broadening. Density of states features observed using STS have a Gaussian width of [Morgenstern 2003a]:

$$\Delta E = \sqrt{(3.3kT)^2 + (2.5eV_{mod})^2}. \tag{38}$$

At 4.2K, $3.3kT$ is 1.2 meV, so $V_{mod}$ should be kept under a few millivolts. At room temperature, the resolution is significantly lower ($3.3kT$ is 85 meV).

The speed at which data can be taken in STS is determined by the lock-in frequency and the delays (used for settling). At NIST, we used a lock-in frequency of $f_{mod} = 500$ Hz, which defines a minimum time period of 2 ms. The $dI/dV$ measurement at each energy should be averaged over several cycles. Additionally, there is a *settle time* when the sample bias is changed to each new value. The settle time greatly reduces the measurement noise by allowing the everything in the system to relax to equilibrium. Typically, the settle time is at least ~10 time constants (in this case, ≥ 20 ms).

#### *2.1.5.2 Spectral Profiles*

Spatial information can be incorporated into a spectroscopic image by taking multiple point spectra in a line across the sample (Fig. 14). The curves are then stacked along a line and rendered into an image. Often times, this is a very informative way to display data because one axis contains spatial information, while the other axis is energy ($eV_S$). Spectral profiles are good for observing the change in the LDOS as the tip is moved across topographic features. Because they can be done quickly in comparison to conductance maps, spectral profiles are very useful as cursory measurements to locate interesting features.

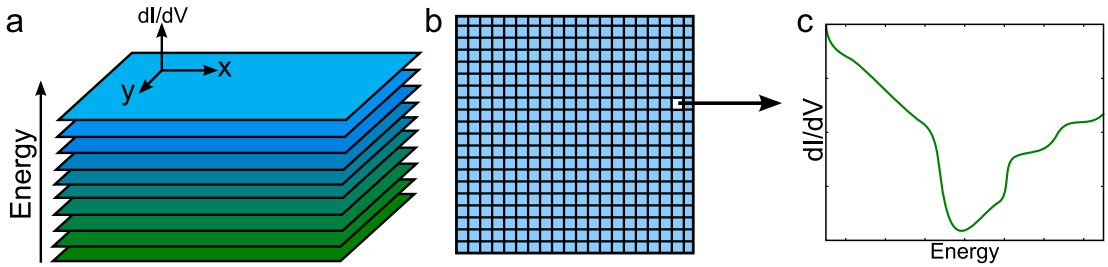


Figure 15: The stack of images in (a) comes from a grid of point spectra (b). Each point contains an entire $dI/dV$ spectrum. An individual image from the stack in (a) contains a 2D map of the local density of states at a discrete energy.

#### *2.1.5.3 Conductance Maps*

Point spectra can be further extended into two spatial dimensions. If a point spectrum is taken at each location in a grid, then the result is a stack of images of the local density of states over two spatial dimensions where each image in the stack corresponds to a different energy $[\rho_S(E_n, x, y)]$.

Large open loop maps can typically only be done at low temperature because of the long times required. The previous discussion of time delays makes STS seem reasonably fast; however the volume of data required for a single map is very large and the settling times are relatively long, so STS mapping cannot be done quickly. At $f_{mod} = 500\,\text{Hz}$, $(251\,\text{pixels} \times 251\,\text{pixels} \times 101\,\text{energies} \times 40\,\text{ms}) \approx 70\,\text{hours}$ to completion. The speed of acquisition is set by $f_{mod}$ because of the settle time and lock-in averaging, which is done over several cycles. The lock-in frequency can be increased; however, the price paid is an increase in the background noise. Maps acquired by the LTSTM at NIST used a lock-in frequency of $f_{mod} = 500\,\text{Hz}$.

The difficulty of these measurements is not necessarily the length of time required for mapping, but the fact that the system must remain perfectly stable for several days while the data is being acquired. In STM, *tip switches* are not uncommon, whereby the configuration of atoms in the microtip rearrange due to electrostatic forces or the addition of stray atoms picked up from the surface. Typically, this alters the spectra and causes artifacts

in the resulting conductance map images. More importantly, STMs used for conductance mapping must have excellent vibrational damping and low drift characteristics, such that a single atom in an image can be located ~3 days later.

#### *2.1.5.4 I-Z Measurements*

Though other measurements still exist, the last spectroscopy technique I will discuss is the current vs. tunnel gap ($I$ vs. $z$) measurements. These measurements are performed by placing the tip in hold and measuring the tunneling current as the tip is pulled back from the surface. From equation 32, we expect an exponential dependence on the tunneling current. The data can be linearized and fit to determine the constant $\kappa$.

When the sample bias is reduced, the servo must bring the tip closer to the surface. Repeated $I$ vs. $z$ measurements at different $V_S$ allows one to measure $\kappa$ and plot it as a function of $V_S$ ($\kappa$ has a dependence on the relative Fermi levels of the sample and tip). At low enough $V_S$, the tip will contact the surface (call this bias $V_{contact}$). The resulting $I$ vs. $z$ curve will deviate from an exponential due to interactions (bonding, van der Waals, etc.) between the tip and sample. The change in height, $\Delta z$, between $V_{set}$ and $V_{contact}$ provides a good estimate for the size of the tunnel gap.

## *2.2 Fabrication of a Digital STM Servo*

The STM servo is a specialized piece of equipment which is used to maintain a constant tunneling current at the desired setpoint $I_{set}$. Previously, an analog servo was used to control the RTSTM, but because of the flexibility and ease of reproduction of a digital servo, I designed and built it as a replacement.

Figure 16 shows the critical components of an analog servo. The servo maintains a constant tunneling current by making small adjustments to the tip-sample separation (typically a few angstroms). The tip is mounted on a tube piezo and is mechanically extended by applying a voltage across the piezoelectric material. The direction of the extension of the tip is typically referred to as the "z" direction (that is the convention will be used here).

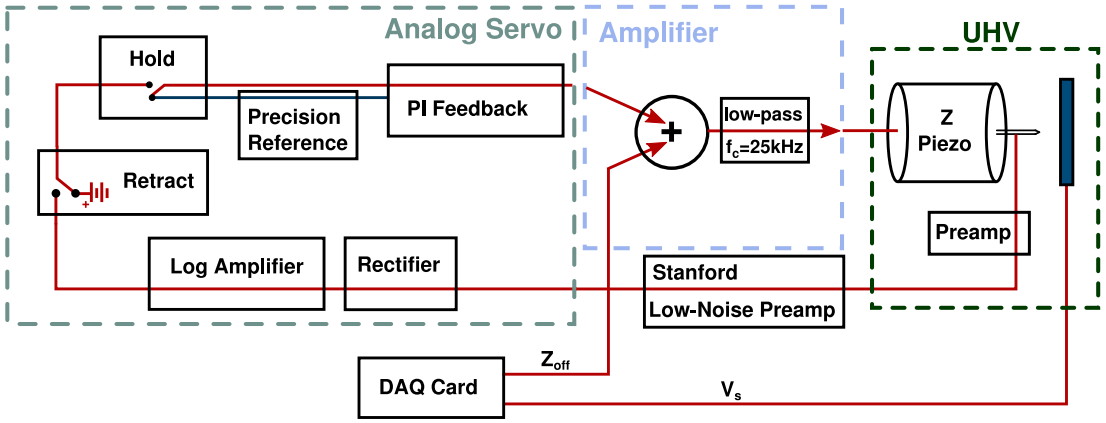


Figure 16: A diagram of a typical analog servo. The tunneling current is internally amplified (current → voltage, $0.1\,\mathrm{V}/nA$) by the preamp and amplified again outside the system by the Stanford preamp. The rectifier takes the absolute value of the voltage to remove the sign of the current, determined by the sign of the bias. The log amplifier linearizes the signal before passing it to the feedback loop. The precision reference provides a stable voltage to control the tunneling current setpoint $I_{set}$, and the error voltage for the feedback loop is generated as the difference between the reference and signal. The output of the feedback loop is added to the offset voltage and amplified. Finally the resulting voltage is applied to the z-piezo to control the height of the tip.

The analog servo is primarily a PI (proportional, integral) controller. It is desirable to have zero overshoot (slightly over-damped) in the step response so that the tip does not crash during normal scanning or approach. For this reason, the differential component was intentionally left out of the feedback loop because it can often lead to instability. If it were introduced into the feedback loop under the right conditions, it would improve the servo response, but optimal tuning of the feedback gains is not guaranteed for the wide variety of tip/sample work functions used.

The central problem of the analog servo is inflexibility. Each operation of the servo must be hard-wired into the circuit, making modification very difficult. In the next sections, I will outline the design considerations for choosing the components of the digital servo. Next, I will describe the core components of an analog servo and how a digital servo can be used to replace or improve each. Finally, I will discuss ways to improve the response of the servo using digital signal processing techniques, and present the results.

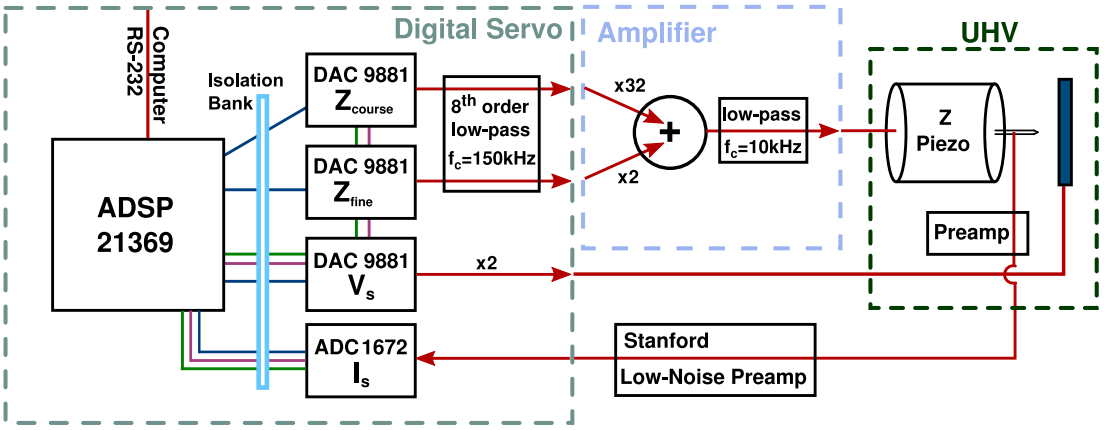


Figure 17: A diagram of a typical digital servo. Most of the components from the analog servo can be implemented in software. The digital servo has a digital signal processor (ADSP-21369) to handle the signal from the STM. An ADC-1672 analog-to-digital converter digitizes the current and the logarithm is computed in software by the DSP. The feedback is calculated from a software PID loop with gains that are adjustable on the fly. Three DAC-9881 digital-to-analog converters are on board for generation of an output signal. Two of them are summed with different gains for a high and low gain scan mode.

### 2.2.1 *"It's More Fun to Compute"* – Kraftwerk

In principle, choosing hardware for a digital servo is easy because most of the implementation is done in software; however, there are a few performance characteristics to consider before deciding which hardware best suits the application. Figure 17 shows a diagram of a digital servo, including the specific components I chose to use.

#### *2.2.1.1 Digital-Analog Converters*

The signal-to-noise ratio and bit resolution of the data converters define the resolution of the servo. For the digitization, I chose the ADC-1672 from Texas Instruments. This is a 24-bit data $\Delta - \Sigma$ converter which can be sampled at 625 kHz. The chip has an adjustable digital filter, which can be programmed to operate at single-cycle latency or fast response. The filter has adjustable data rates, however filter settings with lower sampling frequencies have a higher effective number of bits (more taps in the filter).

The filter characteristics of the data converter are extremely import for a servo application. Consider the situation in Figure 18. As the tip moves over atoms on the surface

of some sample, the servo must oscillate the height of the tip in order to keep a constant tunneling current. The frequency of the oscillation ($f_{osc}$) is defined by the scanning speed ($v$), and the phase of the response ($\phi$) is defined by the fixed latency ($\tau$) (in a digital servo) of the servo throughput (also called the group delay for digital filters). Because the latency of the servo is fixed, the phase of the response also depends on the input frequency. At low frequencies, the servo response will be approximately in phase. At higher frequencies, there will be a crossover frequency where the servo is 180° out of phase. The crossover frequency must be above the filter frequency at the input (set at the Stanford preamp).

The values for $f_{osc}$ and $\phi$ are given by:

$$f_{osc} = \frac{v}{a} \tag{39}$$

$$\phi = \frac{2\pi\tau}{T_{osc}} = 2\pi f_{osc}\tau = \frac{2\pi\tau v}{a} \tag{40}$$

where a is inter-atomic distance and $T_{osc}$ is the period of oscillations. When $\phi = \pi$, the servo response is 180° out of phase with the input and the system is unstable. Typical room temperature scanning speeds are on the order of $v \sim 100 - 300\,\mathrm{nm/s}$, so $f_{osc}$ is in the 1-5 kHz range. Therefore, for the phase to remain less than 90°, the overall latency (input-to-output) should remain under 50 $\mu$s.

Filter latency is important to consider when choosing any data converter. Many audio-quality converters achieve high bit rates and signal to noise by using a digital filter which require numerous samples at the input before a single value is digitized. As a result, the output is significantly delayed from the input. For home audio applications, the filter latency is not a problem; however, large latencies are intolerable for a servo. The ADC-1672 is not an audio analog-to-digital converter, but the filters must be set to a faster mode to reduce the filter latency. The trade-off for reducing the filter latency is that the effective bit resolution is reduced. Fortunately in the single-cycle mode, the converter still maintains roughly 20 bits of effective resolution, which is more than enough for this application.

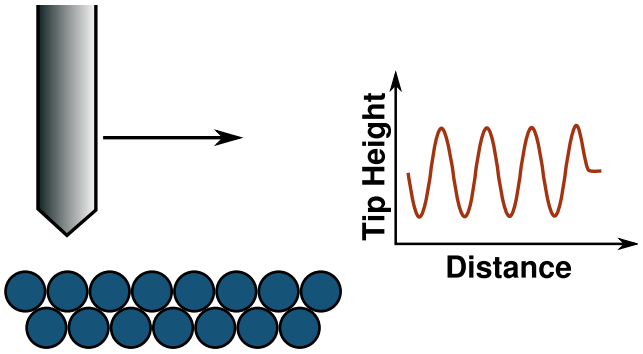


Figure 18: Scanning the tip over atomic corrugation creates a sinusoidal modulation of the tunneling current. The frequency of the oscillations define a maximum input-to-output latency for the entire servo before the servo response is 180° out of phase. This is important to consider when choosing digital converters as many high resolution audio converters have very high associated filter latencies.

For the outputs, I chose the DAC-9881 from Texas Instruments. These converters have a fast settling time and do not use a filter. Unfortunately, 18 bits of resolution is the highest that Texas Instruments offers in a non-audio digital to analog converter (DAC), but since we are using a gain to amplify our signal, we can sum two of them at different gains to increase our total resolution. The high gain DAC output goes into the STM with a total factor of 64 gain (results in ±160 V). The DAC-9881EVM (evaluation module) has an op-amp on board, which gives an outputs of ±5 V. A jumper on the evaluation module, adjusts the output to provide a factor of 2 gain (±10 V). The two signals get summed together, inverted (to double the gain) and applied to the z-piezo. The high-gain DAC ends up with a total gain of 64, or 160 V bipolar. The low-gain DAC has a gain of 4. In the 64/4 gain configuration, the total gain provides an effective 22-bit resolution over 320 V (from the gains, $16 = 2^4$ times the existing $2^{18}$). Thus, the voltage resolution is $V_{res} = 320\,\mathrm{V}/2^{22} = 76.3\,\mu\mathrm{V}$. Using a conversion factor of $20\,\text{Å}/V$, this corresponds to a z-resolution of $\Delta z = 1.5 \times 10^{-3}$ Å, while the resolution for the high-gain DAC is a factor of 16 larger, or $\Delta z = 2.4 \times 10^{-2}$ Å.

I also use the DAC-9881 to control the tip voltage. Numerous converters would fit this requirement since the tip is generally held fixed during imaging. During spectroscopy, the tip is swept through a voltage range so a reasonably fast update rate is helpful.

#### *2.2.1.2 The Brains*

With efficient programming, the whole servo could be created using a 32 bit microprocessor, but since flexibility is the ultimate goal of the project, I wanted something with some headroom. I chose to use a digital signal processor (DSP, ADSP-21369 SHARC) from Analog Devices. The SHARC line is a series of processors built for audio processing. The ADSP-21369 is a 400 MHz, floating-point processor. Floating point calculations are a luxury in the world of microprocessors, but they can greatly simplify code and increase the overall accuracy of the calculation. Additionally, the ADSP-21369 has two serial peripheral interface (SPI) buses, each with four individual chip select lines. This provides the capability for control of up to eight SPI devices. The servo currently has four data converters, and fig. 17 shows how they are connected to the SHARC.

SPI is a form of synchronous serial transfer. The interface consists of three wires: chip select (CS), serial data in our out (SDI/O) and the sample clock (SCLK). Unlike asynchronous serial, SPI can use arbitrary baudrates because the data is clocked. As a result, the transfer is accurate above 100 MHz clock speeds. The ADC-1672 will take clock speeds up to 20 MHz, while the DAC-9881 can handle a 50 MHz clock.

In addition to the three wires used for SPI transfer, the ADC-1672 has START and DRDY (data ready) bits. Before the data can be transferred over SPI, a start signal must be toggled from the DAI (or DPI) bus of the SHARC. The start signal initiates a conversion and flips the DRDY bit when the conversion is completed and ready for transfer.

The SHARC's interrupt timers are important for creating stable, jitter-free realtime servo loops. The interrupts for servo processes can be set to high priority, while the asynchronous main loop can be used for monitoring the serial line. Instructions sent over the serial line will not affect the interrupt-based refresh of the servo loop.

### 2.2.2 Trading Hardware for Software

#### *2.2.2.1 Data Acquisition Card*

Data acquisition cards are expensive equipment. In fact, a single multifunction card from National Instruments costs more than the entire digital servo build itself and since multifunction cards typically do not have enough analog outputs to control the tip bias, z offset, x position and y position, two cards are necessary. Because the servo *already* digitizes the current in order to compute the voltage which is applied to the piezo, data acquisition is as simple as creating a communication link between the computer and servo. Both cards can be replaced if two additional DACs are added to the schematic in 17, but we will not take that approach here.

Communication of data is done by asynchronous serial. The DB9 connector on the SHARC evaluation board is connected to an RJ45 jack. The computer receives data through its serial card. Fast baud rates (460.8 kbps) can be reliably negotiated over this line, and the Perle SPEED1 LE serial card can receive data up to 921.6 kbps. Communication is limited by the voltage level shifting required by the RS-232 standard. Onboard the ADSP-21369 evaluation kit, there is an ADM3202 RS-232 interface device, which takes the 3.3 V logic levels from the ADSP-21369 and shifts them to a 5 V level. The speed of this chip is limited to 460.8 kbps, so if higher speeds are required, this chip should be replaced. Other methods of data transmission were considered. Serial over USB seemed logical; however, the slow (1 ms) refresh rates of USB frames proved to be insufficient.

Data regarding the z-height of the tip is collected on the servo. Using the serial link, the controller computer polls the servo for the current value of the z-height. This value is relayed back to the computer and displayed on the screen. Because the scan frequency is slow compared to the frame rate of the servo (50-200 kHz), several values can be averaged together on board the servo by keeping an up-to-date ring buffer.

#### 2.2.2.2 *Retract and Hold*

Two of the simplest analog servo functions to implement digitally are retract and hold. In the analog servo, the feedback loop is *tricked* by switching the input line to some constant voltage above the reference point. This causes the feedback loop to see a high current on the input, so it continually withdraws the tip from the surface until it reaches its maximal retract distance. Using a digital servo, there is no need to trick the feedback loop. The servo maintains complete control of the z-position, so the feedback can simply be disabled and the tip withdrawn.

The hold in an analog servo is generated by setting the input to the feedback loop equal to the reference current. Because this results in a stable zero error voltage, the tip position is not changed. Again, the desired function is more easily achieved in the digital servo by simply disabling the feedback loop.

#### 2.2.2.3 *Log Amplifier*

PID loops are only stable in systems where the response is linear. In STM, the dependence of the current $I$ on the tip height $z$ is well defined as,

$$I \propto e^{-\kappa z}. \tag{41}$$

Therefore, the linear response with $z$ is achieved by taking the log of the input $I$. Analog servos use logarithmic amplifiers, but we can remove this component from the circuit by taking the log numerically. Often this is done either by using a lookup table or a polynomial expansion, however the SHARC math library has its own built in log function. The current setpoint $I_{set}$ should be kept well above zero. Operationally, $I_{set}$ should remain in the 0.1-1.0 V range in order to stay well inside the saturation limits of the ADC (discussed further in section 2.2.2.5).

#### 2.2.2.4 *Rectifier*

The STM requires the ability to scan with both positive and negative sample biases ($V_s$). The choice of $V_s$ determines the direction of flow of the current. As far as the PID loop is concerned, the sign of the current is irrelevant, as the magnitude response will be the same for changes in the height of the tip. More importantly, linearization of the signal by the log function requires a positive input since both high positive and negative currents indicate that the tip should be moved farther from the surface. In analog servos, a precision rectifier is used. This function can easily be replaced in a digital servo. If a negative current is measured, the incoming signal can be multiplied by -1 (or the absolute value can be used).

#### 2.2.2.5 *Precision Reference*

The current setpoint $I_{set}$ in an analog servo is achieved by using a precision voltage reference. These devices are designed to maintain a steady, noise-free DC voltage, and the PID uses it as a point of comparison to generate the error signal. Usually, these are statically implemented integrated circuits. The reference is not easily changed, so $I_{set}$ is a fixed value for the gain of the pre-amp. The digital servo creates a reference signal by simply choosing a digital value. The point of comparison can be arbitrary, so long as it is held constant while the servo is running. This is extremely flexible, as the current can be adjusted to any value within the measurement range of the ADC; however, caution should be taken when selecting $I_{set}$. If there is insufficient measurement range above and below $I_{set}$, the servo will easily saturate, greatly affecting the speed of the response. Because the ADC cannot exceed its measurement range, the maximum error (for the tip being too close to the surface) is $E_{max} = \ln(I_{set}) - \ln(I_{max})$. Because the maximum measurement is 2.5 V, the response for a setpoint of 0.1 V is roughly 3.5 times better than for a setpoint chosen at 1.0 V (as determined from the maximum error).

Though I describe $I_{set}$ in terms of a voltage, the physical tunneling current can be determined from the gain of the internal current preamp (0.1 V/nA) and the external low-noise

preamp (typically set to a gain of 100). Thus, 1.0 V at the input of the ADC is:

$$1.0\,\mathrm{V} \times \frac{1\,\mathrm{nA}}{100 * 0.1\,\mathrm{V}} = 100\,\mathrm{pA}. \tag{42}$$

The minimum ADC measurement in the digital servo is artificially cutoff below 1 mV to prevent the logarithm from blowing up when the tip is not tunneling (zero tunneling current is physical, but it creates an infinitely large error when the logarithm is applied). Alternatively, $E_{max}$ could be restricted such that the maximum error is equal when the tunneling current is either too high or too low. In view of this, DC offsets in the tunneling current measurement on the ADC could potentially destroy the stability of the loop. It may be important to periodically remove offsets in order to ensure equal response.

#### *2.2.2.6 PID Loop*

One of the greatest benefits of using a digital servo is the ability to tune the parameters of the PID. In software, the basic form of a (velocity) PID loop is given by:

$$E_i = \ln(I_{set}) - \ln(I_i) \tag{43}$$

$$Z_i = Z_{i-1} + K_P(E_i - E_{i-1}) + K_I \times T_s \times E_i + K_D\left(\frac{E_i - 2E_{i-1} + E_{i-2}}{T_s}\right) \tag{44}$$

where $K_x$ are the PID gains, $I_i$ are the measured values of the current, $Z_i$ are the outputs and $E_i$ are the values of the error signal. In this formulation, the integral is accumulated in the $Z_{i-1}$ term, and the derivative term is the 2nd derivative of the error. Typically, $T_s$ (the sample time) can also be absorbed into the gain parameters. This will change the relative proportionality of $K_P$, $K_I$ and $K_D$, but does not otherwise change the algorithm.

Analog implementations of PID loops often exclude the differential part of the feedback (making them PI loops). Because the gains are hard-wired and cannot be changed, overdamping the step response ensures that the height will not overshoot and crash into the sample. In contrast, users can tune digital servos by hand. An RS-232 link to the computer

permits information transfer even while the tip is in tunneling range. A step response can be applied by periodically stepping $I_{set}$. The gains can be tuned by eye (plotting the step response) or using the Ziegler-Nichols method. By tuning the PID gains, the differential term can be slowly introduced into the loop. The differential component can help to improve servo stability and reduce the response time, acting as the proportional term for the predicted output.

#### *2.2.2.7 Adaptive Digital Filtering*

Future improvements to the digital servo could be done by better linearizing the input signal. PID loops achieve their greatest stability when changes in the output produce a linear response at the input. Using the log function, we have effectively modeled the response of the system and linearized the response; however, physical limitations of the STM hardware produce nonlinearities as well. For instance, piezos have a frequency response curve which introduces gain at the resonance peak of the piezos. In practice, some groups have measured the full transfer function of their STM and removed nonlinearities by using techniques borrowed from active noise cancellation [Paillard 1998]. Using adaptive filtering, one can create filters with $> 2^{10}$ taps and drastically improve the PID stability.

### 2.2.3 Results

## *2.3 Python Open Source Scanning Microscopy (POSSM)*

In the course of my lab work, I wrote new software to run the RTSTM. Previously, the in-house STM code had run on DOS-based computers. The code was designed to run with specific hardware, which had long since been outdated. In order to update our computers and equipment, new code would be required.

We decided to use Linux as our base operating system. The Linux kernel is highly configurable, and since version 2.6, has included some kernel flags which boost realtime capabilities. Specifically, when compiling a kernel to use as the STM controller, one can build a fully preemptable kernel. The controller code is set to boost its own realtime priority

when run as root so that steady operation will not be inhibited by kernel interrupts. This modest change was tested and found to significantly improve latencies during waveform generation, when solid timing is critical to producing a uniform STM trace.

The majority of the code is written in python. Though python is a high-level interpreted programming language, it has many attractive advantages including: excellent organization of code through object oriented programming (OOP), rapid code development from the help of easy to read/write code without unnecessary syntax, simple interfacing with compiled C/C++ modules, a wide user base with open source scientific libraries and a command line interpreter.

The code is meant to run on two computers simultaneously, though it may be run on a single computer if desired. The code is divided into a client/controller setup. The client connects to the controller via sockets over Ethernet. Scans are sent to the controller and executed. While the controller is performing the scan, data is streamed back to the client for display. Completed data is stored in the popular NetCDF format, so that it can be opened and accessed by any number of programs.

After completing the first versions, I open sourced the project under the General Public License (GPL) v3. The code is permanently hosted at `http://code.google.com/p/possm/`. The analog servo runs under the v1.0 release in the tags directory. Any new revisions are made to run specifically with the digital servo. The code can be freely downloaded and modified, as per the open source standard. The DSP++$^{TM}$ code for running the digital servo is also included with the POSSM software.

### 2.3.1 Directory Structure

The file directory of the POSSM project is as follows:

**- tags**
**+ v0.99**

**+ branches**
**- trunk**
**+ client**
**+ controller**
**+ icons**
**+ servo**
**+ shared**
**. setup.py**
**. socketdaemon.py**
**. stm.py**

The tags directory contains past releases of the POSSM program. Inside the folder *v0.99*, is the last version used with the analog servo. The current version of the program is located in the *trunk* directory. There are three python files in the *trunk* directory. The file *setup.py* is a build script for some C-extension files that interface with COMEDI. They must be locally compiled in C on the controller computer so that python can build them into a module. To build the files with gcc, use:

```
# python setup.py build
```

```
# python setup.py install
```

Now that the C-extensions have been built, the controller can be started. Execute the following command in terminal:

```
# python socketdaemon.py
```

For testing, the socketdaemon can be started using the *–fake* flag. If it starts correctly, it should indicate that it is waiting to receive a connection from the client.

The client program can be started on the same, or different computer by simply executing

```
# python stm.py
```

in the trunk directory. If the interface does not open, make sure the following packages are installed:

- ⋆ python-numpy
- ⋆ python-Scientific
- ⋆ python-scipy
- ⋆ python-matplotlib ≥ 0.98.3
- ⋆ python-wxgtk ≥ 2.8

Once the interface opens, you will be looking at the main page of the STM interface.

The other folders inside *trunk* contain the actual source files needed to run the client and the controller. The *shared* directory contains python files that are used by both the client and the controller. Of note, is the *shared/worldsettings.py* file. Numerous program settings can be adjusted by changing parameters in this file.

### 2.3.2 Basic Operation

The POSSM interface is setup in a notebook-style configuration. Each new scan opens up a new notebook page automatically. The main window contains all of the parameters for scanning. The list of *scan types* is an expanding tree, which allows users to select scans and modify the parameters of each type of scan. As different lists of a scan are selected, the parameters will be displayed in the grid. The values can be changed from the grid by double clicking in the box. For help on what each parameter means, simply click on the item in the grid and press the F1 key. An explanation will be displayed in the dialog below.

Before beginning a scan, connect the client interface to the controller. Make sure the controller is running, and enter the network name or IP address of the controller computer in the box above the *connect* button. Press the connect button to connect to the open sockets of the controller. At this point, scans can be sent to the controller.

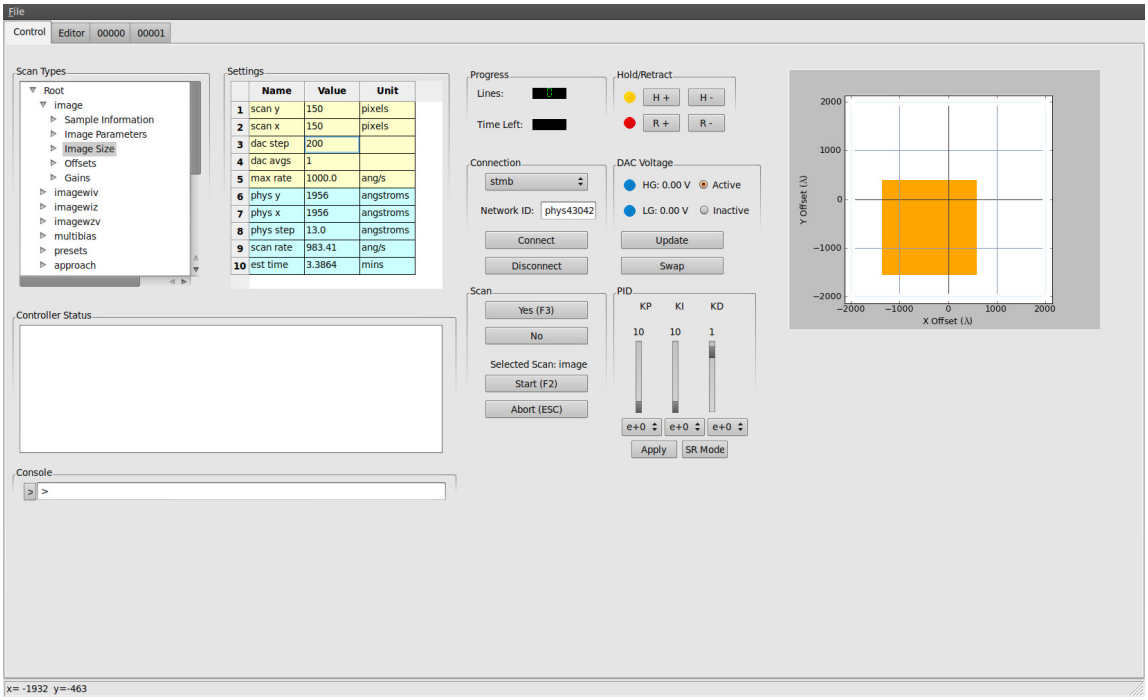


Figure 19: The main interface of POSSM. The scanning software is laid out in a notebook-style arrangement. Additional pages are opened when new scans begin. This client interface connects to a computer running the controller software so that scans can be run remotely from any computer, without the need to install hardware drivers.

To send a scan, click on a scan within the tree control (top left, Fig. 19). Highlight the scan that you wish to perform and press the start button. In the dialog box, the controller will indicate that it has received the scan and ask if you want to continue. Click yes or type yes into the console at bottom. The scan will begin shortly, and data will be displayed as it is streamed from the controller. Image scans can be aborted at any time by pressing the abort button on the interface.

The controls on the right are used to control the digital servo. At the top, there are hold and retract buttons. Below that, the extension voltages of the DAC for the high gain (HG) and low gain (LG) are displayed. The residual DC voltage from the low gain z control can be zeroed and swapped onto the high gain DAC by pressing the *swap* button. The PID gains are adjusted by the sliders on the lower right. Each gain can be adjusted individually, and set while the servo tunneling. None of these controls should be used while the system

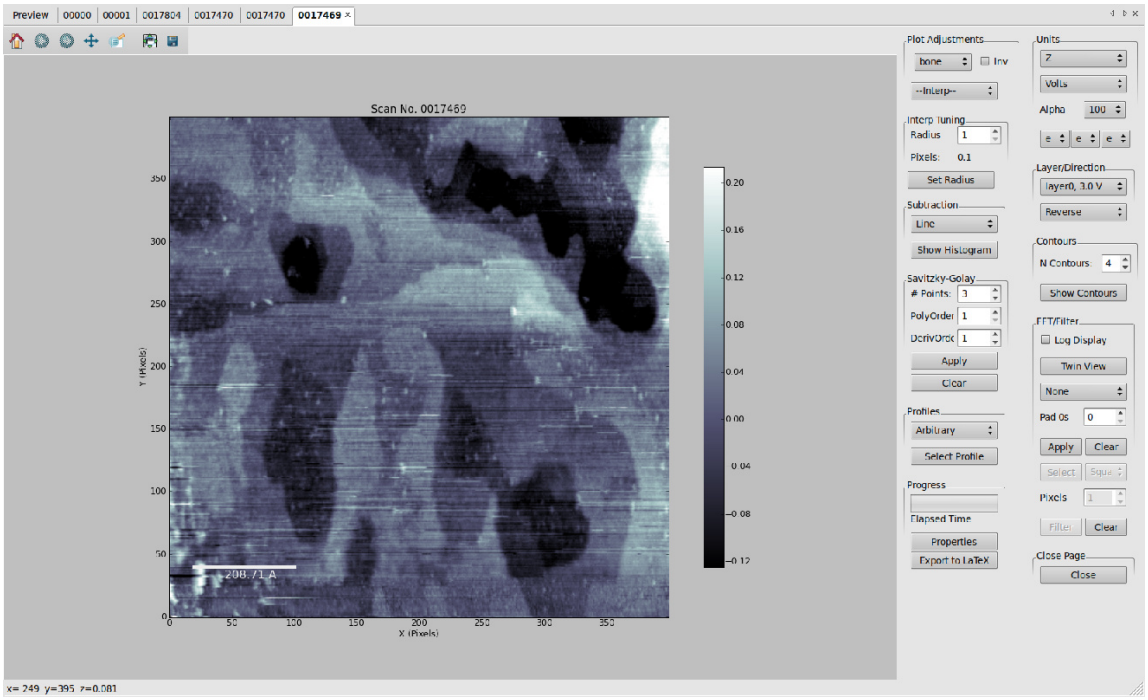


Figure 20: The interface for the viewer and scan window. On the right side of the window, there are many tools available for image processing and data analysis. Most importantly, one can do line and plane subtraction while scanning, adjust the z-height based on a histogram of the image and take height profiles of the surface.

is scanning.

### 2.3.3 Scan Window

When a new image scan begins, a new image window will open. As the scan continues, the display will update for each line that is received. On the right, there are some basic tools for data analysis. The progress bar indicates how many lines of data have been received out of the total number in the scan. The interface also provides the capability to save images directly from the interface, or insert them into the latex code of the built-in virtual labbook.

For more information regarding the POSSM project, refer to the wiki page at `http://code.google.com/p/possm/` or the included documentation.

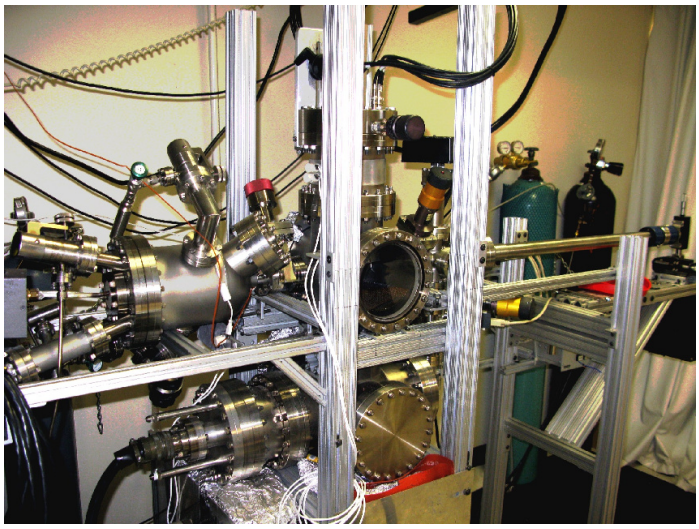

Figure 21: An image of the rapid characterization chamber. Samples are transferred into the system through the load locks (lower right area, not visible). The double load-lock design greatly reduces the transfer time into UHV from ~1 day (for single load lock systems) to ~1 hour. The magnetically coupled linear-rotary feedthrough transfers samples into the main chamber, where they can be characterized by using LEED and AES. If samples require heating or growth, they can be moved further into the RF induction furnace (upper left).

## *2.4 Rapid UHV Characterization and Growth Chamber*

This section is written primarily for the benefit of those who wish to use the rapid characterization chamber (RCC). It details the capabilities of the chamber, and also covers my contributions to the fabrication of equipment and computer control mechanisms.

### 2.4.1 Design and Operation

The primary function of the RCC is to reduce the UHV loading time for samples, so that low energy electron diffraction (LEED) and Auger electron spectroscopy (AES) can be performed more quickly than most ultra-high vacuum (UHV) experiments allow. The RCC uses a double load-lock design, with Pfeiffer Balzers TMU-064 turbo-drag pumps at each stage. The first load-lock is the "dirty vacuum" stage, which is typically maintained at high-vacuum, $10^{-6} - 10^{-7}$ Torr. For sample loading, the lower load-lock is vented to dry $N_2$ gas. The sample is then mounted in a slot loading sample holder, and transferred into the load-lock. Once the load-lock has pumped down below $1 \times 10^{-6}$ Torr (typically 30 minutes

to an hour, depending on how recently the system was baked), the sample can be moved up to the upper load-lock and the lower load-lock is isolated again.

The upper load-lock acts a buffer to the main chamber. Because the main chamber is valved closed during the transfer between load-locks, it always remains isolated from any surfaces that were directly exposed to atmosphere. Thus, water vapor from the transfer does not generally affect the base pressure of the chamber. Additionally, the vacuum conductance between the upper load-lock and the chamber is small, so that even when the gate valves are opened, the pressure is not strongly affected.

The main chamber is equipped with two pumps. At the bottom, there is a 200 L/s ion pump, and on the side (lower left side of Fig. 21), there is a titanium sublimation pump (TSP). The ion pump remains in constant operation, while the TSP is used intermittently to recover the pressure after baking, filament outgassing, etc. The base pressure of this chamber consistently remains at $\sim 10^{-10}$ Torr.

In the center of the chamber, there is a RVL2000 LEED/AES device from LK Technologies (shown in Fig. 22a). This equipment can be used to characterize the structural and chemical properties of *clean* samples which conduct to the edges (insulating samples electrostatically charge from impinging electrons and destroy the measurement). Low energy electron diffraction and Auger electron spectroscopy experiments are discussed further in the next sections. Generally, freshly prepared graphene samples will display a pattern in LEED (usually diffuse, scattered from impurities on the surface). Samples which have been in air for longer than a day likely need to be cleaned in vacuum before LEED measurements can be performed.

For sample cleaning and graphene growth, the RCC is equipped with a custom built radio-frequency (RF) induction furnace (upper left side of Fig. 21). The furnace is separated from the main chamber by a gate valve, and can be used to clean and grow graphene samples. The furnace is equipped with a UHV leak valve, for stagnant atmosphere growth. There is also a quadrupole mass analyzer (QMA) which can be used for monitoring the

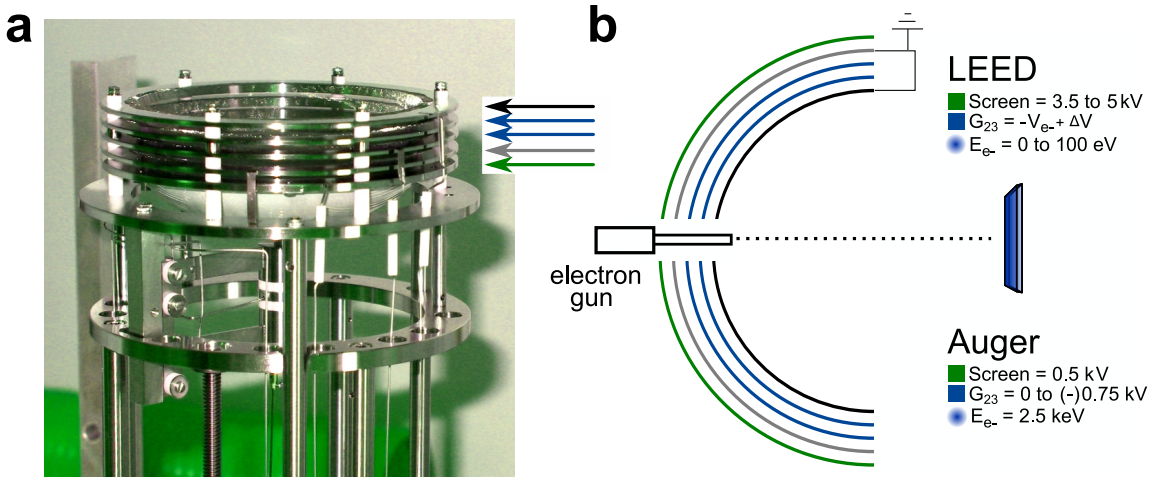


Figure 22: (a) An image of the LK LEED/Auger system. At the top are the grids. The electron gun is in the center of the spherical grids. The whole device can be translated to set the sample at the center of the grid sphere. In LEED mode, electrons are diffracted off of the surface. The voltage on $G_{23}$ filters the inelastically scattered electrons so that the diffraction pattern stands out on the phosphor screen. Similarly, $G_{23}$ in Auger mode acts as a high pass filter; however higher energy electrons from the gun knock out core electrons from atoms at the surface. Ionized atoms become doubly-ionized when the relaxation of higher level electrons drop to fill the vacant core-level state and a higher level Auger electron is knocked out. The detection of these events produces peaks in the collected current which are chemically sensitive. (b) A schematic of the LEED/Auger with typical operating voltages. The same equipment that is used for LEED can be operated with different voltages as a retarding field analyzer (RFA) Auger electron spectroscopy system.

mass spectrum of the residual gas in the vacuum, during or after heating. The interior of the furnace is all-carbon, and is capable of temperatures higher than 1800 °C.

### 2.4.2 LEED

Low energy electron diffraction is an excellent resource for obtaining sample information fairly quickly. With very clean, ordered samples, LEED patterns can be resolved and imaged in under and hour. For samples that have not been heated in UHV, patterns are generally diffuse and difficult to find.

LEED is an extremely surface sensitive technique. The low energies used (typically, 30-150 eV) and the large scattering cross section of ion cores (1 Å) mean that electrons cannot penetrate deeply into the material before being scattered. The wave nature of electrons causes them to diffract off of ordered surfaces via elastic scattering. Inelastically scattered

electrons are filtered by a retarding potential $-V_{e^-}+\Delta V$ at hemispherical grids two and three ($G_{23}$ in Fig. 22b). The retarding potential is set slightly below the kinetic energy ($E_{e^-}$) of electrons coming out of the electron gun. Electrons that are elastically scattered from the surface pass through and are accelerated into a phosphor screen. The glowing spots from electrons hitting the screen are the diffracted pattern (or reciprocal space vectors), which is uniquely characteristic of the atomic arrangement at the surface.

LEED systems use filaments with high electron emissivities to form an electron beam. Standard LK RVL2000 systems come with thoriated tungsten filaments. Tungsten filaments must be run at fairly high temperatures (and high filament currents, $\sim 3.2$ A) in order to get the required emission current ($\sim 1$ mA). Consequently, there is a large incandescent spot reflected from the sample back onto the screen. We have since replaced that filament with a $LaB_6$ (lanthanum hexaboride) filament, which operates at lower temperatures. Users should be aware that this filament must be used in a UHV environment ($< 10^{-8}$ Torr) and should not be operated continuously above a filament current of 1.8 A. The crystal easily acquires a surface coating if it is vented to air, and may require brief operation at $\sim 2.0$ A to get emission initially started. During this outgassing time, the emission current should be monitored and kept below $\sim 1.5$ mA by adjusting the filament current.

### 2.4.3 Auger

The LK RVL2000 system can additionally be operated as a retarding field analyzer (RFA) for Auger electron spectroscopy. AES uses higher energy electrons (2.5 kV) than LEED because the principle of operation is quite different. Nonetheless, the same hardware in LEED can be used as an RFA to acquire Auger spectra.

#### *2.4.3.1 Theory of Operation*

When operating in RFA mode, $G_{23}$ is used as a high pass filter by applying a voltage $V$ to the grids, which repel the inelastically scattered electrons. Electrons with energies above the pass energy $V$ are allowed to reach the phosphor *collector*, and produce a measurable

current $I$. The collector current is dependent on the scattered electron energy distribution $N(E)$ by [Chung 2001]:

$$I = \int_{ev}^{E_{max}} N(E)\, dE, \tag{45}$$

where $E_{max}$ is the maximum scattered electron energy. Because $N(E)$ is the quantity of interest, the Auger electronics use a lock-in amplifier to measure the differential signal,

$$\frac{dI}{dE} = -N(E). \tag{46}$$

The measurement of $N(E)$ provides chemically unique information about surfaces. Electrons impinging on the surface knock out core-level electrons from atoms at the surface. The ionized atoms undergo de-excitation when the electron vacancy is filled from other electron states of higher energy. The energy is released when higher energy electrons relax to fill the core-level vacancy ejects a so-called "Auger electron" into the vacuum. The scattered electron distribution $N(E)$ reflects the Auger energy loss peaks.

Unlike the cylindrical mirror analyzer (CMA) design (a band-pass, differential detector) for AES, the RFA suffers from a rather low signal-to-noise. The peaks in RFA, despite being locationally correct (in energy), also fall on top of a rising background of secondary electron emission [Somorjai 1980]. This can be fit and subtracted out, but it is important to have enough signal so that it is not over-shadowed by the background. Nonetheless, RFA designs are most convenient in the fact that they share the same hardware as LEED, making it a widely available technique. Despite the deficiencies of the RFA, the resolution and the scan speeds are good enough for most every-day applications.

AES is a useful technique when studying epitaxial graphene, not only to measure the composition and cleanliness of a surface, but because attenuation models have been fit which can estimate the graphene thickness (refer to the thesis work of Tianbo Li).

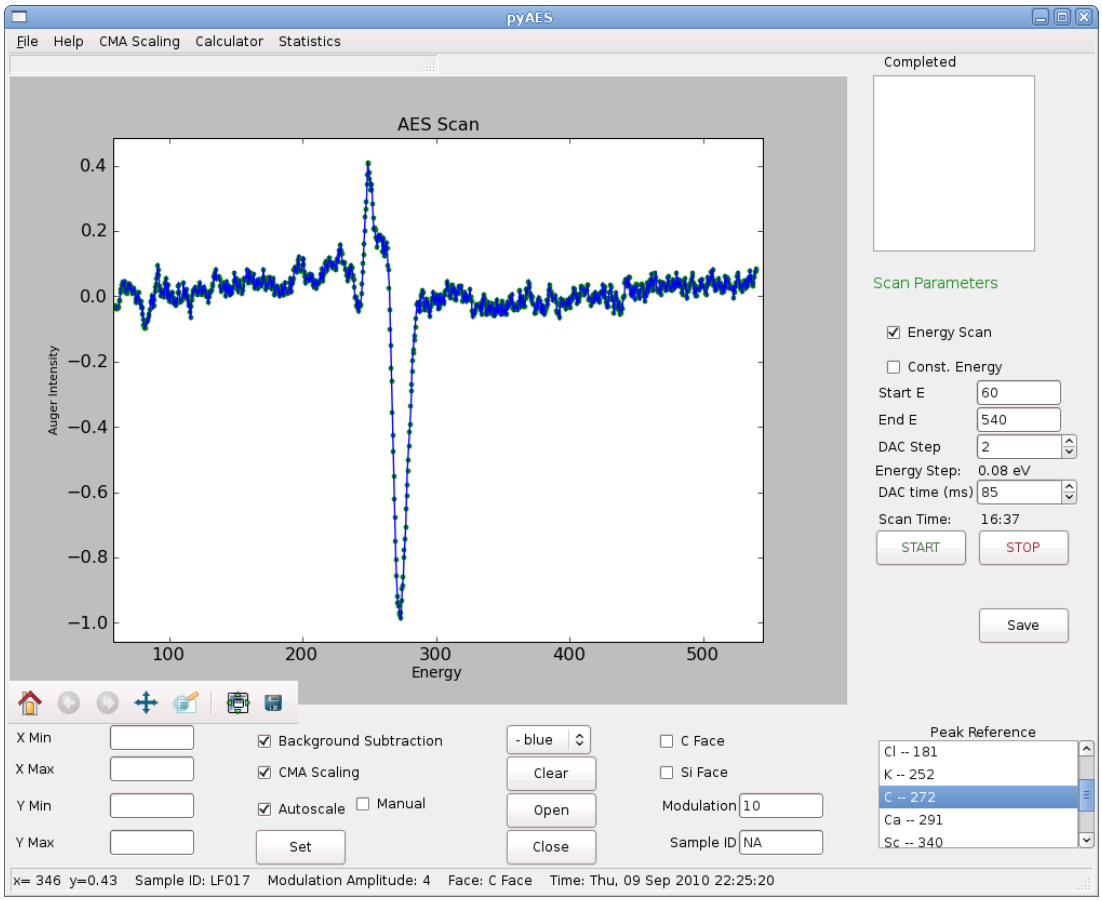


Figure 23: An screenshot of pyAES, Auger control program. The large Auger peak shown is a graphitic carbon peak. The program interfaces with a data aquisiton card which controls and measures the AES signal from the control electronics.

### *2.4.3.2 Control System*

The LK Auger system is controlled by the pyAES program. This program is custom for the LK hardware, and uses a National Instruments (NI) Multifunction DAQ PCI card for measurement and control. The NI card is controlled through the open source COMEDI library with extensions to python. The pyAES program is written in python, and the interface is created using WxPython and the GTK widgets.

The program normally operates in *energy scan* mode. The pass energy is swept over the range specified by *start E* and *end E* at the specified step size. At each energy step, there is a settling time which is designated *DAC time*. If the DAC time is not long enough, the lock-in will not fully settle and the Auger peaks will be additionally broadened. Typically, an 85 ms

DAC time is sufficient, but users can tweak this depending on how fast the measurement needs to be done.

The second mode of operation is *constant energy*. In this mode, the electronics remains at the start E and records the Auger intensity as a function of time. This is useful for tweaking the settings on the electronics in order to get the highest possible signal.

The *background subtraction* checkbox attempts to fit the rising background from secondary electrons and remove it from the spectrum. The peaks can also be scaled to match the size of peaks on a CMA system using the *CMA scaling* checkbox. I also wrote a second version of pyAES so that it could be used to control the CMA in the RTSTM system.

### 2.4.4 RF Furnace

In principle, graphene growth on silicon carbide is a very simple procedure; however, producing high quality films requires accurate control of high temperatures and a pure, reproducible growth environment. Following established low-vacuum methods developed in the deHeer lab at Georgia Tech, I wanted to design and produce a UHV furnace to explore the parameter space of graphene growth by the thermal decomposition of silicon carbide.

#### *2.4.4.1 Materials*

Materials to be used in the furnace have to meet several stringent requirements. First, we expect that temperatures will exceed 1600 °C. Regular growth temperatures routinely exceed 1300 °C, and by using a well enclosed furnace and an inert atmosphere to supress the evaporation of silicon, the growth temperature can effectively be increased even further. In order to avoid sample contamination, the material on the inside of the furnace must have a low vapor-pressure at elevated temperatures. Furthermore, the material must not endlessly absorb silicon vapor from the growth so that the hot walls of the furnace can act as a reflecting boundary. Additionally, the material used must also be a good conductor so that it can be heated by induced currents from the furnace coils.

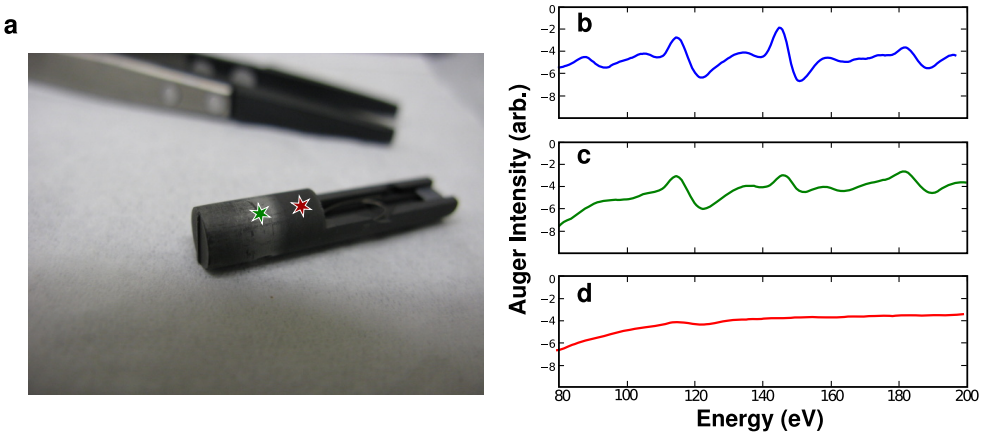


Figure 24: (a) An image of the graphite sample holder. Green and red stars mark where Auger scans were taken in (c) and (d) respectively. The gray part at the back of the sample holder is molybdenum which was evaporated from the furnace suscepter. (b) A reference scan on a piece of molybdenum. (c) An Auger scan on the back of the sample holder showing molybdenum evaportion on the back. (d) An Auger scan on a clean graphite region.

The only metals which potentially fulfill these requirements are refractory metals. Unfortunately, refractory metals are quite challenging to machine. Molybdenum and tungsten are hard, brittle metals, though molybdenum is more readily machineable than tungsten. Unfortunately, its vapor pressure is roughly $\sim 10^{-7}$ torr at 1600 °C. This pressure is undesirable, and is likely worsened by the 83% Mo – 17% C eutectic which lowers the liquid transition temperature by 400 °C [Brewer 1990]. Also, molybdenum and other refractory metals likely cannot be used inside a furnace environment due to the low temperature formation of stable silicide ceramics. This would continuously deplete the growth environment of silicon vapor, as the walls became "sinks." The first version of the furnace attempted to circumvent this by using a molybdenum susceptor with an interior graphite lining. The interior graphite protected samples from molybdenum contamination, and the formation of SiC on the walls produced a reflecting boundary due to the equal vapor pressure of the walls and the sample.

At higher temperatures (1600 °C), the molybdenum began to evaporate slightly. This is evident in fig. 24a. The gray region is part of the sample holder that was not enclosed inside the graphite furnace insert. Figure 24b shows an Auger spectrum on a piece of

molybdenum foil. Clearly, the matching spectrum in fig. 24b shows that the end of the sample holder has accumulated molybdenum, while the region that was inside the furnace (fig. 24c) managed to stay clean.

In light of this, different materials needed to be considered. Tantalum has a higher melting point that molybdenum (3017 °C compared to 2623 °C for Mo), so we tested this as well. Experimentation with this material led to additional unforseen problems. When heating tantalum to high temperatures in vacuum, sulfur migrates out of the material. We began finding sulfur contamination on our samples after we started using a tantalum sample holder. Scanning the sample holder using Auger revealed a large peak at 152 eV, which is the primary sulfur peak. Additionally three peaks at slightly higher energies were present, which are the lowest energy tantalum Auger peaks. After heating the sample holder for several hours at 1500-1600 °C, we observed a small reduction in the sulfur peak; however, the large sulfur peak always persisted even after attempts at outgassing in UHV. This came as a surprise, given the rated 99.9998% purity quoted from the manufacturer, and in fact, we tested tantalum foil from another high-purity vender, but the results were reproduced. At that point, we deemed refractory metals unsatisfactory for this application and instead opted for an all-carbon furnace.

Originally, I had thought it best not to use carbon (particularly at the front of the furnace). The immoderatly high spectral emissivity of carbon would seriously decrease the efficiency of the furnace, which is especially of concern regarding thermal gradients on the interior. Because the sample holder is inserted from the front, the face of the furnace must remain open during transfer. Power is lost through radiation from the unshielded end of the furnace and dissipated by conduction through the walls of the vacuum.

These issues aside, I found the carbon suscepter to have several beneficial qualities. 1) The design is simplified, requiring only a graphite rod for the furnace, a graphite rod for the sample holder and alumina ($Al_2O_3$) tubes for radiation shielding. 2) The graphite is directly heated by the induction coils and has a low heat capacity, resulting in a low latency

between the application of power and the increase in temperature. This makes PID control much simpler and more accurate. 3) If the furnace is reasonably enclosed, the inside walls of the furnace can become rich with Si and form SiC. This can be useful because it provides an alternate source of silicon pressure, which slows down the growth process. Special care must be taken with graphite furnaces not to allow particles of amorphous carbon to drop onto the surface. Although the furnace is horizontally mounted for alignment with the transfer system, we have found that this can be avoided by simply rotating the sample so that particles from the furnace wall do not drop directly onto the SiC (0001) or (000$\bar{1}$) faces.

In making the new furnace, we used a high-purity grade from Poco Graphite Inc. The DFP-2 semiconducting grade was selected for its high density, minimal open porosity (should reduce outgassing), high purity (99.9995%) and low resistivity (1500 $\mu\Omega$-cm). All newly machined graphite parts should be ultrasonically cleaned in methanol for 15 minutes, then ultrasonically cleaned again for 5 minutes in deionized water. Once placed in vacuum, the graphite should be outgassed at high temperatures for at least an hour.

#### *2.4.4.2 Performance*

The performance of the furnace was calculated before building to estimate the size of the RF power supply that we would need. The "hot zone" of the furnace is a cylinder about 1.5 in long by 0.5 in in diameter. The face of the furnace is completely open, and it is good to approximate the radiating surface as the inner diameter of the alumina radiation shielding. The long axis of the furnace will have significantly higher radiation shielding because it is surrounded by an alumina tube. This can be estimated by dividing the power lost off of that wall by a radiation reflection factor. The total power required to operate the furnace in steady state for a given temperature is the sum of power losses by radiation and conduction.

Conduction is primarily responsible for power dissipation at the lower temperatures (20-900 °C, blue region of Fig. 25). Above ~800 °C, emission in the visible spectrum

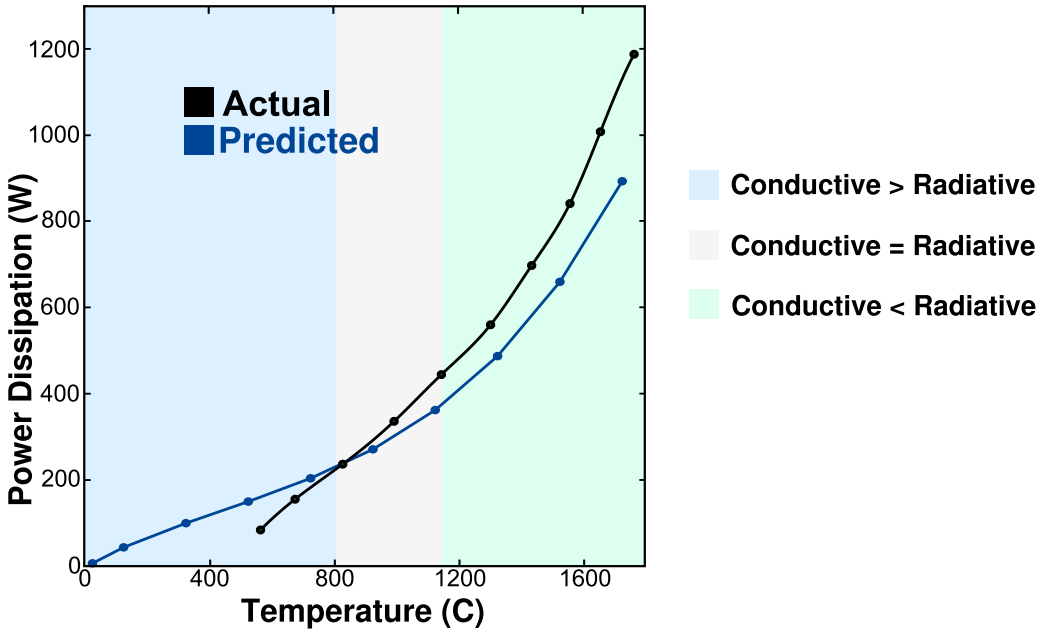


Figure 25: Calculated and actual power losses in the all-graphite furnace. At lower temperatures, the furnace loses efficiency mostly from conduction, but as the temperature, $T$, is increased in the furnace, the $T^4$ dependence of the blackbody radiation becomes the primary source of power dissipation. The predicted power losses diverge slightly from the actual at low temperatures. Conductive losses are significantly more difficult to predict.

becomes apparent. Around 1150 °C radiation losses become the dominant source of power dissipation and become increasingly more significant at higher temperatures.

The peak power necessary to heat an object not only contains the power required for steady state operation, but the heat capacity of the material and the desired heating rate should be taken into account as well. Following the calculations, we decided that a 2 kW power supply would be sufficient to provide the range of temperatures required so we chose an Ameritherm Easyheat 2 kW power supply.

#### *2.4.4.3 Control*

To monitor the temperature of the furnace, we have applied several methods. The first method we attempted was a type C (W-5% Re/W-26% Re) thermocouple (TC). A hole was drilled in the back of the furnace, and the thermocouple junction was adhered in place using a high-temperature graphite epoxy. Unfortunately, the placement of the thermocouple

must be inside of the furnace coils where RF pickup is the highest. The noise can be filtered effectively using a low-pass filter; however, the DC thermocouple signal is on the order of 20 mV while the pickup from the coils is on the order of ~10 V. A better solution is to use a pyrometer for temperature measurement.

We use a Mikron MI-GA140 infrared pyrometer for measuring temperatures. This pyrometer has sensitivity in the range of 300-3300 °C, which is excellent for our growth temperatures. The temperature is read using a computer through an RS-232 interface. It is important to make sure that the emissivity of the heated material is set on the pyrometer. The pyrometer operates in the range of 0.7-1.8 $\mu$m. Graphite is an excellent blackbody and therefore has a high emissivity. Measurements of Poco EDM-3 (a graphite grade with similar grain sizes) produce emissivities of 0.8-0.85 between temperatures of 1000-1500 °C [Biasetto 2008]. Emissivity can be adjusted through the RS-232 interface to calibrate the measured temperature.

We use an SRS IGC100 ion gauge controller to monitor the pressure in the chamber. The controller has an analog output for the pressure which sets 1 V per decade in units of Torr.

#### *2.4.4.4 pyTherm*

To control the operation of the furnace, I wrote a control program called pyTherm. This program uses a custom hybrid algorithm which combines PID feedback with the stability of a calibration curve. By incorporating a calibration curve into the control, we can achieve extremely stable temperatures (±1° C at $T_{max}$) with virtually no overshoot (within the range of error). The algorithm also achieves stable linear ramps by initially generating feedback error based on the slope of the temperature vs. time curve.

Overshoot is eliminated by incorporating a calibration curve of the supply current vs. temperature. Because the instantaneous power at a given temperature is larger for heating than maintaining the temperature, pyTherm avoids overshoot by instantly dropping to the

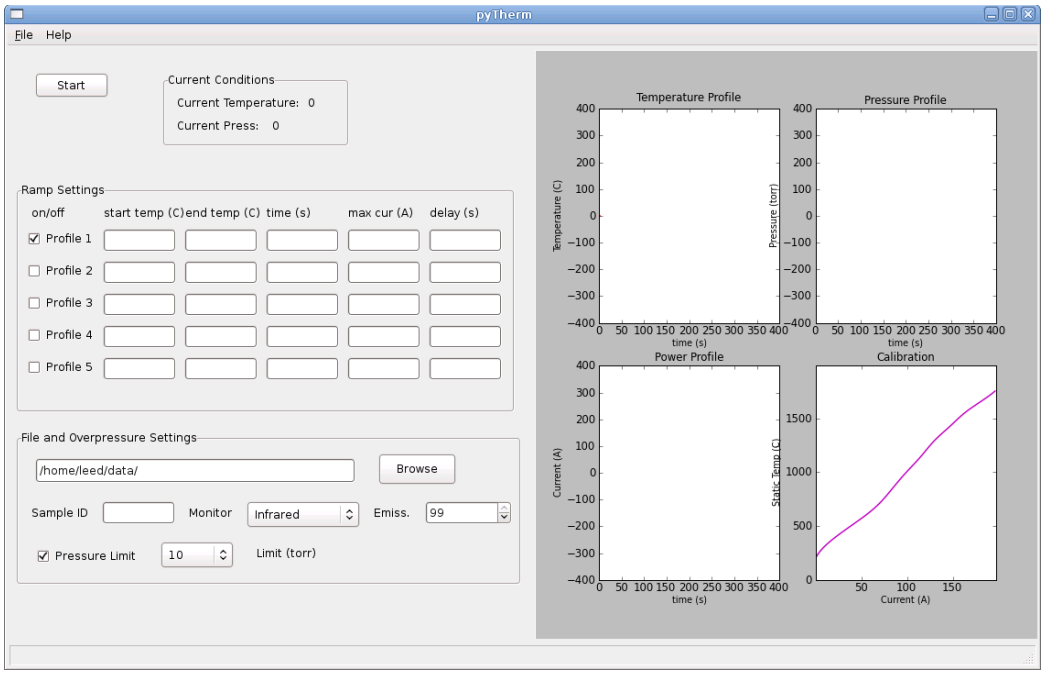


Figure 26: An image of the pyTherm interface. The temperature of the furnace can be monitored two different ways (type C thermocouple and infrared pyrometer). The pressure is recorded during heating, and the maximum pressure can be set on the interface (so that the ion pump does not shut off). The interface has several heating stages which can be set. The temperature is controlled through a custom hybrid algorithm of PID feedback and a calibration curve. Plots of the pressure, temperature and supply current are simultaneously displayed as a function of time.

calibrated supply current for the desired temperature once the soak temperature has been reached. The PID then switches to "normal" feedback for maintaining the soak temperature.

Users can set 5 individual heating profiles. The start temperature $T_{start}$ indicates the temperature at which the program should begin heating. If the start temperature is above the current temperature, pyTherm will wait until the furnace has cooled below the start temperature before heating is initiated. The end temperature $T_{end}$ (or soak temperature) is the final temperature to which the furnace is ramped. The ramp is calculated from $(T_{end} - T_{start})/time$, given that the supply current required to achieve this ramp does not exceed *max cur*. The delay time specifies how long the temperature should be held at $T_{end}$ before the program either continues to the next profile or shuts off.

# CHAPTER III

# METROLOGY OF SIC($000\bar{1}$) GRAPHENE USING STM

## *3.1 Moiré Patterns on SiC($000\bar{1}$) Graphene*

Effects of rotationally stacked graphene sheets are highly visible in scanning tunneling topographs. The moiré patterns seen in Fig. 6 are manifested as spatial modulations in the tunneling current. It is generally held that these peaks are not physical corrugations of the lattice as is the case with lattice mismatched graphite/graphene on metals [Enachescu 1999]. Modulations between mismatched graphene lattices are thought to be a result of periodicities in the density of states [Pong 2005b]. The strongest argument supporting this point of view is that these patterns have never been observed in AFM. It is not uncommon to find moiré patterns in graphene that are as large as 50 nm, clearly within the resolution of AFM. One might argue that van der Waals surfaces are soft and therefore AFM may destroy the pattern. Even still, less invasive AFM techniques such as non-contact dynamic force microscopy (DFM) techniques have achieved atomic resolution on graphite, but no moiré patterns have been reported [Kawai 2009].

Very early measurements reported the existence of moiré patterns on HOPG [Kuwabara 1990, Xhie 1993]. To prepare the surface for STM, one generally exfoliates (or cleaves) the HOPG crystal with tape (this technique was adapted for preparation of exfoliated graphene samples). Often, monolayers or thin films that decouple in the exfoliation process lie on the surface at rotated angles to the bulk stacking, producing moiré patterns (see [Pong 2005b] for a review of moiré patterns on graphite). More recently, it was found that the rotated layers of carbon face graphene also display moiré patterns

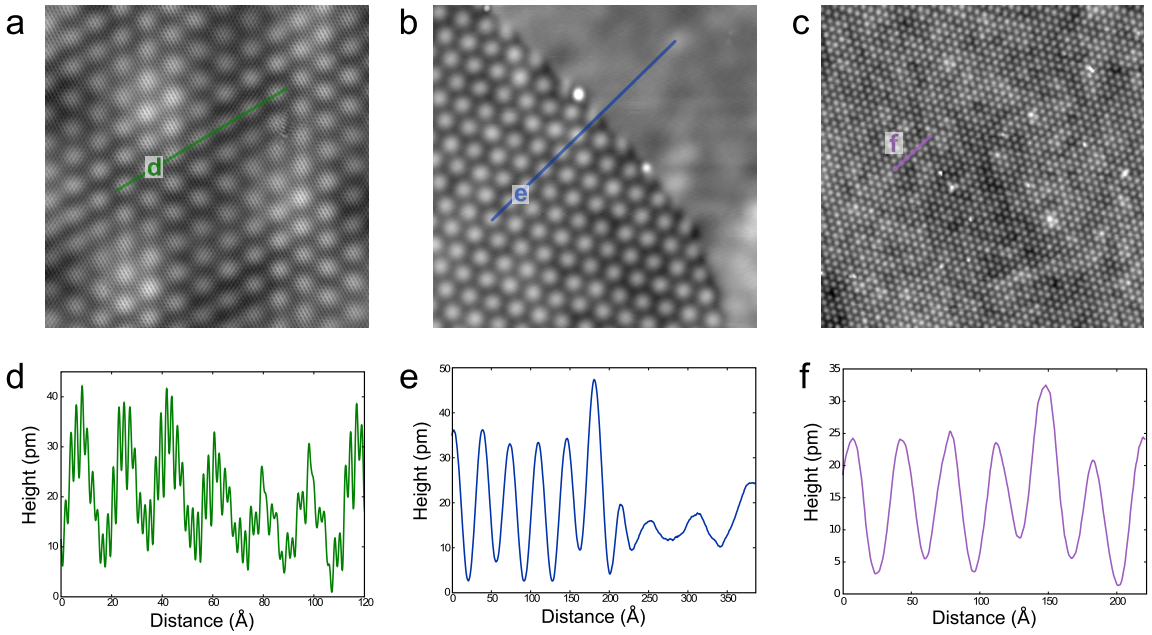


Figure 27: A few moiré patterns observed in STM on multilayer epitaxial graphene. (a) A 200 Å × 200 Å image with a "double moiré" and atomic corrugation visible at the fine scale ($V_S$ = 350 mV, $I_{set}$ = 100 pA, L_23543). (b) A 500 Å × 500 Å image, showing a low-angle grain boundary in a subsurface layer. The top layer is continuous (from atomic scale images), but a change of stacking in a subsurface layer causes the pattern to change ($V_S$ = 200 mV, $I_{set}$ = 100 pA, L_25987). (c) A 1500 Å × 1500 Å image showing the large, continuous spatial extent of the pattern ($V_S$ = 300 mV, $I_{set}$ = 100 pA, L_23470). (d-f) Height profiles from images in (a-c).

[Varchon 2008, Hass 2008c, Biedermann 2009]. Unlike graphite, however, multilayer epitaxial graphene is made up of mostly rotated layers, and often, more complex patterns arising from the cumulative effects of multiple rotated layers can be observed [Miller 2010a]. Various studies on HOPG have reported an attenuation factor (AF) corresponding to the decrease in moiré corrugation as a function of the number of carbon overlayers from the rotated stacking fault. A fit of this data yields $AF_n = e^{0.81n}$, where n is the number of overlayers [Rong 1994, Pong 2005a, Sun 2003]. In view of this, a second/third layer moiré pattern would be visible ($AF_1 = 2.25$) if present, but the possibility of observing patterns from deeper layers (such as fourth/fifth) seems very unlikely.

Figure 27 shows a few moiré patterns observed on the surface of MEG. The moiré shown in Fig. 27a has two periodicities. The larger supercell has a length of ~ 12 nm, while the shorter moiré (visible in the height profile shown in Fig. 27d) is ~ 2 nm. An

important point to note is that the amplitude of the moiré pattern on MEG is quite small compared to patterns on HOPG. The height profile in Fig. 27d shows a peak-to-peak superlattice height of $\Delta z \approx 0.25\,\text{Å}$. Corrugation from the atomic lattice is easily observed. The shortest periodicity in Fig. 27d is due to the atomic lattice, and represents a significant fraction of the moiré height. For patterns observed on HOPG, the peak-to-peak height is typically $\Delta z \geq 1\,\text{Å}$, and observed corrugations due to the moiré pattern as large as 20 Å have been observed [Pong 2005b]. The thickness of the MEG sample used in these measurements was $10 \pm 1$ layers, measured by ellipsometry (details of thickness measurements via ellipsometry are given in [Sprinkle 2010]). Similar height corrugations can be observed in other moiré patterns at other tunneling biases. Figures 27b-c show moiré patterns taken from other areas. The decreased corrugation seen in some regions (Figs. 27b,e) is possibly a result of greater decoupling between the layers. Occasionally, the moiré pattern changes or terminates abruptly (Fig. 27b), yet the top graphene lattice of MEG is continuous. Features like this are also observed in HOPG and commonly associated with subsurface grain boundaries.

### 3.1.1 Fourier Transform Analysis of Multiple Superperiods

The length of a superlattice cell can be evaluated as the wavelength of an interference pattern resulting from the misaligned reciprocal lattice vectors. The difference between a reciprocal lattice vector $\boldsymbol{k}_i$ and a reciprocal lattice vector rotated by angle $\theta$, $\boldsymbol{k}'_i = \hat{R}(\theta)\boldsymbol{k}_i$, is used to determine the length ($D$) and orientation ($\phi$) of the pattern. Here, we use the $\boldsymbol{k}'$ vector as the rotated reciprocal lattice vector from a second graphene layer. Since we are interested in long wavelength moiré patterns (rotation angles, $\theta \leq 5°$), the only relevant vectors of the interference pattern will be $\Delta\boldsymbol{k} = \boldsymbol{k}_i - \boldsymbol{k}'_j$ for $i = j$, where $i$ is any of six graphene reciprocal lattice vectors. For unstrained lattices, only one pair of vectors $\boldsymbol{k}$ and $\boldsymbol{k}'$ needs to be considered because of symmetry ($\Delta\boldsymbol{k}$ is simply rotated by 60 ° for the other vectors). Thus, for two rotated lattices of undistorted length, we obtain the equation for the

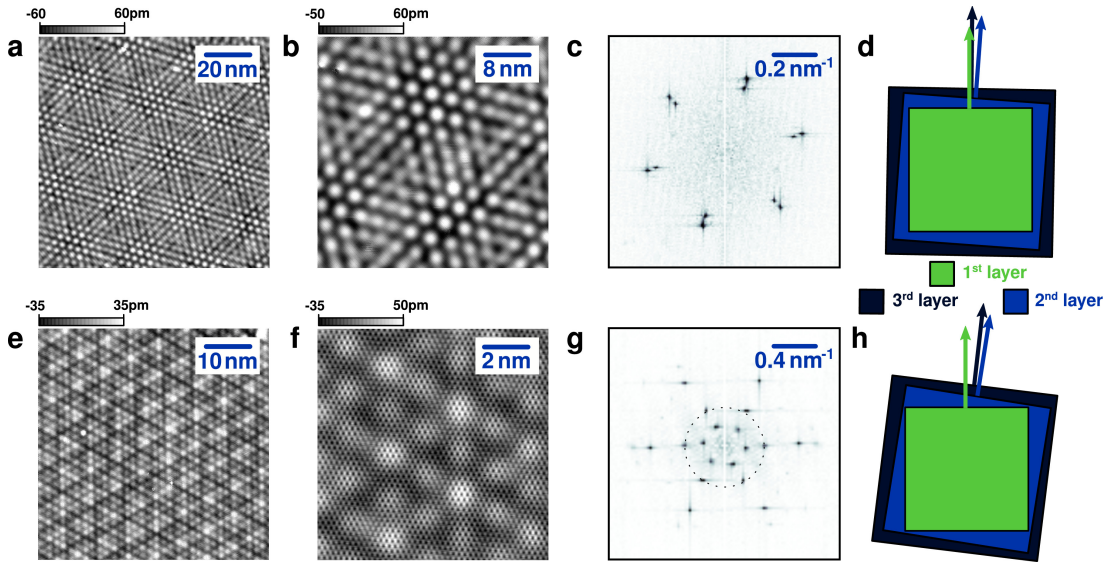


Figure 28: STM topographs of two moiré patterns on multilayer epitaxial graphene ($V_S$ = 0.5 V, $I_{set}$ = 100 pA). (a) Two similarly-sized moiré patterns interfering, resulting in a large superlattice unit cell. Layers 1 (surface layer) and 2, and layers 2 and 3 have comparable rotation angles in opposite directions (shown schematically in d). (b) High resolution image of a region in (a). (c) FT of (a). (d) Schematic of layer orientations based on the moiré pattern shown in (a, L_24336) and (b, L_24318). (e, L_25598) STM image of a different moiré superlattice. (f, L_25606) High resolution image from within the same area. (g) FT of (e). Spots on the dotted circle result from the interference of two moiré patterns (three graphene layers). The top-layer atomic reciprocal lattice from a FT of (f) determines which spots correspond to the moiré formed from layers 1 and 2 (see Eq. 48). (h) schematic of layer orientations based on the moiré pattern in (e).

size of the moiré unit cell length [Kuwabara 1990, Amidror 2003]

$$D = \frac{2\pi}{|\boldsymbol{k} - \boldsymbol{k}'|} = \frac{a}{2\sin(\theta/2)}, \tag{47}$$

and orientation with respect to the atomic lattice,

$$\phi = \frac{\pi}{6} - \theta/2. \tag{48}$$

Figure 28a shows an example of two interfering moiré patterns (the collective interference of three graphene layers), obtained by STM measurements. On first glance, one might think that the moiré pattern constitutes a significant modulation in the tip height. In fact, the graphene lattice is extremely smooth, such that any small changes in tip height become the foremost feature. Height modulations due to moiré patterns are at most 0.05 nm peak-to-peak. From Fig. 28a and Fig. 28b, two periodicities can be seen. The large periodicity

has a length of $D \approx 26.5\,\text{nm}$ while the smaller periodicity has a length of $D \approx 3\,\text{nm}$, still much larger than the atomic lattice spacing. Because more than a single moiré pattern is observed, we can conclude that this is a combined effect of at least three layers (in another area of the sample, 3 coexisting moiré patterns were found, implying the participation of at least 4 graphene layers). From the discrete fast Fourier transform (FT) in Fig. 28c, we find that two sets of spots are present in reciprocal space. These spots correspond to moiré lengths of $D_1 = 2.95 \pm 0.05\,\text{nm}$ and $D_2 = 3.35 \pm 0.09\,\text{nm}$.

Using equations 47 and 48 and $a = 0.246\,\text{nm}$ as the graphene lattice constant, we deduce the rotation angles needed to produce a moiré of size $D_1$ and $D_2$ as $\theta_1 = 4.78 \pm 0.07\,^\circ$ and $\theta_2 = 4.21 \pm 0.11\,^\circ$. Because $\Delta\phi = \phi_1 - \phi_2 \approx 0\,^\circ$, as seen in the Fourier transform, we propose the orientation of the top three layers in Fig. 28d. The first and third layers (starting from the surface and counting into the bulk) must be nearly aligned in order to obtain the observed $\Delta\phi$ in the FT. The measured value is $\Delta\phi = 0.61 \pm 0.23\,^\circ$, slightly higher than the expected value of $\Delta\phi = 0.29\,^\circ$ from the proposed three layer orientation (Fig. 28d) and equation 48. Again, we can determine the length of the largest interference pattern from $\Delta\boldsymbol{k}$ using the moiré reciprocal lattice vectors from the FT,

$$D_3 = \frac{D_1 D_2}{\sqrt{D_1^2 + D_2^2 - 2D_1 D_2 \cos(\Delta\phi)}}. \tag{49}$$

Thus, we calculate a value of $D_3 = 24.7 \pm 1.6\,\text{nm}$ for the size of the largest observed pattern. The uncertainty is due to a distortion in the hexagonal shape of the pattern, and is likely caused by strain, which will be discussed later. As shown in the schematic in Fig. 28d, the top layer is nearly aligned with the third. This creates two patterns of nearly equal size and orientation. The angle between the two moiré patterns is small, producing a large interference pattern.

In the case of Fig. 28e, we have applied a similar analysis to determine the orientation of the top three lattices. The smallest $\boldsymbol{k}$ vectors in Fig. 28f were determined to correspond

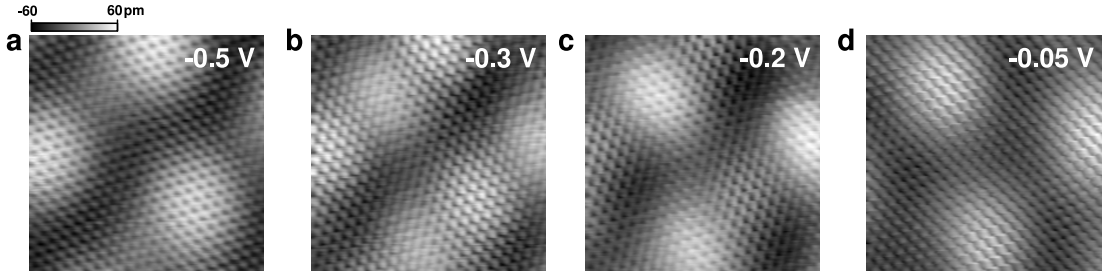


Figure 29: Multibias imaging on the moiré pattern in Figure 28a. Each image is 5 nm × 5 nm, and was taken at the same spatial location and tunnel current (100 pA). In (a, L_24048), only the moiré pattern of the top two layers is imaged. (b, L_24044), (c, L_24045) show the transition as the tip moves closer to the surface. In (d, L_24047), the tip has pushed in far enough to only image the lower layer moiré pattern. We believe that by $V_S = -0.05$ V, the tip is actually in contact with the surface.

to the moiré pattern of the first and second layers by comparing the moiré pattern orientation with respect to the reciprocal lattice vectors. We propose that there is a small rotation between the second and third layer. The interference of these two moiré patterns is responsible for the hexagonal set of spots on the dotted circle in the FT (Fig. 28g). Consequently, the image in Fig. 28e looks qualitatively very different than the one in Fig. 28a.

### 3.1.2 Multiple Bias Imaging

As further proof of concept, we image the pattern at multiple sample biases for a constant tunneling current. Because the imaging is done in a constant current mode, the tip will move closer to the surface as the sample bias ($V_S$) is decreased. This technique is used in imaging Bernal stacked graphene bilayers, and shows a transition in the imaging of the atomic lattice [Rutter 2008]. At higher biases, every atom is imaged; however, as the bias is decreased the tip instead images every other atom.

Figures 29(a-d) show the result of imaging at multiple biases on a region within the image shown in Fig. 28a. At $V_S = -0.5$ V, a single set of moiré maxima is seen, corresponding to a moiré pattern from the rotation of the first/second layer. As the bias decreases, the tip begins to image a second moiré pattern. By $V_S = -0.05$ V, the tip images only the second moiré pattern, which apparently results from rotation of layers 2 and 3. From measured

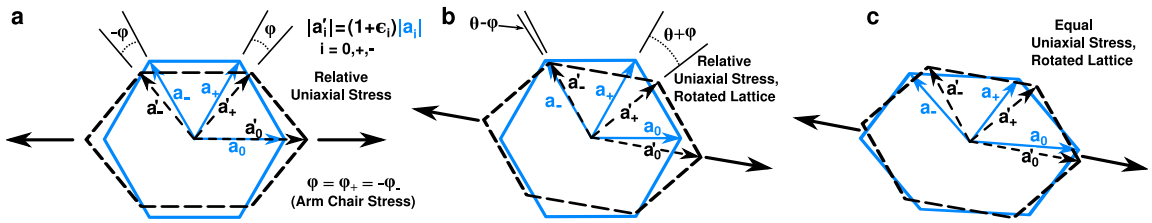


Figure 30: (Color online) Strain induced between two stacked hexagonal (real space) lattices in the case where one lattice (black/dashed line) is (a) stretched but not rotated and (b) stretched and rotated with respect to the undistorted lattice (blue/solid line). (c) displays equal strain for both lattices. For rotated lattices under relative strain, the angular change in the lattice vectors affect the interference pattern differently for each direction. As a result, the moiré pattern observed in STM will appear stretched or distorted. Significantly higher strain is required for similarly sized distortions if the lattices are equally strained along the same direction. At the low moiré angles ($\theta$), the lattice vectors (when equally strained) will obtain similarly sized angular distortions $\varphi_i$ which will nullify each other.

deviations in the expected exponential decay of tunneling current vs tip-height ($I$ vs $z$), we believe that by $V_S = -0.05\,\mathrm{V}$ the tip is in contact with the surface. The difference in tip height between $V_S = -0.5\,\mathrm{V}$ and $V_S = -0.05\,\mathrm{V}$ is $\Delta z = 0.39\,\mathrm{nm}$. The sample biases at $V_S = -0.3\,\mathrm{V}, -0.2\,\mathrm{V}$ (Fig. 29b,c) show the transition in imaging the top moiré to the one underneath. The tip bias, tunneling current and tip shape are known to have a large effect on the imaging of a moiré pattern [Pong 2005b]. Similar behavior was predicted for a rotated layer on top of AB stacked graphite [Cisternas 2008]. Calculations of STM imaging for layer configurations similar to those studied here would be a valuable aid in determining the relative influences of the density of states and the tunnel conditions.

## *3.2 Atomic moiré interferometry*

Relative strain induced between two stacked hexagonal lattices can have a large effect on observed superlattice wavelengths. This phenomenon is well known in moiré interferometry as a technique for strain measurement [Bromley 1956], and has been observed in large period moiré patterns on HOPG [Xhie 1993]. The effect appears as a distortion in the real space hexagonal shape of the superlattice cell, resulting from unequal distortion of both the relative length and angular alignment of the reciprocal lattice vectors. Distorted moiré

patterns are commonly observed in HOPG when lattice rotation angles ($\theta$) are small. We examine the effect of a uniform strain in the top layer relative to an unstrained layer below. For simplicity, we demonstrate the effect of a relative strain in the armchair direction on the observed superlattice periodicity.

Strain breaks the symmetry of the reciprocal lattice vectors, so we now consider the case where the lattice has been uniformly strained along the armchair direction, such that $|\boldsymbol{a}_i'| = (1+\epsilon_i)|\boldsymbol{a}_i|$, where $i = 0, \pm$. The vector $\boldsymbol{k}_0$ along the direction of strain does not change angular orientation ($\varphi_0 = 0$), so under rotation

$$\boldsymbol{k}_0' = \frac{1}{(1+\epsilon_0)}\hat{R}(\theta)\boldsymbol{k}_0. \tag{50}$$

This leads to a change in the wavelength of the interference pattern along the strain direction as given by the law of cosines,

$$D_0 = \frac{2\pi}{|\boldsymbol{k}_0 - \boldsymbol{k}_0'|} = \frac{a(1+\epsilon_0)}{2\sqrt{(1+\epsilon_0)\sin^2(\theta/2) + \epsilon_0^2/4}}, \tag{51}$$

Lattice vectors ($\boldsymbol{a}_\pm$) which are not along the direction of strain will undergo an additional rotation, $\varphi_\pm$. In the most general case of arbitrary changes in length ($\epsilon_i$) and arbitrary rotations ($\varphi_i$), this becomes:

$$D_i = \frac{2\pi}{|\boldsymbol{k}_i - \boldsymbol{k}_i'|} = \frac{a(1+\epsilon_i)}{2\sqrt{(1+\epsilon_i)\sin^2[(\theta+\varphi_i)/2] + \epsilon_i^2/4}}. \tag{52}$$

where $i = 0, \pm$, and the distortion in the angular orientation of the moiré is given by

$$\phi_i = \arcsin\left(\frac{(1+\epsilon_i)\sin(\theta+\varphi_i)}{2\sqrt{(1+\epsilon_i)\sin^2[(\theta+\varphi_i)/2] + \epsilon_i^2/4}}\right) \tag{53}$$

In order to approximate the values of $\epsilon_i$ for a uniform uniaxial stress, we make use of Poisson's ratio $\nu$ and the strain matrix $\boldsymbol{\varepsilon}$ by, $\epsilon_x = \varepsilon, \epsilon_y = -\nu\varepsilon$ [Kittel 1996]. The strain matrix is:

$$\boldsymbol{\varepsilon} = \begin{pmatrix} 1+\varepsilon & 0 \\ 0 & 1-\nu\varepsilon \end{pmatrix}, \tag{54}$$

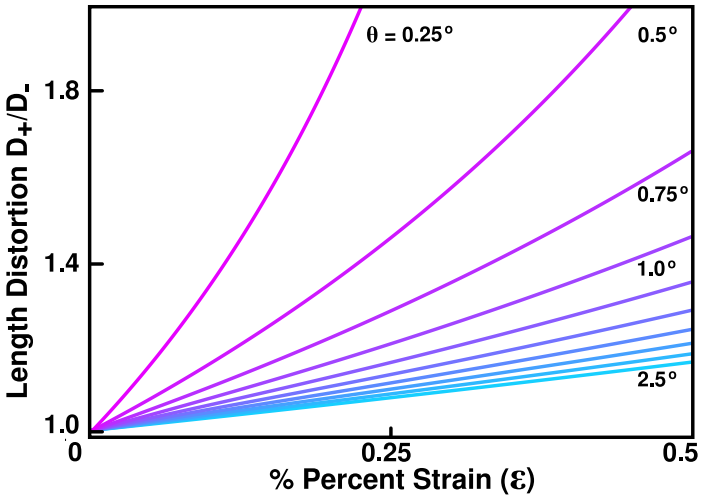


Figure 31: (Color online) Curves display the length distortion between two vectors of the moiré cell as a function of the moiré rotation angle $\theta$. The amount of distortion for a small strain rapidly increases with decreasing moiré rotation angles (i.e. when the rotation angle is comparable to the angular distortion, $\theta \sim \varphi$).

where the axes have been chosen to diagonalize the strain matrix. Poisson's ratio is defined as:

$$\nu = -\frac{\Delta w/w}{\Delta L/L} \tag{55}$$

where $w$ is the width of the graphene sheet and L is the length ($\Delta w$ and $\Delta L$ are the changes under deformation).

For strain in the armchair direction, we do not need to rotate the lattice vectors $\boldsymbol{a}_i$ with respect to $\boldsymbol{\varepsilon}$. In this case the lattice is stressed along $\boldsymbol{a}_0$. We can relate the strain matrix to the values $\epsilon_i$ by applying the original definition,

$$|\boldsymbol{a}_i'| = (1 + \epsilon_i)|\boldsymbol{a}_i| = |\boldsymbol{\varepsilon}\boldsymbol{a}_i|. \tag{56}$$

Thus, under a small strain approximation ($\varepsilon \ll 1$) we obtain

$$\epsilon_0 = \varepsilon, \epsilon_\pm \approx \frac{1}{4}(1 - 3\nu)\varepsilon. \tag{57}$$

$$\varphi_0 = 0, \varphi_\pm \approx \pm\sqrt{3}\varepsilon\left|\frac{1+\nu}{4 + \varepsilon(1-3\nu)}\right| \tag{58}$$

We use the values from equations 56 and 57 and approximate Poisson's ratio as $\nu = 0.5$ [Reddy 2006] to plot the overall distortion in the wavelength of the interference pattern. If

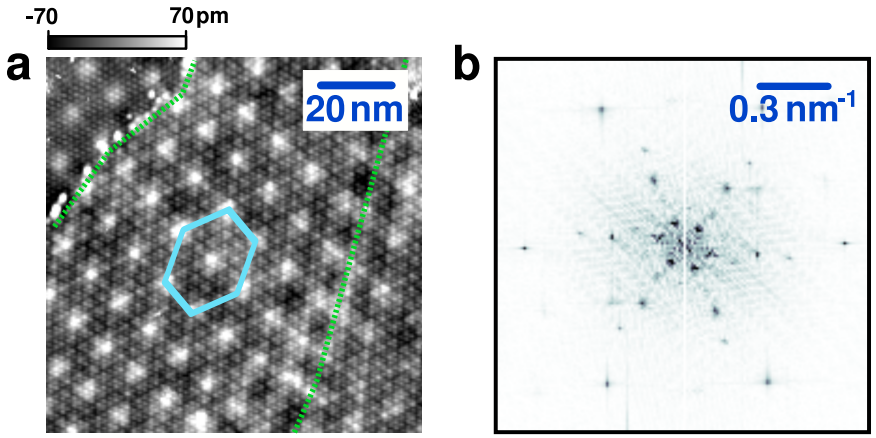


Figure 32: (Color online) (a, L_25800) STM image demonstrating the effect of strain on the moiré superlattice ($V_S = 0.35$ V, $I = 100$ pA). (b) FT of the image in (a). Five sets of moiré spots can be identified, requiring interactions from at least 4 layers. Strain may be caused by subsurface low-angle grain boundaries [marked approximately with green lines in (a)] or by nearby "pleats."

we put these values into 52, we can compare the length distortion ($D_+/D_-$) of the resulting moiré pattern. Figure 31 clearly shows the expected behavior. As the rotation angle $\theta$ between the lattices increases, the effect of the distortion is quickly diminished; however, for a large moiré pattern the rotation angle is small, leaving the pattern easily distorted by the relative strain. The reason is that small angular differences become comparable to the rotation angle ($\varphi \approx \theta$), and lattice distortions cannot be neglected. Additionally, in this regime small changes in the lattice constant $a$ contribute greatly to the moiré rotation angle. The shape of the moiré hexagon suffers additional skewing in $\phi_i$ due to the angular distortion of the reciprocal lattice vectors.

Obtaining an exact measure of the strain is difficult because it can be hard to determine the direction of the applied stress. Distortions can also be made from equally stretching both lattices along one direction as in Fig. 30c; however the distortions of the resulting moiré patterns are generally much smaller than for relative strains (on the order of several percent strain for a comparable length distortion). The reason is that for small moiré rotation angles, the lattice vectors will obtain similarly sized angular distortions for each lattice vector pair, $i$, thereby yielding a relative angular distortion of $\varphi_i - \varphi_i' \approx 0$. In this case, we can use the original moiré equations to approximate the length distortion simply

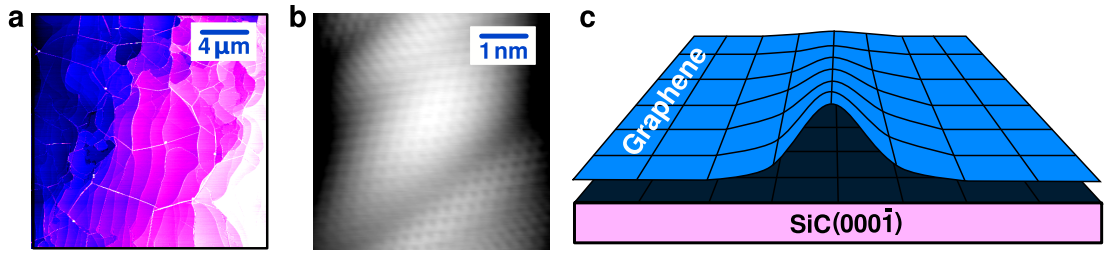


Figure 33: (Color online) (a) Large-area AFM image showing pleats; i.e., folds in the stacked graphene layers. Pleats tend to run along the SiC step or perpendicular to them. (b, L_25218) Atomically-resolved STM image on the top of a pleat. Tunneling conditions were $V_S = 350\,\text{mV}$, $I_{set} = 100\,\text{pA}$. (c) Schematic of a pleat in epitaxial graphene. Mismatches in the thermal contraction after growth can induce buckling of the graphene lattice causing pleats to form.

by replacing the lattice spacing $a$ in equation 47 with its distorted values, $a_i = (1 + \epsilon_i)a$.

Given a low enough angle rotation, the relative strain effects are indeed observed. Low angle moiré patterns are even more likely to occur when multiple patterns can be simultaneously observed. Figure 32a shows a fairly large moiré pattern with an average unit cell length of $D = 10.5\,\text{nm} \pm 0.9\,\text{nm}$, corresponding to a rotation angle $\theta = 1.36 \pm 0.11^\circ$ (calculated using the FT in Fig. 32b); however, distortion from relative strain causes the actual size of the moiré pattern to range from 9.50 nm to 11.7 nm, depending on which axis is measured. This corresponds to a moiré length distortion of 23% ($D_{max}/D_{min} = 11.7/9.50 = 1.23$); thus we estimate the parameter $\varepsilon \approx 0.37\%$ for the relative strain between the two lattices producing the pattern.

There are a few mechanisms by which a graphene sheet can undergo strain. In Fig. 32a, low angle grain boundaries are visible. The moiré pattern bends with the boundary on the right. In this case, the subsurface rippling of the lattice is likely causing a slight relative strain. Another type of strain possible in graphene grown on SiC(000$\bar{1}$) is a bending of the graphene sheet caused by unequal thermal contractions between the SiC and graphene sheets after growth [Cambaz 2008]. In order to relieve stress, the lattice buckles (see Fig. 33a,b). The image in Fig. 33a was taken by atomic force microscopy, and shows these "pleats" of the graphene sheet. They are typically 5 nm to 10 nm in height, and are visible in Fig. 33a as white lines running parallel and transverse to the SiC steps. Despite

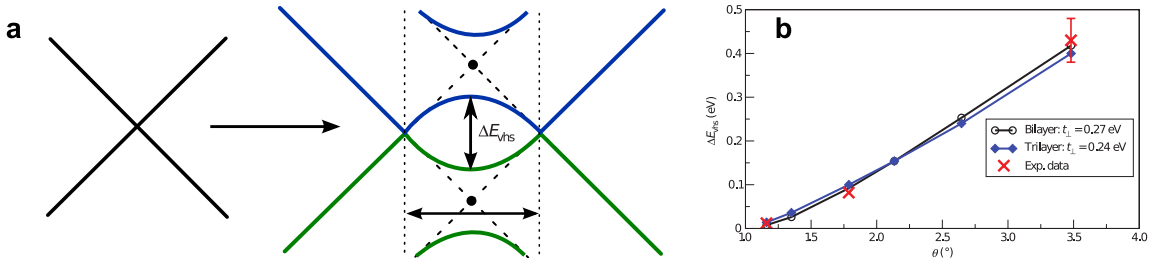


Figure 34: (a) Band structure of two twisted bilayers. For two (decoupled) AA stacked sheets, the Dirac cones line up on top of one another. As the layers are twisted toward 30 °, the bands spread apart in k-space. If there is interaction between layers, the crossing points cause band repulsion which modifies the band structure. (b) A fit to the model of the energy separation between the Van Hove singularities (Reprinted from [Li 2009a]).

bending, the graphene lattice stays intact over a pleat, and the graphene lattice can extend for several microns before a pleat occurs. The STM image in Fig. 33b was taken on top of a graphene pleat. The lattice is continuous, but it is clearly contorted as a result of the lattice buckling. The strain relief looks much like the strain relief in nanotubes [Orlikowski 2000]. Flat areas near these pleats could show strain effects. Immediately around pleats, slight layer delamination is possible which may not even produce a recognizable moiré pattern to be observed.

## *3.3 STS of SiC($000\bar{1}$) Graphene without a magnetic field*

Theory suggests that moiré patterns from rotated layers of graphene should cause extra features in the density of states. The rotation of two graphene sheets causes the bands to shift with respect to each other in k-space. This produces a point of crossing between the linear bands from each layer. If the layers interact, the band repulsion creates a band gap around those points (Fig. 34a). If this occured in MEG, it would produce peaks in the density of states called Van Hove singularities [Van Hove 1953]. Band structure calculations of twisted bilayers have indicated that they should be present [Lopes dos Santos 2007]. These peaks were observed using scanning tunneling spectroscopy on HOPG and graphene grown by chemical vapor deposition [Li 2009a], and the model for the energy separation ($\Delta E_{VHS}$) between the peaks on the density of states was fit (Fig. 34b). A smaller moiré pattern

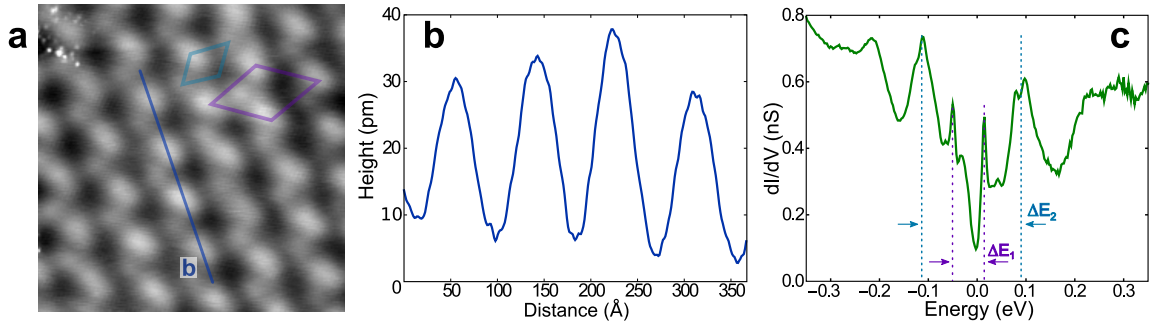


Figure 35: (a) A double moiré pattern on MEG. Supercells are marked in blue (~ 4.8 nm) and purple (~ 8.3 nm) in the 400 Å × 400 Å image (L_23915). The blue line shows a (b) height profile with modulations due to the superperiodicity. (c) A $dI/dV$ spectrum taken from the center of the image in (a), showing Van Hove—like peaks in the density of states. The energy gap between the peaks as marked are $\Delta E_1 = 64$ meV and $\Delta E_2 = 202$ meV. Tunneling conditions were $V_S = 0.5$ V, $I_{set} = 100$ pA.

produces a larger $\Delta E_{VHS}$ because of a larger $\Delta k$ in the reciprocal lattice vectors.

Figure 35a shows the moiré pattern where this spectra were recorded. The moiré pattern produces a modulation in the topography of ~20 pm. The $dI/dV$ spectrum in Fig. 35c shows similar features to other observed Van Hove spectra. The size of the supercell is quite large (marked in purple in Fig. 35a). The oscillations in the height profile indicate a periodicity of ~ 8.3 nm, corresponding to a rotation angle of $\theta \approx 1.7\,^\circ$. It also appears that there is a second periodicity as well (light blue, Fig. 35a). This periodicity is difficult to pick out from the larger pattern, but the supercell as marked would have a length of ~ 4.8 nm corresponding to a rotation angle $\theta \approx 2.95\,^\circ$.

It seems that the two moiré periods could be producing two sets of Van Hove singularities. These are marked as $\Delta E_1$ and $\Delta E_2$ in Fig. 35c. The smaller of the two, $\Delta E_1$ matches the expected value for the larger superperiod from the fit in [Li 2009a] (Fig. 34c), but $\Delta E_2$ is significantly off for the smaller periodicity.

We cannot make a statement about the existence of Van Hove singularities in MEG with certainty. Our measurements were generally focused on low energy features, and often the size of the moiré supercell was small enough that $\Delta E_{VHS}$ was not in the energy range of our spectra. Additionally, most of our moiré patterns displayed multiple layers

of interaction for which the two-layer theory may not apply. The spectra in Fig. 35c may indicate Van Hove singularities, but further investigation is necessary (eg. determination of $\Delta E_{VHS}$ vs. moiré rotation angle). STS spectra with features reflecting Van Hove peaks were not commonly observed. The increased layer decoupling of MEG may be enough to completely remove the interlayer coherence. It should be pointed out that modulations of the tip height of moiré patterns on MEG are substantially less than on HOPG. This may be indicative of the interlayer decoherence, but the fact that a moiré pattern is observed at all seems to suggest that there must at least be *some* effect on the electronic structure.

# CHAPTER IV

# SCANNING TUNNELING SPECTROSCOPY OF GRAPHENE IN A MAGNETIC FIELD

## *4.1 Sample Treatment and Experimental Details*

In the following set of measurements, we explore the electronic properties of multilayer epitaxial graphene [MEG, graphene grown on 4H-SiC(000$\bar{1}$) ] in a magnetic field. The sample was grown at Georgia Tech using a low-vacuum induction furnace technique. Prior to growth, the sample was hydrogen etched in order to form a uniform step structure. The sample thickness was measured using ellipsometry [Sprinkle 2010] and found to be 10 ± 1 monolayers thick. It was then characterized using LEED and Auger, and the surface was prepared in the RTSTM at Georgia Tech.

Following these preliminary measurements, it was exposed to air during transport to NIST. At NIST, the sample was re-heated in UHV to 1250 $^{\circ}C$ as a cleaning procedure. After cooling, it was transferred in vacuum into the LTSTM for magnetic field measurements.

For STS measurements, we used electrochemically etched iridium tips. The tips were characterized and further prepared in vacuum via field evaporation in a field-ion microscope. A lock-in amplifier was used to acquire $dI/dV$ measurements. The superimposed AC voltage was set at a frequency of $f_{mod} = 500\,\text{Hz}$, and the root-mean-square of the amplitude was set at $V_{mod} = 1 - 2\,\text{meV}$ for all measurements.

## *4.2 Point Spectroscopy at Fixed Magnetic Fields*

According to equation 23, application of a perpendicular magnetic field to the plane of a graphene sheet should produce quantized energy states stemming from the boundary conditions for electrons in cyclotron motion. The zero-field "V-shaped" density of states

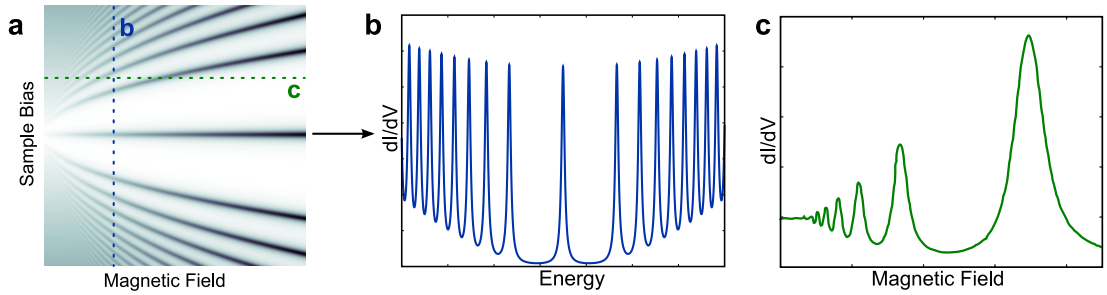


Figure 36: (a) A simulation of the LL structure in graphene (dark color represents high density of states). The dotted line shows the location of density of states profiles taken along the (b) energy direction and (c) magnetic field direction. Peaks seen in (c) are a result of the LL passing through the sample bias $V_S$, resulting in an increase in the density of states.

collapses into a series of peaks. Because the sample density of states $\rho_S$ can be measured using STS, this provides a direct route to observing the LL structure in 2D materials like graphene. The application of a magnetic field provides a 2D space of energy and magnetic field, which can be probed by various methods using STM (see Fig. 36).

Figure 37a shows a $dI/dV$ measurement of graphene in a perpendicular magnetic field of $B = 5\,\mathrm{T}$. The LLs are well-defined, narrow peaks in the density of states, sharper in energy width than those previously measured by STS in other 2-D systems [Morgenstern 2003b, Matsui 2005, Li 2007]. Over 20 LL peaks can be identified. The peaks are not equally spaced as in a conventional 2DES (equation 16). As expected for graphene (equation 23), the LLs have a $\sqrt{N}$ dependence with a central $\mathrm{LL}_0$ at the neutrality point. Each LL is four-fold degenerate: two-fold for each of the spin and valley degeneracies.

The Gaussian energy broadening from thermal effects and the RMS lock-in modulation amplitude ($V_{mod} = 1\,\mathrm{meV}$) is $\sigma_G = 2.8\,\mathrm{meV}$. The LLs in Fig. 37a are fit with a series of Voigt functions, which is a convolution of Gaussian and Lorentzian linewidths:

$$V_N(E) = \int_{-\infty}^{\infty} d\epsilon' G(\epsilon'; \sigma_G) L_N(E - \epsilon'; \sigma_L) \tag{59}$$

where,

$$G(\epsilon; \sigma_G) = \frac{1}{\sqrt{2\pi}\sigma_G} e^{-\epsilon^2/(2\sigma_G^2)} \tag{60}$$

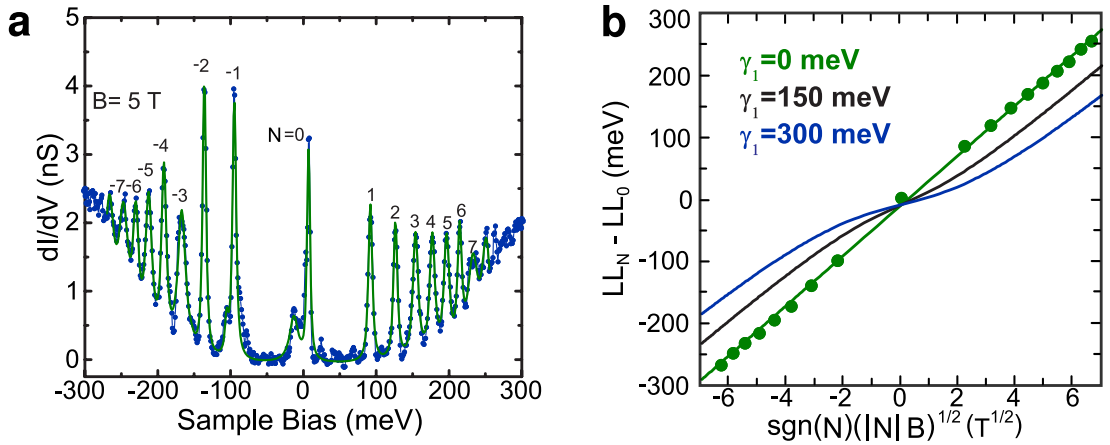


Figure 37: (a) dI/dV scan of MEG in a strong magnetic field ($B = 5$ T). (b) The LL structure linearizes with $sgn(N)\sqrt{|N|B}$ as expected. When interlayer coupling is included ($\gamma_1$, black and blue lines), the data is not well fit, implying that the top layer has completely decoupled.

$$L_N(\epsilon;\sigma_L) = \frac{\sigma_L}{\pi\left[(\epsilon - E_N)^2 + \sigma_L^2\right]}. \tag{61}$$

Equation 59 is for area normalized Voigt functions, so we multiply by an amplitude constant for fitting, $A_N$. $E_N$ (energy of the peak) and $\sigma_L^N$ (Lorentzian width) and $A_N$ are the only fitting parameters that we use, while holding $\sigma_G$ constant at 2.8 meV (the experimental broadening). The full spectrum is well described by:

$$\rho_S(E) = \sum_{N=-\infty}^{\infty} A_N V_N(E; E_N, \sigma_L^N) \tag{62}$$

We truncate the sum at $N = -9, ..., +9$ for computation. We also include two additional terms to account for the small anomalous peaks around $N = 0$ and $N = -1$. The fit line (green line, Fig. 37a) accounts for virtually all of the spectral weight. The rising background is well described by the overlapping Lorentzian tails of the Voigt functions.

Using these parameters, we find that the width of $LL_0$ is $\sigma_L^{N=0} = 1.5$ meV. This is a significant, because the LLs are measured at a point; thus, they have not been broadened by inhomogeneities. The width, $\sigma_L^{N=0}$ can therefore be used as a measure of the minimum scattering time, $\tau = \hbar/\sigma_L$ (from the Heisenberg uncertainty principle), resulting in a value of $\tau = 0.4$ ps. This long scattering time is comparable to scattering times in the highest mobility suspended graphene samples [Bolotin 2008] or high quality MEG samples

[Orlita 2008]. These studies reported mobilities in excess of $200,000\,\mathrm{cm}^2/\mathrm{Vs}$.

Previous STS measurements of graphite found equally spaced LLs [Matsui 2005] or a mixture of $\sqrt{NB}$ and linearly spaced LLs [Li 2007]. Though this is a 10 layer sample, we find no evidence of linearly spaced LLs. For comparison, we also fit the data to the bilayer graphene LL structure (Fig. 37b) [Henriksen 2008]:

$$E_N = \frac{sgn(N)}{\sqrt{2}}\left[(2|N|+1)\Delta^2 + \gamma_1^2 - \sqrt{\gamma_1^4 + 2(2|N|+1)\Delta^2\gamma_1^2 + \Delta^4}\right]^{1/2} \tag{63}$$

where,

$$\Delta = c^* \sqrt{2eB\hbar}. \tag{64}$$

The best fit yields a value of $\gamma_1 = 0$, where $\gamma_1$ is known as the *interlayer coupling* parameter. When $\gamma_1 = 0$, equation 63 reduces to the monolayer form. Other values of $\gamma_1$ are plotted in Fig. 37 ($\gamma_1 = 350\,\mathrm{meV}$ was measured for bilayer graphene in [Henriksen 2008]). Clearly, increasing $\gamma_1$ beyond zero does not produce a better fit, suggesting a true monolayer electronic structure.

Figure 38a shows point spectra measured at the same spatial position (within a few angstroms) for several magnetic fields. The curves are offset vertically at equal 1 T intervals of the magnetic field. Lines are drawn faintly in the background with $\sqrt{|N|B}$ dependence as guides for the eye. As the magnetic field is increased, so are the LL peak intensities. With higher magnetic field, the LLs increase in degeneracy allowing each LL to hold more electron density. Interestingly, when $LL_0$ coincides with $E_F$, the level splits (particularly visible at the 6 T $dI/dV$ measurement). This could be the development of a correlated electron state, though further measurements would be required to qualify such a result.

When all of the peaks over the 1-8 T magnetic field range are fit with Voigt functions and the energy positions for each LL are determined, the plot of their energy versus $\sqrt{|N|B}$ is extremely linear (Fig. 38b). The slope of the fit line allows us to extract the carrier velocity, $c^* = 1.128 \pm 0.004 \times 10^6\,\mathrm{m/s}$ (error bounds represent one standard deviation in the carrier velocity, does not include systematic effects caused by the tip). If we fit the

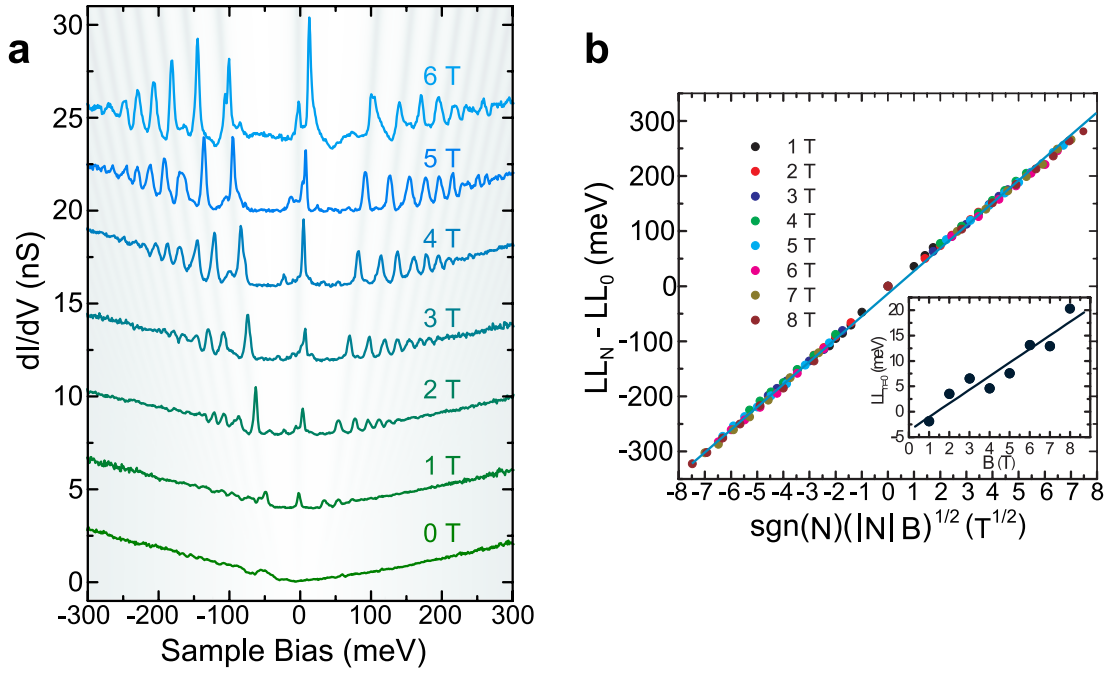


Figure 38: (a) $dI/dV$ measurements at 1 T intervals. The curves are offset vertically so that they can be easily seen. (b) A linearization of the data from (a). The slope of the light blue fit line gives the the carrier velocity as $c^* = 1.128 \pm 0.004 \times 10^6$ m/s. The inset shows the energy variation of $LL_0$ as a function of magnetic field.

electron and hole branches separately, we obtain slightly different velocities for each. For negative LLs, the measured velocity is $c^* = 1.189 \pm 0.007 \times 10^6$ m/s while the velocity for the positive LLs is $c^* = 1.044 \pm 0.004 \times 10^6$ m/s, demonstrating a 6% difference in the measured electron and hole velocities. This could imply the existence of many-body effects [Deacon 2007, Trevisanutto 2008], though it is more likely a result of band bending from the electric field of the tip.

The inset of Fig. 38b shows the change in energy of $LL_0$ as a function of the magnetic field. It appears that $LL_0$ changes linearly as a function of the magnetic field, starting slightly below $E_F$ at $B = 1\,\mathrm{T}$ ($E_0 = -1.8\,\mathrm{meV}$) and increasing above $E_F$ at $6\,\mathrm{T}$ ($E_0 = 13.1\,\mathrm{meV}$). When this is extrapolated to $B = 0$, the intercept is at $-3.8\,\mathrm{meV}$, corresponding to an electron density of $n = E_F^2/\pi\hbar^2 v_F^2 = 8.8 \times 10^8\,\mathrm{cm}^{-2}$ [de Heer 2007, First 2010]. The charge density is extremely low in the top layer due to screening of the charged interface by the stack of graphene sheets, consistent with the densities measured optically

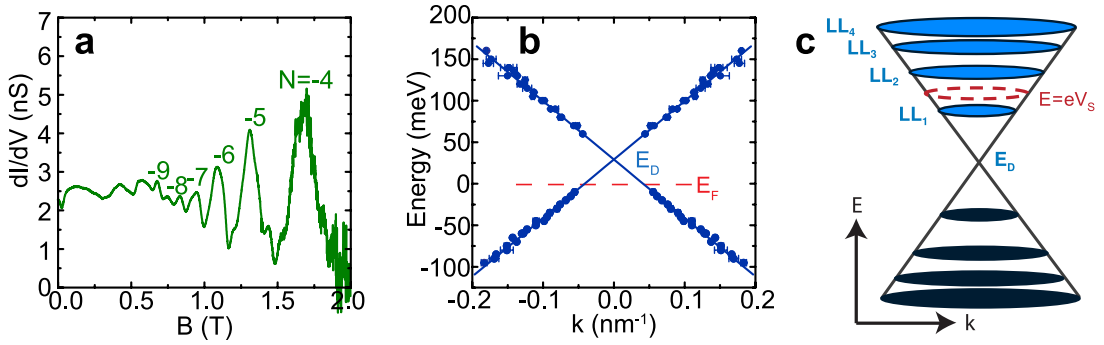


Figure 39: (a) A $dI/dV$ measurement at a fixed sample bias $V_S = -65$ meV. The magnetoconductance oscillates due to the passing of LLs through the tunneling bias. (b) A reconstruction of the low-energy band structure using TMCO measurements. If a circular cross-section is assumed, spectroscopy measurements can reproduce the energy band structure. Data is symmetrized about the $k = 0$ line. (c) A schematic of the conical graphene band structure in a magnetic field. The application of a perpendicular magnetic field forms discs (circles) due to LL formation. The red dotted circle represents the energy of the tunneling bias. As the magnetic field is increased, the LLs move through the circle, creating peaks in TMCO measurements.

[Sadowski 2006]. The interface between the SiC and the first graphene sheet on SiC(000$\bar{1}$) dopes the first layer to a charge density of $\sim 10^{13}$ /cm$^2$. The charge screening length is on the order of $\sim$ 1 layer, leaving the top sheet relatively undoped [Sun 2010]. The energy shift of $LL_0$ is not yet well understood, but it is likely to be related to the screening of the electric field from the STM tip. In a magnetic field, this is a complicated effect.

## *4.3 Point Spectroscopy at Fixed Sample Bias*

Another method of measuring the LLs in STM consists of holding $V_S$ fixed, while the magnetic field is ramped (Fig. 39a). This method had not previously been published prior to our work [Miller 2009]; however, these measurements (called tunneling magnetoconductance oscillations or TMCOs) have some similarities to Shubnikov de Haas (SdH) oscillations. Shubnikov de Hass measurements record the transverse resistivity in a Hall bar geometry. Maxima occur in the transverse resistivity whenever LLs cross $E_F$. Much like SdHOs, TMCOs find peaks when a LL crosses the sample bias, $V_S$ (i.e. when LLs cross the red line in Fig. 39c). The density of states at $V_S$ increases when a LL is at the sample bias, and consequently an increase in the magnetoconductance is measured (Fig. 36a).

A typical TMCO measurement on MEG is shown in Fig. 39a. By assuming circular cross-sections of the low-energy band structure, one can use TMCOs to find the slope of the energy bands (Fig. 39b). This assumption is valid at energies that are close to $E_F$, where trigonal warping is minimal. Distortions due to multilayer stacking are not considered, but the linear collapse in Fig. 39b of the data gives sufficient evidence that this is an excellent approximation to the band structure. The measured carrier velocity from the fit to the linear bands is $c^* = (1.07 \pm 0.006) \times 10^6$ m/s. This velocity is lower than the one measured using standard STS techniques; however, we consider it to be more accurate because it is performed at magnetic fields below 2 T, where the effect of band bending from the tip is likely to be less important.

Data is not taken in these measurements near $V_S = 0$ because the tip is being servoed in closed loop so that the magnetic field can be slowly ramped. Setting the tip at low bias would cause the tip to crash. Induced currents in the STM apparatus causes shaking at higher fields (which is the reason for the increasing noise as $B \rightarrow 2$ T in Fig. 39b). Even with these limitations, the band structure is mapped to lower energies than what is typically possible in photo-electron measurements [Rollings 2006, Bostwick 2007, Sprinkle 2009], and both filled and empty states are probed. TMCO measurements are covered at length in [Kubista 2011].

## *4.4 Absence of Velocity Renormalization*

A few theory papers have suggested a velocity renormalization (and van Hove singularities) resulting from twisted bilayer moiré patterns [Lopes dos Santos 2007, Mele 2010, Trambly de Laissardiere 2010]. Very recent measurements on CVD grown graphene samples appear to confirm these theories [Luican 2010]; however, these features have not been reproduced in photoemission [Sprinkle 2009] or infrared magnetospectroscopy experiments [Sadowski 2007].

In Fig. 40a, we show a 3.9 nm moiré pattern with STS spectra (Figs. 40b,c) taken at a

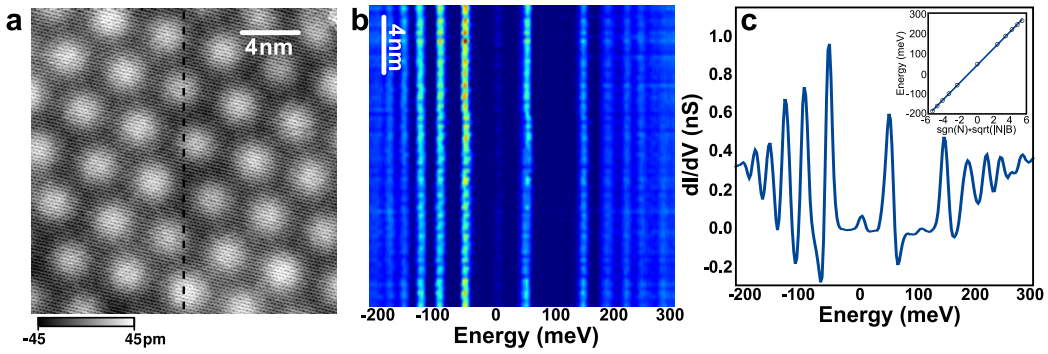


Figure 40: (a) A 3.8 nm moiré pattern (L_23626). (b) A line scan through the center of the image, showing the largely $\sqrt{|N|B}$ dependence of the spectra. Spectra are unaffected by the position of the tip relative to the moiré pattern. (c) Averaged spectra from (b). The inset shows the linearization of the LL peaks when plotted vs. $\sqrt{|N|B}$. The slope yields a value of $1.13 \pm 0.07 \times 10^6$ m/s. Spectra shows interesting negative differential conductivity at the edge of the LLs. This feature is occasionally observed when the tip is very sharp. Tunneling conditions for (a,c) were $I_{set} = 100$ pA, $V_S = 300$ mV.

magnetic field of 6 T. Figure 40b shows a line scan through the center of the topographic image. The LLs appear to be unaffected by the moiré pattern. For a 3.9 nm moiré pattern, the relative rotation between the layers is 3.61 °. This value is very close to the size of the pattern observed in [Luican 2010], where a renormalization of the velocity ($c^* = 0.87 \times 10^6$ m/s) and van Hove singularities at ±200 meV were observed. A fit to the data in Fig. 40c (see inset) yields a carrier velocity of $c^* = 1.13 \pm 0.07 \times 10^6$ m/s. Additionally, spectroscopic measurements on MEG at milliKelvin temperatures have observed a carrier velocity of $c^* = 1.08 \pm 0.03 \times 10^6$ m/s for a moiré pattern with a rotation angle of 2.3 ° [Song 2010]. Evidently, the velocity renormalization observed in CVD grown graphene multilayers is not reproducible on epitaxial graphene.

## *4.5 Density of States Mapping*

In this section, we extend the point spectroscopy measurements from Section 4.2 over two spatial dimensions. This results in a series of maps at discrete energies (Section 2.1.5.3). The measurement gives a unique view of graphene wavefunctions and reveals an unexpected lifting of the $LL_0$ valley degeneracy.

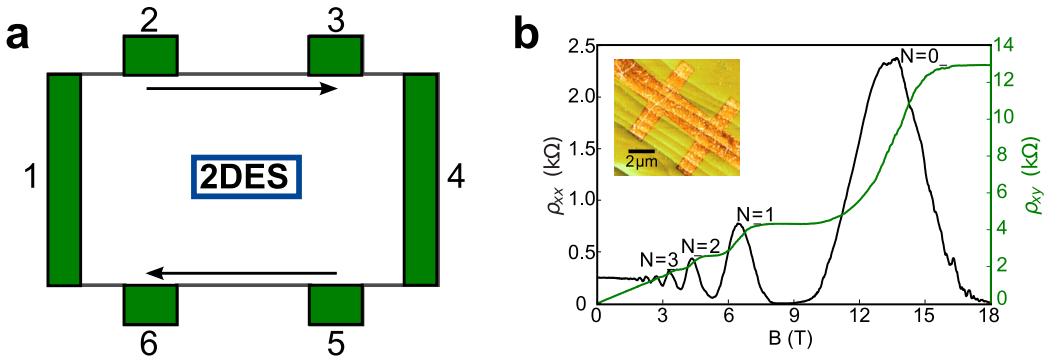


Figure 41: (a) A schematic of a six terminal quantum Hall device. Terminals 1 and 4 provide the current that travels along the edges when $E_F$ is between LLs (marked by arrows). The direction of the current is determined by the magnetic field. As shown, the magnetic field would be directed into the page. The longitudinal resistivity $\rho_{xx}$ is measured between 2 and 3 or 5 and 6, while the Hall conductivity is measured between 2 and 6 or 3 and 5. (b) Quantum Hall measurement on carbon face epitaxial graphene (reprinted from [Wu 2009]).

### 4.5.1 The Half-Integer Quantum Hall Effect

The quantum Hall effect is an important manifestation of the Landau level structure in a transport experiment. In a six terminal quantum Hall device (such as the one shown in Fig. 41a), the contacts 1 and 4 are used for driving current through the 2DES. The chirality of the magnetic field directs which way the current flows along the edges. The arrows in Fig. 41a mark the direction of the current flow, therefore the magnetic field is directed into the screen (let's be modern) by the right hand rule. The remaining contacts (2,3,5,6) are used for measurements. Resistances measured between 2 and 3 or 5 and 6 are referred to as the longitudinal resistance $R_{xx}$ (or $R_L$), while resistances measured between 2 and 6 or 3 and 5 are called the Hall resistance, $R_{xy}$ (or $R_H$).

Figure 41b shows a quantum Hall measurement on graphene grown on the carbon face of the polar SiC crystal. The inset shows an image of the six terminal Hall bar taken by atomic force microscopy (AFM). As the magnetic field increases, the Hall resistivity $\rho_{xy}$ forms distinct plateaus, while the longitudinal resistivity $\rho_{xx}$ oscillates and even drops to zero at higher fields.

Inhomogeneities in the electrostatic potential play an important role in understanding

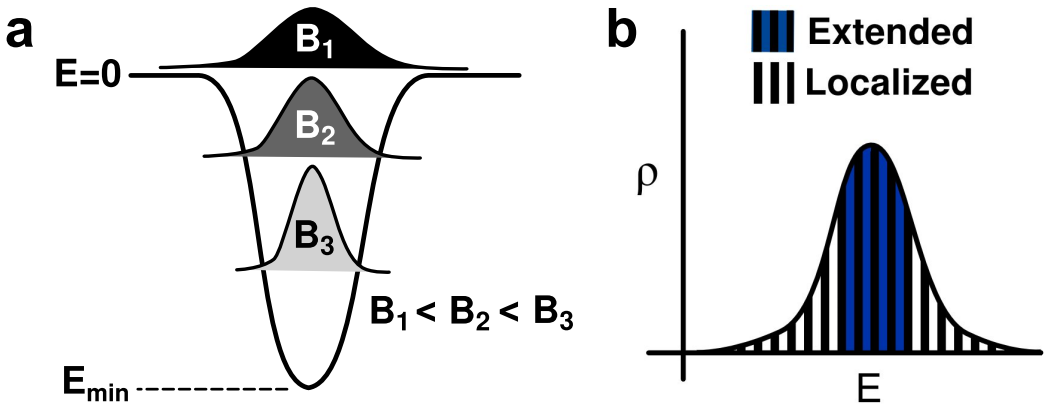


Figure 42: (a) In a magnetic field, the size of wavefunctions are on the order of the magnetic length. As the magnetic field ($B_i$) increases, the wavefunction size decreases. As a result, the wavefunction can more deeply probe hills and valleys in the electrostatic potential. (b) Localized and extended states in a inhomogeneity broadened Landau level.

these results. Even though our Landau level calculation results in delta function spikes at distinct energies, physical Landau levels typically have a broadened linewidth. In transport measurements, Landau levels are broadened in two primary ways: 1) limited carrier lifetime or recombination through the electron-phonon interaction and 2) spatial variation in the electrostatic potential. Let us assume, for now, that the carrier lifetime is sufficiently long and the magnetic fields high enough that the majority of the broadening is through local variations in the electrostatic potential.

Because magnetic fields reduce the size of the wavefunction and cannot do work, shifts in the local electrostatic potential are able to localize electrons in graphene. Figure 42a shows a 1-d schematic of the response of a wavefunction in a magnetic field to a dip in the local electrostatic potential. For high magnetic fields, the size of the wavefunction ($\approx \ell_B$) is small. A small wavefunction can more easily probe the depth of the potential well and is therefore more easily localized. At lower magnetic fields, the wavefunction expands and cannot "fit" within the boundary of the potential well. In this case, charge carriers are reasonably unaffected by its presence and lifetime broadening becomes the important source of broadening.

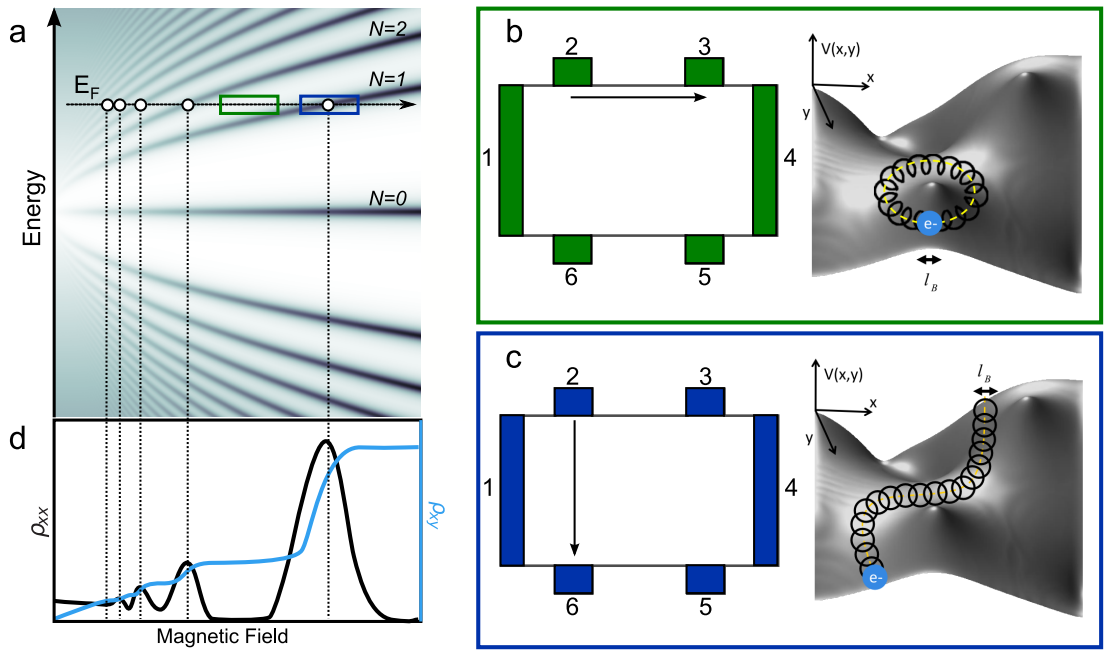


Figure 43: (a) The Landau level structure of graphene as a function of energy and magnetic field. The Fermi energy is shifted off of the Dirac point (and $LL_0$) either by using a back gate or from doping. LLs disperse to higher energies as the magnetic field is increased. When the magnetic field is set so that $E_F$ is between LLs, the graphene is in a localized state. Electrons at $E_F$ cannot traverse the sample due to localization around extrema in the electrostatic potential and must travel along the edge as in (b). Because of this, the longitudinal resistivity $\rho_{xx}$ drops. The crossing of a LL through $E_F$ reduces the filling factor $\nu$ (the number of filled LLs *times* the degeneracy). This increases the Hall resistivity $\rho_{xy}$ by quantized amounts and produces plateaus, (d) blue line. During this transition, the graphene is in an extended state, as in (c). The current follows saddle-point equipotentials in the sample and connects the terminals at contacts on opposite sides. Electrons drift along equipotential lines (yellow lines) while spinning in cyclotron motion (black spirals).

The wavefunction energies shift to reflect the so-called *potential landscape* of the surface. The net result is to smear the Landau level energy out over a certain energy distribution. The Landau level takes on a Lorentzian linewidth as shown in Fig. 42b. The spatial characteristics of the central energy of the inhomogeneity broadened LL and energies in the tails are quite different. The tails of the $LL^{av}$ represent the quantum states that are most significantly affected electrostatic potentials. These states lie at the bottoms of potential wells and are spatially separated. Because these states do not connect to one another and do not contribute to conduction, the tails of $LL^{av}$ are called the *localized states*.

In contrast, the center of $LL^{av}$ represents states that remain unshifted. These states

lie at the saddle points between hills and valleys of the electrostatic potential. Because an equipotential line can be drawn across the entire sample at this energy (for randomly distributed positive and negative potentials, as in Fig. 43b, right panel), these states are called the *extended states*. Therefore, the local density of states is spatially connected (Fig. 43c, right panel) and permits a pathway for conduction. The critical crossing point between extended and localized states is called the *mobility edge*.

In light of this, the behavior shown in Fig. 41b can be explained. Doping from contaminants on the film remaining from the fabrication process and from the SiC interface shift the Fermi energy ($E_F$) away from the Dirac point [Wu 2009]. As the magnetic field is increased, the LLs will disperse through $E_F$ (Fig. 43a). Between LLs, the Hall resistivity ($\rho_{xy}$) forms distinct plateaus. Figure 43b shows that within a plateau, the 2DES carriers are in localized states. Electrons which are put into the system are trapped by the inhomogeneities in the electrostatic potential over the sample. These localized states are able to receive electrons, but because the electrons cannot traverse the sample, they cannot contribute to the conductance. In this case, the current must flow along the edges of the sample. Electrons are able to move along the edges because the edges shift the chemical potential and bend the energy of the LLs (think of the edges as a boundary condition with an infinitely high potential). The chirality of the magnetic field establishes a direction of current flow at the top edge. The chemical potential there (2-3 edge, $\mu_{23}$) will be different from the bottom edge (5-6 edge, $\mu_{56}$) establishing a flow of charge carriers [Yoshioka 1998, MacDonald 1984]. States on these edges can be filled up to the chemical potentials of the contacts ($\mu_{23} \rightarrow \mu_1$ and $\mu_{56} \rightarrow \mu_4$). Because of this, the resistivity $\rho_{xx}$ drops when $E_F$ lies between LLs.

Upon increasing the magnetic field, the center of the LL will pass through $E_F$ (the boxed blue region in Fig. 43a). As discussed earlier, the 2DES forms an extended state. This is shown schematically in the right panel of Fig. 43c. The extended state destroys the edge current by allowing electrons at $E_F$ to move across the 2DES, driving the chemical potentials at the edges to equilibrium. The path of current is no longer along the edge, so

a peak is observed in $\rho_{xx}$. The Hall conductance is a quantized function of the number of filled LLs. Because the LLs disperse to higher energy with increasing magnetic field, the conductance drops as each LL passes through $E_F$ due to a decrease in the total number of filled LLs. It can be shown that the quantized conductance associated with a single Landau level is $e^2/h$ (assuming no extra degeneracies). The Hall conductance $G_{xy} = R_{xy}^{-1}$ (when $\rho_x x = 0$) is then just the quantum of conductance multiplied by the total number of filled LLs and the degeneracy factor (for graphene, 2 spin × 2 valley = 4).

The name "half integer quantum Hall effect" is given to graphene because of the non-dispersing zero energy LL ($LL_0$). It is clear from Fig. 43a $LL_0$ will never cross $E_F$. Therefore, it always remains half-filled. This half-filling adds a factor of $1/2$ to the conductance equation and gives graphene its unique quantum Hall structure:

$$R_{xy}^{-1} = 4(\nu + \frac{1}{2})\frac{e^2}{h}, \tag{65}$$

when $\nu$ has been used to denote the number of filled LLs [Jiang 2007, Novoselov 2005, Zhang 2005].

### 4.5.2 Local Density of States in a Magnetic Field and the Quantum Hall Effect

The spatial distribution of wavefunctions in 2D electron systems underlies the behavior of the quantum Hall effect. Inhomogeneities in the electrostatic potential provide regions for the localization of charge carriers. In the quantum Hall effect, this is necessary for the formation of well defined plateaus in the Hall resistance [Goerbig 2009, Davies 1998]. Fluctuations in the electrostatic potential provide regions in the material where charge carriers can be localized without contributing to the conductance. As the Fermi energy is raised so that the LL approaches half-filling, the localized regions of charge carriers begin to connect. This process is generally described as a *percolation*. Semiclassically, at half-filling, charge carriers circulate in cyclotron orbits about a guiding center which drifts along the spatially extended equipotential lines in the sample [Ando 1984, Huckestein 1995].

Much like filling an ice cube tray, once the water level is increased to the brim of the

individual ice cube cups, water can drip between them. When the tray is adequately filled, water molecules that are at the surface can be transported from one edge to the other without inhibition. The process of "filling" a LL is similar (at least to half-filling). In this analogy, electrostatic potentials create the *cups* that localize charge carriers.

As a consequence of the spin and valley degeneracy of each LL and the position of $LL_0$ at the Dirac point, magneto-transport measurements show quantized Hall conductance plateaus [$\sigma_{xy} = \nu e^2/h$] for filling factors $\nu = 4(N \pm 1/2) = \pm 2, \pm 6, \pm 10$ [Zhang 2005, Novoselov 2005, Wu 2009]. Recent transport measurements for both monolayer and bilayer graphene reveal apparent interaction effects that lift the energy degeneracy at other integer filling factors [Checkelsky 2009, Checkelsky 2008, Jiang 2007, Zhang 2006, Feldman 2009, Zhao 2010], and fractional quantum Hall plateaus have recently been observed on suspended graphene samples [Du 2009, Bolotin 2009].

In addition to electrostatic potentials and correlation effects, graphene has other unique properties which can affect the real-space structure of the LDOS. In Section 1.2.1.3, we showed that $LL_0$ has the unique property of sublattice polarization; that is, states in the $K_+$ ($K_-$) valley of the Brillouin zone are fully restricted to the A (B) sublattice. This is a direct consequence of the two component spinor-like wavefunctions which originate from the sublattice structure. Normally, this does not play a role in the LDOS, however if the sublattice degeneracy is split and the polarization maintained, the LDOS on each sublattice would be different.

### 4.5.3 Analysis of Surface Topography

Given the importance of electrostatic potentials to features in the LDOS, we first discuss the topography of the graphene surface that we studied. Figure 44a shows a scanning tunneling microscope (STM) topograph of the 100 nm × 100 nm area under study. A single defect is visible at the bottom of the image and a hexagonal superlattice height modulation (10 pm root-mean-square variation) is found throughout the region.

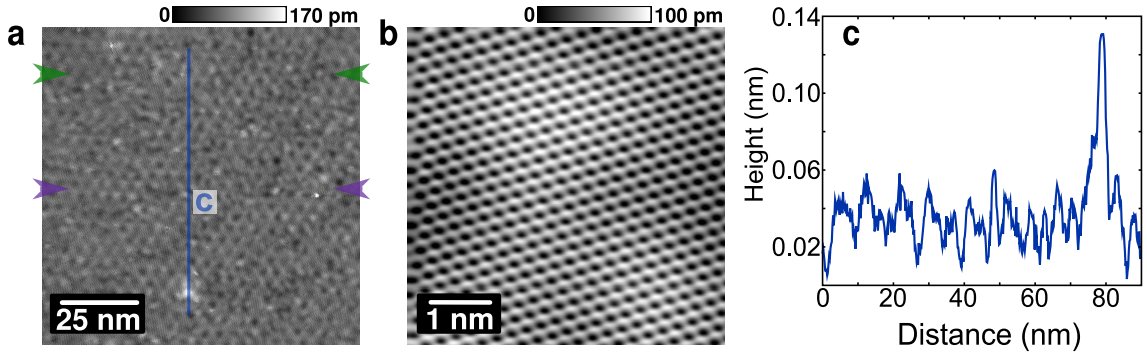


Figure 44: Topographic STM images of the multilayer epitaxial graphene sample grown on SiC. (a, L_25082) A 100 nm × 100 nm real-space image of the surface studied, taken at a sample bias of $V_s = 0.35$ V and a tunnel current $I_s = 400$ pA. This image was acquired simultaneously with the 8 T $dI/dV$ maps shown in Fig. 46. Periodic height variations are a moiré pattern of ≈ 4 nm period. A defect at bottom-center distorts the topograph due to an electronic perturbation. Arrows label the line corresponding to the spectral profiles of Fig. 52. (b, L_24993) A 5 nm × 5 nm image ($V_s = 0.10$ V, $I_s = 100$ pA, $x, y$ sampling increment 25 pm) showing the atomic lattice. c) A height profile showing the topographic variations in (a). The line cut goes through a defect at the lower/center part of the image in (a). The sample surface is very smooth with variations tip height due to the moiré pattern on the order of 10 pm RMS.

The superlattice is a consequence of the moiré alignment of two graphene layers, rotated slightly with respect to one another. The topographic moiré period of $(3.98 \pm 0.12)$ nm corresponds to a rotation of $\theta = (3.6 \pm 0.1)^\circ$ between graphene sheets [Hass 2008c]. Other than the defect seen in Fig. 44a, the graphene surface is well ordered with the graphene honeycomb lattice apparent in atomically-resolved images, as shown in Fig. 44b. Figure 44c shows a vertical height profile through the image (marked in blue in Figure 44a). The overall roughness of the sample surface is very low, on the order of 10 pm RMS. This is an upper bound on the true roughness, because the moiré is likely a modulation of the density of states and not a physical corrugation [Pong 2005b].

### 4.5.4 Spatial Mapping of Magnetically Quantized Electronic States

In this section, we investigate the unique spatial structure of the LDOS at energies around $LL_0$. Using the LTSTM at NIST, we apply the conductance mapping techniques previously described in Section 2.1.5.3. These experiments are performed at 4.3 K in magnetic fields up to 8 T.

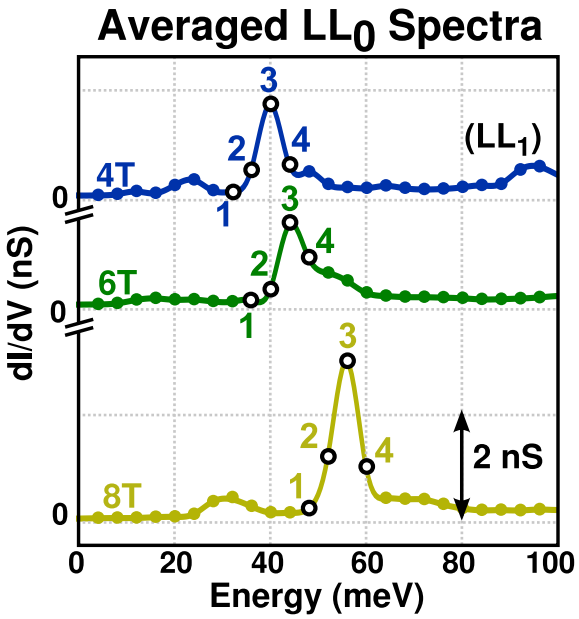


Figure 45: Spectra of $LL_0^{av}$ at magnetic fields of 4 T, 6 T and 8 T averaged over the area in Fig. 44a. Energy is $eV_s$, where $V_s$ is the sample voltage bias. Labels at marked energies (open circles) correspond to the displayed maps. The energy spacing between points is 4 meV, and the energy of the peak for $LL_0^{av}$ is labeled *#3* for each magnetic field spectra. Each number corresponds to a map which is displayed in Fig. 46. Lines are spline interpolants of the raw data (filled circles).

#### *4.5.4.1 Grid-Averaged Spectra*

The spectra in Fig. 45 are spatial averages at energies around $LL_0$. Each averaged spectrum consists of $251 \times 251 = 63,001$ point spectra in an evenly spaced grid over the 100 nm $\times$ 100 nm region of the sample displayed in Fig. 44a. $LL_0$ is the first LL observed above the Fermi energy $E_F$ (which lies at zero sample bias), indicating a filling factor $\nu = -2$ for all three magnetic fields.

For clarity, we refer to the averaged $LL_0$ in Fig. 45 as $LL_0^{av}$. This distinction is subtle, but important for understanding measurements of this kind. The averaged spectra which make up $LL_0^{av}$ collectively introduce inhomogeneity broadening into the measurement. For individual point spectra, the peak energy of $LL_0$ shifts to accommodate the local fluctuations of the electrostatic potential. Once these individual spectra are spatially averaged, the shifting LL peak energies broaden the resulting $LL^{av}$. Consequently, the $LL^{av}$ more

accurately describes transport LLs because it includes the effects of electrostatic inhomogeneities (which are extremely important to the spatial distribution of the density of states). When describing LLs in the context of transport phenomenon (such as the quantum Hall effect), we will use the notation $\mathrm{LL}^{av}$ and $\mathrm{E}_N^{av}$ to denote the peak energy of $\mathrm{LL}_N^{av}$.

The filling factor depends on the location of the Fermi energy within the $\mathrm{LL}^{av}$ spectrum. For all of the magnetic fields presented (4, 6 and 8 T), the Fermi energy lies between the $N = 0$ and $N = -1$ levels, so the filling factor is constant at $\nu = -2$. The Fermi energy $E_F$ occurs at zero sample bias in tunneling spectra, well below $\mathrm{LL}_0^{av}$, as is apparent from Fig. 45 (the $N = -1$ $\mathrm{LL}^{av}$ lies tens of meV below $E_F$). At zero magnetic field, $\mathrm{LL}_0^{av}$ lies $\approx 6$ meV below $E_F$.

In this work, as in [Miller 2009], the energy of $\mathrm{LL}_0$ is found to depend on the magnetic field. The matter awaits a full theoretical calculation, however, the general explanation is that the field-dependence of the LL peak energy for $\mathrm{LL}_0$ is a consequence of screening the electric fields from the substrate (which induces electron doping) and to some extent from the STM tip (which would tend to induce hole-doping due to the work function difference). The defect in the imaged area may also contribute to the charge density, partially pinning the Fermi level to an energy below $\mathrm{LL}_0^{av}$.

#### *4.5.4.2 dI/dV Maps*

Figure 46 shows a set of $dI/dV$ maps around $\mathrm{LL}_0^{av}$ for magnetic fields of 4, 6 and 8 T. Lighter colors (green, yellow) correspond to higher density of states. All of the $dI/dV$ maps show prominent rings around the defect imaged in the topograph of Fig. 44a. These are related to the defect potential and charge state [Martin 2009]. This is a complex interaction of electric and magnetic field effects [Kubista 2011].

Here we focus on general features of the $\mathrm{LL}_0$ spatial distribution. The 4 T $dI/dV$ maps in Figs. 46 display spatial patterns similar to LLs in a conventional 2DES [Morgenstern 2003b, Morgenstern 2003c, Hashimoto 2008, Niimi 2009]. Localized drift

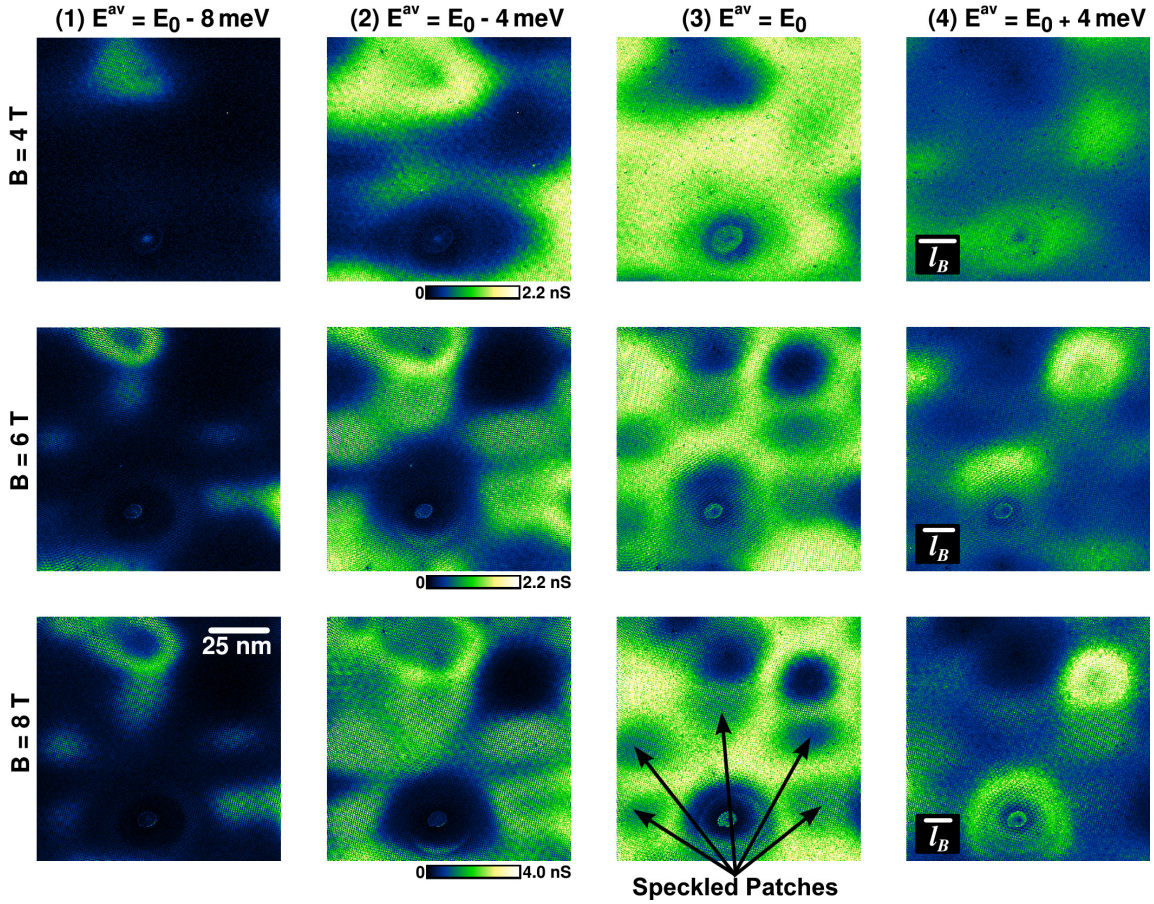


Figure 46: Spatial local density of states measurements at energies around $LL_0^{av}$ showing the extended states at the $LL_0^{av}$ peak energy and localized states at energies above and below the peak energy. Each row is a set of four maps at a single magnetic field and each column (1-4, marked in Fig. 45) are chosen at comparable energies along $LL_0^{av}$ for each magnetic field. STS $dI/dV$ maps of the 100 nm × 100 nm region are displayed for magnetic fields of 4 T (top row, L_25094), 6 T (middle row, L_24875), and 8 T (bottom row, L_25084). These maps (taken from a larger data set) were selected at energies bracketing $E_0^{av}$ for each magnetic field (note that areas probed at different fields are not in exact registry; the defect position can be used as an alignment guide). The magnetic lengths ($\ell_B$, shown in the right most column) correspond to values of 13 nm,10.5 nm and 9 nm, respectively. Following the maps down columns shows that $dI/dV$ features sharpen due to decreasing $\ell_B$. Left to right across rows, the maps show the change from states localized in potential energy minima, to extended states at $E_0^{av}$, to states localized around potential energy maxima (note the inversion of $dI/dV$ intensity from $E_0^{av} - 4$ meV to $E_0^{av} + 4$ meV). Rings at upper-left in columns (1) and (2) can be viewed as tracing equipotential lines that differ by 4 mV. At energy $E_0^{av}$, the drift state follows an equipotential that may span the sample. In 6 T and 8 T maps, patches with large pixel-to-pixel intensity variation appear.

states in the tails of the $LL^{av}$ follow closed paths around potential energy minima [low energy tail, Fig. 46(4 T, col. 1,2)] or maxima [high-energy tail, Fig. 46(4 T, col. 4)]. The bright triangular ring of large LDOS seen upper-left in Fig. 46(4 T, col. 1 & 2) is a good example. The width of the closed path is approximately the magnetic length ($\ell_B = \sqrt{h/(2\pi eB)}$), which is the size of the $LL_0$ wavefunction (see $\ell_B$ bars in column 4). Bright regions in Fig. 46(4 T, col. 2) complement those in Fig. 46(4 T, col. 4). This makes sense because opposite tails of $LL_0^{av}$ will be populated by localized states from inhomogeneities of opposite signs. At the central energy, Fig. 46(4 T, col. 3) shows that the extent of the drift state expands drastically. The LDOS is no longer confined to spatially separated patches [as in Fig. 46(col. 1)]. In the integer quantum Hall effect, coupling of edge states through this extended state destroys the zero longitudinal magnetoresistance.

The wavefunction size $\ell_B$ determines how accurately drift states can follow the local potential landscape (refer back to Figure 42a). The same features found at 4 T are seen more clearly resolved in the $dI/dV$ maps at 6 T [Figs. 46(row 2)] and 8 T [Figs. 46(row 3)] (*cf.,* the ring at upper-left in column 2).

#### *4.5.4.3 Correlation Maps*

The full set of $dI/dV$ maps represents a large quantity of data. A convenient way to get analyze the whole data set simultaneously is to produce a correlation map like in Figs. 47a,b. Each pixel of these images is the normalized cross correlation of two $dI/dV$ maps at different energies. Both axes of the image are in energy, indicating the energies of the two maps being correlated. The color scale indicates high correlation (blue) and high anticorrelation (red) between any two maps. The solid blue diagonal line across the image is the cross correlation of maps with themselves (i.e. $E_i = E_j$). Data is mirror reflected over this line, so only half of the map displays unique information.

The correlation maps can be used to analyze the spatial structure of peaks seen in the raw spectra. Mechanisms such as Van Hove singularities [Li 2009a], defect states

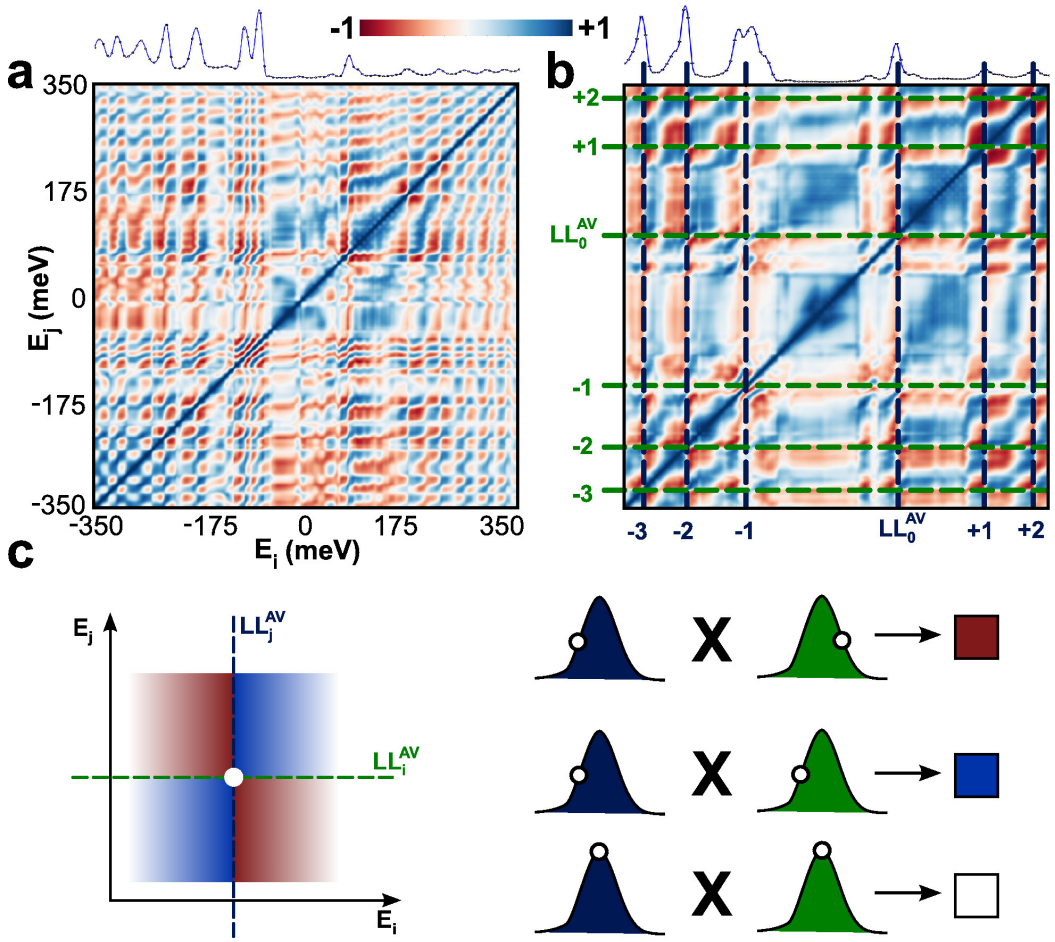


Figure 47: Cross-correlation maps for magnetic fields of (a) 4 T and b) 8 T (energy range is the same for both maps, $dI/dV$ spectra shown above each map). Both planar axes are $dI/dV$ energy, and each pixel of the cross-correlation map represents the normalized cross-correlation of two $dI/dV$ maps at energies $E_i$ and $E_j$. Blue represents maps of high correlation, while red represents anti-correlation. The solid blue diagonal line is the cross correlation of maps with themselves (representing maximal correlation). The map in (b) has dashed lines drawn to indicate where $LL^{av}$ peaks occur. The intersection of two LLs always has the same structure: high correlation in directions parallel to the center-diagonal, and anti-correlation in directions which are perpendicular. This behavior is described in (c). The correlation of maps on the same side of any two LLs have a high correlation, while the correlation of maps on opposite sides are anti-correlated. This behavior is expected within the drift state localization picture.

[Brar 2010] or tip-induced quantum dots [Dombrowski 1999] can also produce peaks in the density of states. Unlike these density of states features, the spatial structure of LLs can be identified because they follow the drift state localization picture. The localization of electron density around hills and valleys in the electrostatic potential at opposite energy tails of the $LL^{av}$ produces a defined checkerboard pattern in the correlation of any two LLs in the map. It should be noted that the maps were Gaussian smoothed inside an 8 pixel radius (3.2 nm), so these maps represent the correlation of larger scale features. In order to compare LLs in the drift state picture (at length scales closer to $\ell_B$), we neglect small-scale features.

Lines are drawn in Fig. 47b and energies coincident with $LL^{av}$ peaks. The numbers mark the $LL^{av}$ index of the peak. Figure 47b is the correlation map of the data from 8 T. The correlation map in Fig. 47a is much more complex, because it is done at 4 T. The 4 T spectrum has many more LLs inside the same energy range as 8 T.

The intersection of two LLs produces a correlation-anticorrelation saddle point. Figure 47c shows why this occurs. When $E_i$ and $E_j$ are selected from the same side of any two LLs, the features of the maps are correlated. Because the sign of the inhomogeneities are responsible for the broadening, two maps from opposite sides will be anticorrelated, while two maps from the same side will be correlated. Looking back at Fig. 46, one can see that this is the case. Images from Fig. 46(col. 2) and Fig. 46(col. 4) are taken from opposite sides of $LL_0^{av}$, thus they have *inverted* intensities from localized states created by electrostatic potentials of opposite sign. Additionally, one can identify saddle points between LLs. If the LLs are well separated, the tails do not have much overlap, and the LDOS will remain *polar* on either side of a LL with the sign of the inhomogeneities. Therefore, similar saddle point behavior occurs in the correlation; however, because the cross-correlated maps are from opposite signs, the maps are anti-correlated in directions parallel to the diagonal center line (lower left/upper right squares of the checkerboard are anti-correlated between LLs).

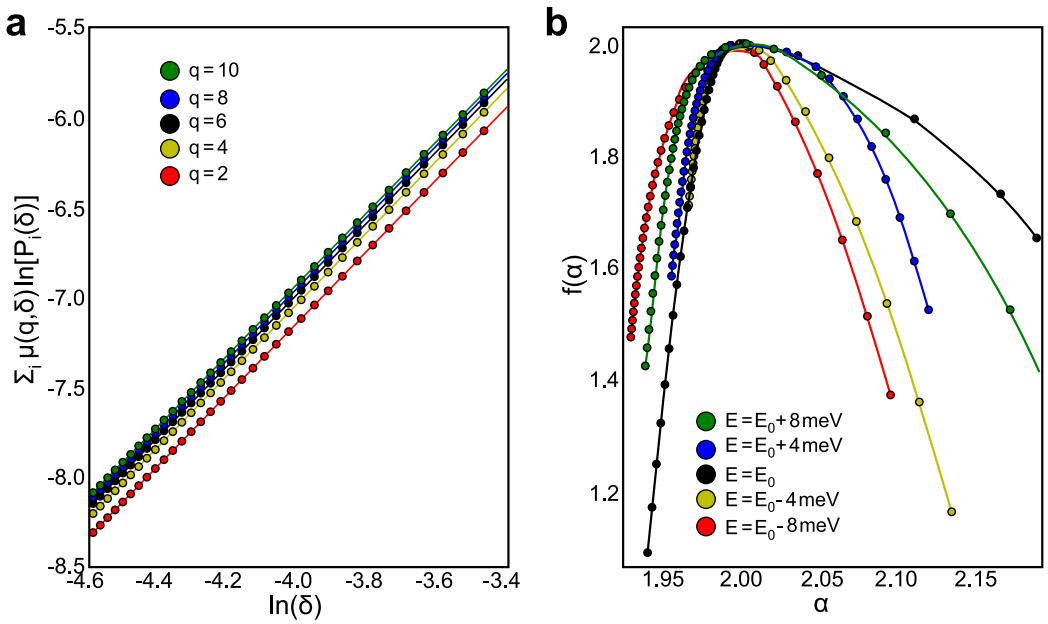


Figure 48: Multifractal analysis of the maps shown in Fig. 46 (8 T only) (a) A plot of the numerator vs. the denominator equation 67, the fractal dimension $\alpha$, for various values of q. Similar plots are used for $f(q)$, and the slopes of the fit lines are used to plot $f(\alpha)$. (b) The resulting plot of $f(\alpha)$ for various maps around $E_0^{av}$. The apex of the parabolic curve at the center of $LL_0^{av}$ gives a value of the scaling parameter $\alpha \approx 2.0$.

Correlation maps show that the behavior of the observed peaks are consistent with that of LLs from the localization picture. Recently, photocurrent maps of a graphene hall bar in a magnetic field have also shown oscillatory patterns, resulting from the same mechanism [Nazin 2010].

#### *4.5.4.4 Multifractal Analysis*

Localized states cross-over into extended states at the *mobility edge*. The equipotential lines that run between localized states follow the saddle points of the electrostatic potential. Electrons at $E_F$ following closed contours inside the hills and valleys of the "potential landscape" begin to *percolate* to the saddle-point equipotentials as $E_F$ approaches the mobility edge. Near this point, the fast cyclotron motion of the electron orbits begin to overlap and quantum interference effects (tunneling) can even take effect [Huckestein 1995].

For a conventional 2DES, the scaling of the localization length near the mobility edge

is known to diverge as [Aoki 1985, Huckestein 1992]:

$$|E - E_{LL}|^{-\nu}. \tag{66}$$

Using multifractal analysis on STS conductance map data, it was shown that this method might be used to quantify the scaling exponent ($\nu$) [Morgenstern 2003c]. Multifractal analysis is a method which calculates the $q^{th}$ *moment* ($\mu$) of the LDOS by dividing the area into boxes of length $\delta$. The fractal dimension $\alpha(q)$ and the Hausdorff dimension $f(q)$ are calculated as [Chhabra 1989]:

$$\alpha(q) = \lim_{\delta \to 0} \sum_i \frac{\mu_i(q,\delta) \ln[P_i(\delta)]}{\ln(\delta)} \tag{67}$$

$$f(q) = \lim_{\delta \to 0} \sum_i \frac{\mu_i(q,\delta) \ln[\mu_i(q,\delta)]}{\ln(\delta)} \tag{68}$$

where P is the probability (given by the average $dI/dV$ in the box multiplied by the area of the fractional box). The largely linear plot of these two values vs. $\ln(\delta)$ (Fig. 48a) allows us to take the slope of these lines and obtain $f(q)$ and $\alpha(q)$. Most importantly, the resulting values can be plotted together to obtain the singularity spectrum $f(\alpha)$ [Chhabra 1989]. The $f(\alpha)$ spectra for the measured $dI/dV$ maps are characteristic of the quantum phase transition in the center of a LL [Morgenstern 2003c]. The apex of the resulting parabolic curves corresponds to the scaling parameter $\nu$.

Figure 48 shows the multifractal analysis of the map in Fig. 46 at $B = 8\,\mathrm{T}$. The plot of the numerator vs. the denominator of equations 67 and 68 show the required linear trends. Taking the slope of these lines gives the values of $f(q)$ and $\alpha(q)$, which can be plotted together as parametric equations of q. The result is shown in Fig. 48b.

The right halves of the curves in Fig. 48b deviate from a parabolic shape. This is likely indicating that our maps are not large enough for this analysis to be effective given the size of the observed features. The apex of the parabolic curve at $E_0^{av}$ does not shift much from the other curves and is at a value of $\alpha \approx 2.0$, significantly lower than the expected values of $2.26-2.35$ calculated from theory [Evers 2001, Huckestein 1990]. Other

attempts at using multifractal analysis on $dI/dV$ map data have also resulted in a scaling parameter of $\alpha \approx 2.0$ [Morgenstern 2003c], and concluded that the thermal contribution to the energy resolution was too large. In the present case, it is certainly the case that our energy point density (4 meV) is not high enough to perfectly resolve the exact position of the peak extended state. Future measurements done at lower temperatures (~milliKelvin) might be more successful at producing a measurement of the scaling parameter if a dense set of energy points is used.

#### *4.5.4.5 Unconventional Localization*

Aside from the expected localization behavior from inhomogeneities in the surface potential, new features also appear in the density of states maps. With increasing magnetic field, the extended state in Figs. 46(col. 3) develops a pattern with high density of states confined to narrow channels separating lower-density patches of diameter $> \ell_B$. These patches show large pixel-to-pixel fluctuation of intensity [the fluctuations are most apparent at 6 T and 8 T in Figs. 46(col. 2)]. Magnetically induced LDOS variation on a length scale $\ll \ell_B$ is unexpected and qualitatively different from any previous STS measurements on a conventional 2DES.

The fluctuation in the patches can be easily visualized in the raw data by performing a color addition of maps at energies on either side of $LL_0^{av}$. The 8 T map at $E = 52$ meV is colored black to red (Fig. 49a), and the map at $E = 60$ meV is colored black to green (Fig. 49b). Because these are both in the tails of $LL_0^{av}$, overlapping of localized states should not occur within the standard picture. Overlapped regions should color-add to produce patches of yellow. Figure 49c shows the addition of parts (a, red) and (b, green), making apparent the yellow regions of unconventional localization.

Interestingly, if we zoom in on one of these regions, as in Fig. 49d (expanded from the white box in Fig. 49c), we find that the individual pixels of the map are *speckled* green and red. Intensity of the LDOS is varying rapidly on scales far below $\ell_B$.

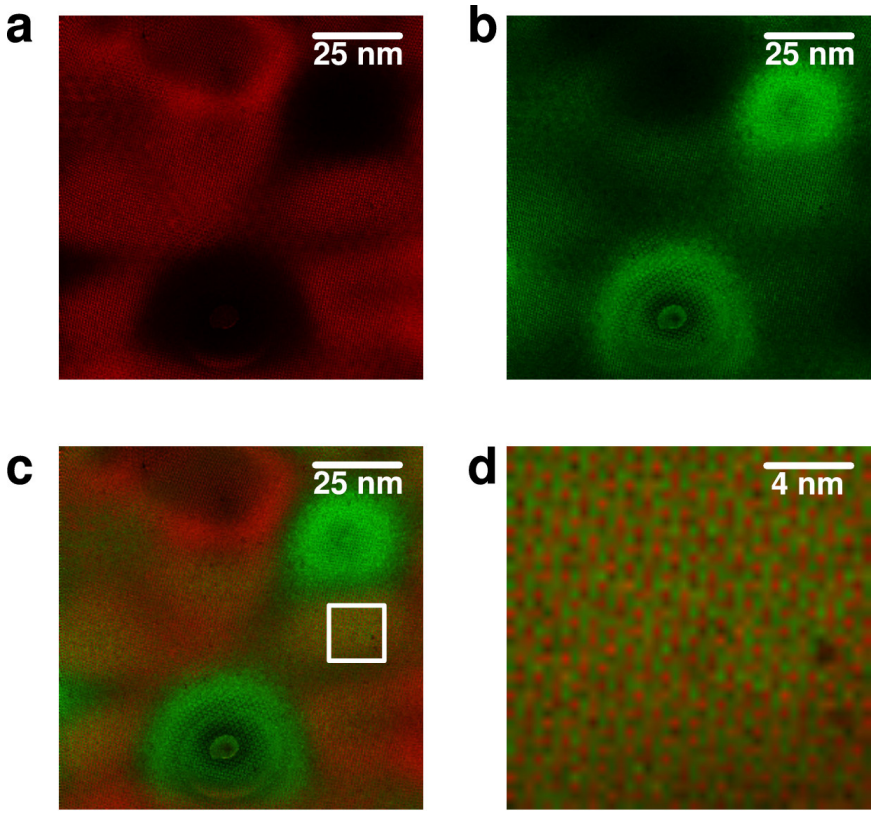


Figure 49: Small scale fluctuations seen in the raw $dI/dV$ data acquired at a magnetic field of 8 T. Images were taken (a) at 52 meV, $\approx$ 4 meV below the $LL_0^{av}$ peak (see Fig. 45), and (b) at 60 meV, $\approx$ 4 meV above the $LL_0^{av}$ peak. In (a)/(b), zero differential conductance is shown as black and the maximum differential conductance of 5 nS is red/green. (c) The sum of red and green images in (a) and (b). The speckled patch marked by a white box is shown expanded in (d).

To get a better understanding of how the energy of the $LL_0$ peaks in the point spectra shift as a function of position, we make a map of $E_0(x, y)$. For Fig. 50, the energy of the $LL_0$ $dI/dV$ maximum ($E_0$) was determined by fitting a Lorentzian peak to the spectrum at each $(x, y)$ pixel, using a nonlinear least squares algorithm (Levenberg-Marquardt in MINPACK). Fit parameters were the peak-center energy $E_0$, the Lorentzian width, and the peak amplitude. Figure 50 plots the fitted $E_0$ values at each pixel at magnetic fields of 4 T (a), 6 T (b), 8 T (c).

A region of high peak-energy is apparent near the topographic defect (see Fig. 50c). A second broad maximum can be seen in the upper-right quadrant of Fig. 50c, while a dip in $E_0(x, y)$ occurs near the top-center. Within the drift state picture, $LL_0$ follows equipotential

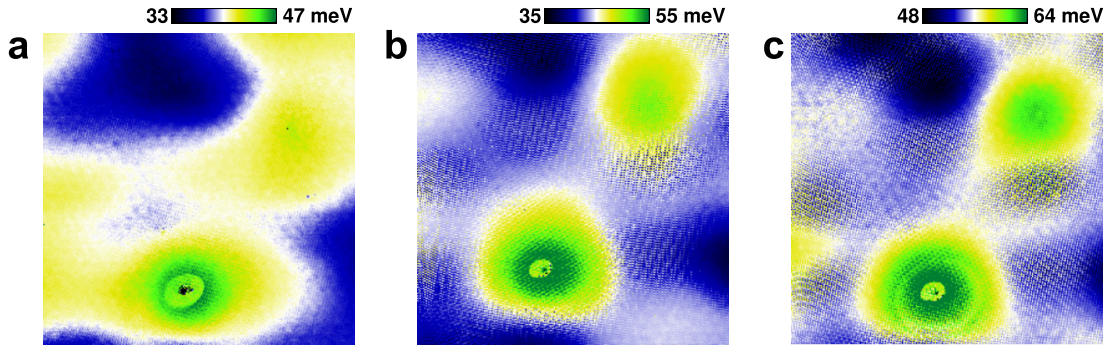


Figure 50: Maps of $E_0(x, y)$ for magnetic fields (a) 4 T, (b) 6 T, (c) 8 T. In (a) there are no apparent small scale fluctuations. As the field is increased in (b) and (c), the fluctuations in the peak of $LL_0$ become apparent. The influence of inhomogeneities is also apparent in this map. In (c), over much of the area, $E_0$ varies smoothly, reaching a maximum at the position of the defect seen in Fig. 44a (omitting the defect core). A second maximum (top-right) and a minimum (top-center) could be due to unresolved defects. Several speckled patches can be seen, where $E_0$ varies over distances shorter than the 0.4 nm sampling distance.

lines for length scales greater than $\ell_B$, therefore we associate these broad $E_0(x, y)$ features with maxima and minima in the electron potential energy. The increase in $E_0$ over the topographic defect (bottom-center) is consistent with a negatively-charged configuration. The sources of the second potential energy maximum (upper-right) and the potential energy minimum (top-center) are not resolved in the topograph, but a natural explanation would be the presence of other isolated defects or intercalant atoms.

The effect of increasing the magnetic field (left to right in Fig. 50) is clearly visible in these plots. At 4 T, the $LL_0$ peak energy is uniform on much larger scales, indicating a larger width of the $LL_0$ wavefunction. Also, there are not small scale fluctuations present. The fluctuations are induced by the magnetic field and appear to "shut off" below 4 T.

For 6 T and 8 T, inside each of the patches in areas like box I (marked in Fig. 51) the peak-tracking map shows a speckled pattern, indicating large pixel-to-pixel variation of $E_0$. An expanded view of the speckle within box I of part (a) is shown in Fig. 51b. From this patch and from a region that shows no speckle (box II), we produce histograms of $E_0$ values, as shown in Fig. 51c. In region II, all $LL_0$ peaks are found to lie close to the mean energy. Within patch I, however, $E_0$ values cluster around two distinct energies separated

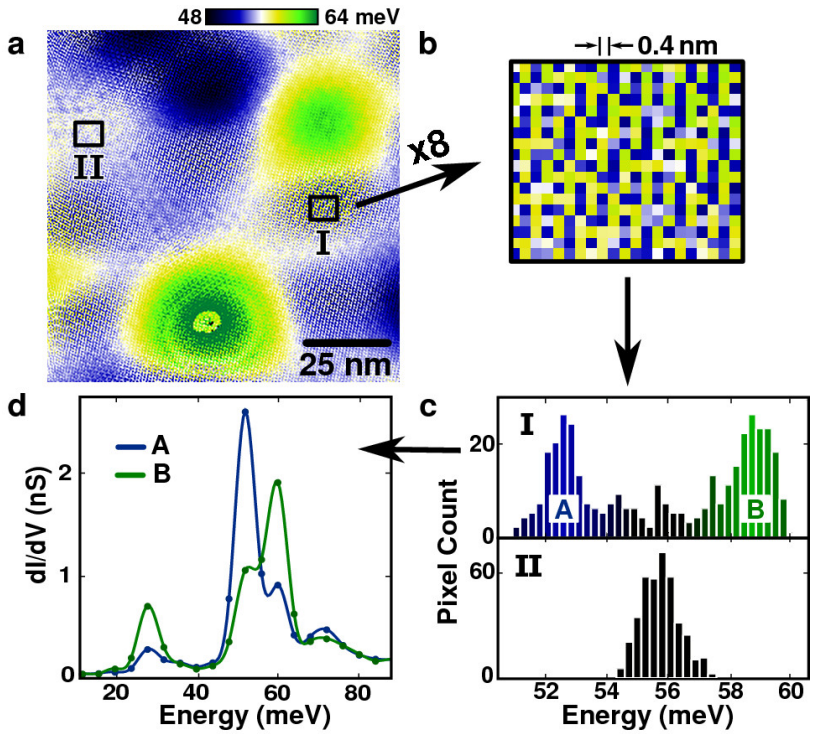


Figure 51: Closer inspection of Fig. 50c. (a) The $E_0$ tracking map for 8 T. (b) Expanded view of the speckle displaying large pixel-to-pixel variations of $E_0$. (c) Histograms of $E_0$ values from boxes I & II in part (a). In the speckled patch I, the histogram (top) has two distinct peaks (A & B) separated by 6 meV. A single peak is found in the bottom histogram from unspeckled region II. (d) Average $dI/dV$ spectrum obtained from pixels in the high-count bin (52.5 meV $< E_0 <$ 52.75 meV) under histogram peak A (blue) and from pixels in the high-count bin 58.5 meV $< E_0 <$ 58.75 meV) under peak B (green). We associate these with the valley-split $LL_0$ LDOS on sublattices A and B.

by more than 6 meV.

These features establish that the LDOS energy distribution varies on the atomic scale within each speckled patch. Clearly, this behavior falls outside of the drift state picture and—unlike the broad maxima and minima in $E_0(x, y)$—is not exclusively associated with the isolated defects. At 0.4 nm pixel spacing, the atomic lattice (0.246 nm lattice constant, 0.142 nm C-C bond length) is under-sampled in these LDOS maps due to time constraints in data acquisition, but the *resolution* is $\ll$ 0.4 nm (*cf.* Fig. 44b, acquired with the same STM tip), i.e., a large sampling increment does not broaden underlying features. Therefore, the exact atomic LDOS is not determined directly in the present data, but the bimodal distribution of $LL_0$ peak energies clearly suggests different LDOS on the A and B carbon

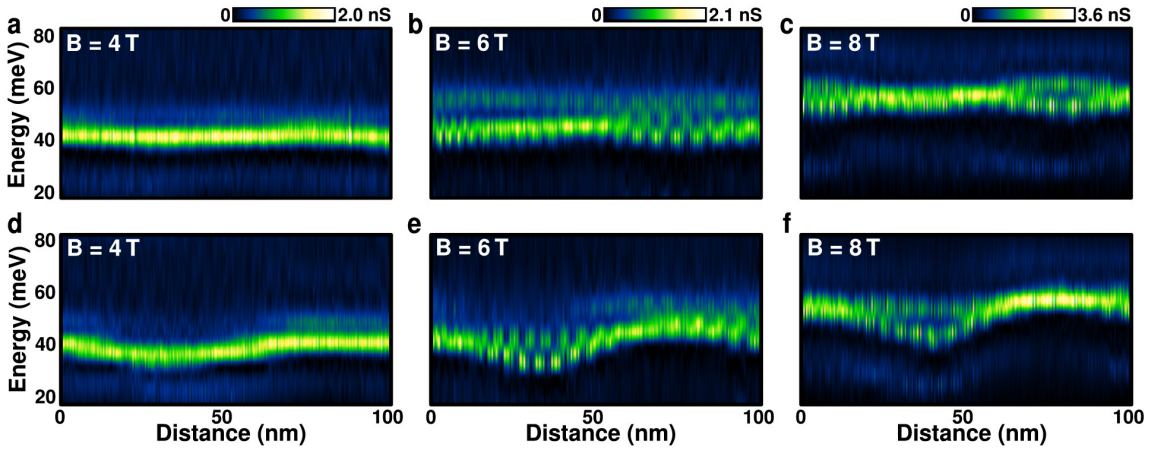


Figure 52: Magnetic field dependence of the spatially varying $LL_0$ peak energy. $dI/dV$ magnitude (color) versus energy (vertical) and position (horizontal) along the line marked by arrows in Fig. 44a. The yellow arrows in Fig. 44a correspond to the location of the line cuts in (a-c), while the green arrows correspond to the location of the line cuts in (d-f). The spectral profiles were extracted from $dI/dV$ maps at (a,d) 4 T, (b,e) 6 T, and (c,f) 8 T. The bright $dI/dV$ peak is $LL_0$. Within a speckled patch (centered at 35–40 nm in d-f), an energy gap is observed for fields above 4 T. The $dI/dV$ intensity of the two bands is anticorrelated: At any spatial position (pixel), large $dI/dV$ in one band corresponds to small $dI/dV$ in the other. Note that the $\approx 5$ nm intensity modulation of the bands is an aliasing artifact due to undersampling of the graphene lattice.

sublattices. Given the sublattice polarization of the spinor-like wavefunctions in $LL_0$, the histogram energy gap is "valley-splitting."

Figure 51d shows the average spectrum from the high-count bin within the low-energy peak of the histogram (labeled A) and the average spectrum from the high-count bin in the high-energy peak (B). We interpret these as sublattice polarized, valley-split LDOS spectra from each of the A and B sublattices.

The spatial and magnetic field variation of valley-splitting in the $LL_0$ states can be seen in profiles of the $dI/dV$ intensity versus energy along a line crossing one of the speckled patches. Figures 52(a-f) show these spectral profiles taken from $dI/dV$ maps (information about spectral profiles is given in Section 2.1.5.2). The profiles show spectra across the same lines at magnetic fields of, 4 T (a,d), 6 T (b,e), and 8 T (c,f). The progression of the energy gap can be seen in Fig. 52 (a-c). At 4 T, there is no apparent energy gap. As the magnetic field is increased to 6 T, gaps on the left and right side of the profile begin to form.

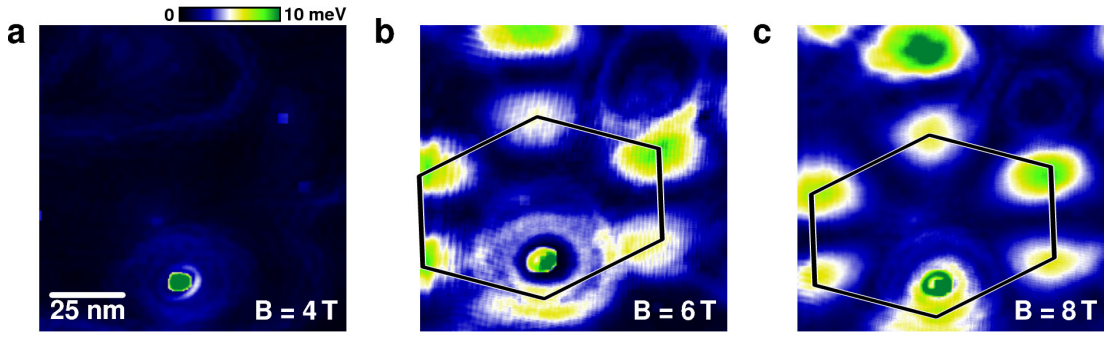


Figure 53: Gap maps ($\Delta(x, y)$) for magnetic fields of (a) 4 T, (b) 6 T, (c) 8 T. The quasi-hexagonal figures in (b) and (c) are identical. Note that maps at different magnetic fields are not in exact registry; the defect (bottom-center) can be used to judge positional displacement between maps.

By 8 T, the gaps are distinct and easily resolved. The splitting does not appear to change in regions where the electrostatic potential has shifted the LL. In the 4 T profile of Fig. 52d, the peak energy $E_0$ dips slightly over the patch, but does not split. At 6 T a clear energy gap develops, reaching a maximum of $\approx$ 8 meV, but no gap is found in unspeckled regions. By 8 T the splitting has increased slightly to $\approx$ 10 meV. In both spectral profiles, the valley-splitting occurs only above a threshold field $B_*$ where $4\,\mathrm{T} < B_* < 6\,\mathrm{T}$ and may saturate at high fields to a value somewhat larger than 10 meV. Close examination of Figs. 52c and 52f also shows anticorrelation of the $dI/dV$ intensity in the two bands, as expected from the pixel-to-pixel fluctuations seen in the $E_0(x, y)$ maps of Fig. 50. This is additional evidence from raw data of sublattice polarization.

#### *4.5.4.6 Gap Maps*

We observe the spatial distribution of the valley-splitting by producing *gap maps* [Pan 2001]. Gap maps display the size of the gap (color) over the entire spatial area studied from Fig. 44a. Figure 53 was generated from the $E_0(x, y)$ maps described in Fig. 50(a-c). The standard deviation of $E_0$ over a box of size 3 pixels $\times$ 3 pixels, was collected over the extent of the image. The standard deviation was multiplied by $2\sqrt{2}$ in order to obtain the local energy gap. This scaling is exact only for a perfectly bimodal distribution of $E_0$ values. Fig. 51c (top) shows that histogram peaks A and B have finite widths. Because these widths

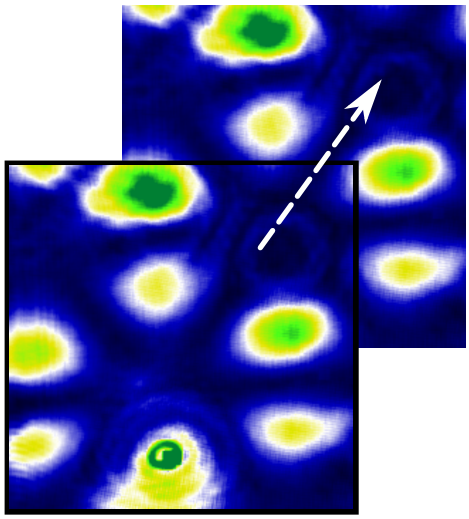

Figure 54: The 8 T gap map of Fig. 53c (black outline) shown on top of the same map shifted in position by a superlattice period (white arrow). This illustrates that the positions of the gaps at the edges of the map are consistent with a continued hexagonal distribution.

also contribute to the standard deviation, the energy gap $\Delta = E_0(B) - E_0(A)$ is slightly overestimated [$E_0(A)$ and $E_0(B)$ denote energies of the respective histogram peaks]. The size of the calculation box and the influence of defect potentials creates some artifacts, but $\Delta$ obtained from the rapid spatial variations is generally large by comparison.

The gap maps reveal a large scale spatial distribution of the valley-split patches, summarized in Fig. 53. The valley-split patches form a large hexagon (slightly distorted), with sides of length $\approx 40$ nm. In Fig. 54, we show that partial patches at the edges of the gap map are consistent with a repeating pattern of patches with a 70 nm period. Gap maps for magnetic fields of 6 T (Fig. 53b) and 4 T (Fig. 53a) show that the long-range pattern is nearly identical at 8 T and 6 T (with similar maximum energy gaps), but at 4 T the valley-split patches vanish entirely (seen also in Fig. 52a).

Figure 54 demonstrates that the faint regions of increasing brightness seen at the upper-right edges of Figs. 53(b,c) are consistent with an extended periodic hexagonal pattern. Similar shifts match with other edge-truncated patches in the map.

#### *4.5.4.7 Discussion*

We have imaged the $LL_0$ drift states of graphene, identifying magnetically-localized states above and below the Dirac point, and an extended state that lies at the peak energy of $LL_0^{av}$. The drift states at $E_0^{av}$ follow equipotentials over length scales larger than the magnetic length $\ell_B$, and, in general, agree with the drift-state localization picture of the quantum Hall effect. The presence of magnetically-localized states and the extended state are essential for the observation of the half-integer quantum Hall effect in graphene. From our results it appears that the basics of the drift-state picture remain valid at energies both above and below $LL_0^{av}$.

The "unconventional" localization from the previous section has been characterized. It is not expected within this framework and has not been predicted for MEG or any graphene system. Thus, we consider theoretical possibilities to explain the following observations:

- Above a threshold magnetic field $B_* \gtrsim 4\,\mathrm{T}$, we find spatial variation of the $LL_0$ energy on the atomic scale. These variations occur only within small patches of size comparable to the magnetic length.

- Within each patch, two distinct spectra are found, with the $LL_0$ energy difference apparently saturating to $\approx 10\,\mathrm{meV}$ for fields greater than $B_*$.

- The two spectra appear to be due to different local density of states on the $A$ and $B$ carbon sublattices, consistent with sublattice polarization.

- The "valley-split" patches themselves form a larger hexagonal pattern that appears to repeat with a period of $\approx 70\,\mathrm{nm}$.

There are numerous mechanisms by which symmetry breaking can occur in graphene [Yang 2007]. Most of these involve Coulomb interactions between electrons in many-body

systems. Recent local measurements of exfoliated graphene on $SiO_2$ have found that localization in this system is not dominated by single particle effects, but by Coulomb repulsion of charge carriers [Martin 2009]. For graphene, the theory of correlated states continues to evolve [Castro Neto 2009], and in most cases no ordered spatial symmetry breaking is discussed. A few models, such as a ground state Wigner crystal/bubble phase [Poplavskyy 2009] or a pseudospin vortex lattice [Nomura 2009], could produce spatial inhomogeneity comparable to the pattern that we observe. While we cannot exclude these types of many-body effects entirely, there are a few points which make such explanations improbable.

First, the Fermi energy is not aligned at the Dirac point with $LL_0^{av}$. Fig. 45 shows the energy of $E_0^{av}$ at 4 T, 6 T and 8 T, which is 44-56 meV above $E_F$. Creation of an energy gap in unfilled states (positive sample bias, $V_S > 0$) does not lower the total energy of the system and therefore should not be preferred. Secondly, the spatial distribution of valley-split patches does not vary with magnetic field from 6 T to 8 T (see Fig. 53b,c). In the absence of pinning centers, a pattern created by density-dependent interactions should change with magnetic field since the LL density of states varies with field. Lastly, a high density electron-doped layer ($n \approx 5 \times 10^{12}\,\mathrm{cm}^{-2}$) lies at the interface with the silicon carbide substrate, less than 4 nm below the top graphene layer in the multilayer stack [de Heer 2007, First 2010]. Screening by this interface layer should reduce Coulomb correlations. This does not preclude an interaction-driven state, but formation of a pattern with a unit cell much larger than the film thickness would be less probable.

In view of this, an explanation involving single electron interactions is more likely to describe our data. A small contribution of intervalley orbital currents is known to lift the $LL_0$ valley degeneracy [Luk'yanchuk 2008], but the predicted energy gap offers no spatial inhomogeneity and is even smaller than the ordinary Zeeman splitting (i.e., $\lesssim \mu_B B$, where $\mu_B$ is the Bohr magneton), which itself is unobserved in these 4.3 K experiments. We propose instead that our observations indicate a subtle interaction of the top graphene layer

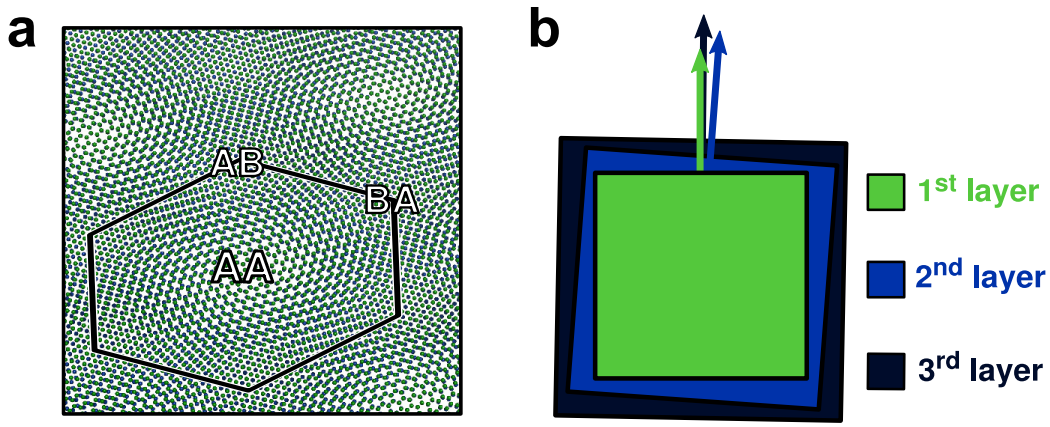


Figure 55: (a) Model of the moiré alignment of two graphene sheets. The top model layer (green) is aligned with the sample crystallographic axes, but the atomic unit cell is larger for illustration. The second model layer (blue) is slightly rotated with respect to the top layer and strained uniaxially by 0.25%. The model shows that the observed quasi-hexagonal symmetry in Fig. 53 follows naturally from a large moiré superlattice with small relative strain [Miller 2010a]. The valley-split patches in Fig. 53(b,c) correspond to AB/BA patches in the model. Since this large moiré superlattice is not seen in the topography, the energy gaps are most likely a consequence of interaction between the first (top) and third graphene layers. (b) Schematic of an orientation of the top three layers that would produce the observed short-period (STM) and long-period (STS) moire patterns.

with the layers below, which comprise an atomically-smooth and ordered substrate.

When considering two layers in multilayer epitaxial graphene (not necessarily adjacent layers), it is possible to find periodic regions of atomic alignment/misalignment between the layers (see Fig. 55a or Fig. 6). Where local atomic alignment occurs, the stacking is AA-like. That is, each atom in one layer has an adjacent atom beneath it in the opposing layer. In local regions of misalignment, the stacking is AB- or BA-like. Unlike AA stacking, the AB/BA regions are sublattice inequivalent, meaning that the presence of atoms in adjacent layers creates an asymmetry in the electrostatic potential between each of the two atoms of the sublattice. A model moiré superlattice is shown in Fig. 55a with a reasonably small rotation angle ($\theta = 1°$), so that regions of AA, AB, and BA stacking are apparent. Within the superlattice cell, the sublattices remain equivalent (due to the reversal of AB to BA stacking inside the superlattice cell) and the linear band dispersion of graphene is preserved near the Dirac point [Hass 2008c, Hass 2008a, Sprinkle 2009, Latil 2007, Lopes dos Santos 2007,

Mele 2010]. Superlattice Van Hove singularities [Li 2009a] were not observed within the energy range of our $dI/dV$ maps. Figure 55b illustrates how multiple layers typically have different rotational alignment. STM topographs over other regions of this sample show the effect of one moiré interfering with another below it (a double moiré), easily creating superlattice periods of tens of nanometers [Miller 2009] and requiring the participation of at least 3 graphene layers, as illustrated.

AB/BA stacking creates different environments for atoms on different sublattices, which can be modeled phenomenologically as a small difference in on-site potential — a *staggered potential*. For magnetic fields where $\ell_B$ is much larger than the size of the AB/BA patches, the staggered potential has little effect, but at fields where the wavefunction size becomes smaller than an AB/BA patch, the staggered potential is important. Figures 56a and 56b illustrate the $LL_0$ LDOS distribution over the A/B sublattices and the effect on the energy spectrum induced by the staggered potential. This simple picture explains the appearance above a threshold field of a hexagonal array of valley-split patches over the AB/BA regions. As shown in Fig. 55a, straining one graphene lattice uniaxially by less than 0.25% with respect to the other accounts for the distortion of the superlattice cell from a regular hexagon [Miller 2010a]. Considering a perturbative approach, the sublattice-polarized LDOS distribution of $LL_0$ is also explained since wavefunctions are unaffected in the first-order of perturbation (in fact, to all orders for a uniform staggered potential). However, the observed valley-splitting is smaller than one might naively anticipate from an interaction between first (top) and second graphene layers. More importantly, the size of the presumed moiré pattern is much larger than the single moiré superlattice imaged in the topography (which we attribute to the first and second graphene layers). Therefore, although in Fig. 44 we do not directly image the moiré between first and *third* graphene layers, we suggest that this is the interaction responsible for the spatially inhomogeneous valley splitting.

The proposed mechanism has some similarities to a lattice-scale charge density wave

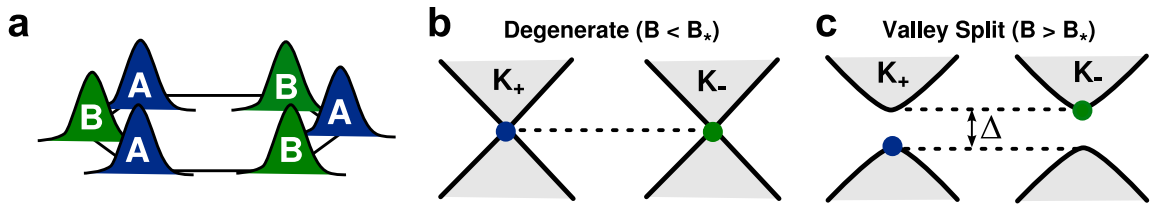


Figure 56: (a) Schematic wavefunctions of $LL_0$ in graphene. A and B label the sublattice atoms; blue denotes states from the $K_+$ valley of the graphene Brillouin zone and green corresponds to states from the $K_-$ valley. (b) Schematic of $LL_0$ states at the $K_\pm$ points with zero potential difference between sublattices (zero staggered potential). (c) $LL_0$ states at the $K_\pm$ points with nonzero staggered potential.

[Fuchs 2007, Alicea 2006, Khveshchenko 2001]. It is conceivable that the interlayer interaction could locally promote this type of instability, but in the present case, no energy would be gained by opening a gap in the unoccupied $LL_0$. Using a tight-binding model to investigate the influence of a small staggered potential and spatial inhomogeneity in the staggered potential arising from the moiré alignment of graphene layers, the presence of the gap can be explained [Miller 2010b, Kindermann 2010]. Consideration of the microscopic foundations of the model (using tight-binding parameters fitted to experiment [Dresselhaus 2002, Partoens 2006]) shows that our observed valley splitting of $\approx 10\,\mathrm{meV}$ is consistent with a first-layer/third-layer interaction. The model also produces a sublattice-polarized LDOS and an exponential suppression of the valley-splitting for moiré period $\ell \lesssim \ell_B$. The latter result implies a threshold magnetic field $B_*$ determined by $\ell_B \approx \ell$, which furthermore explains the negligible influence of the 4 nm first-layer/second-layer moiré on the valley splitting since $\ell_B \gg 4\,\mathrm{nm}$ at all fields studied here.

# CHAPTER V

# CONCLUDING REMARKS

## *5.1 Summary*

We have used various techniques of the scanning tunneling microscope to characterize multilayer epitaxial graphene. In Chapter 3, we saw that MEG exhibits intricate patterns arising from multiple layer moiré patterns and relative lattice strain. These superstructures contain useful information about the angular orientation of three or more layers. In the case of low angle moiré patterns, the amount of relative strain can even be estimated based on the distortion of the hexagonal superstructure. Low rotation angle superstructures ($\ll 1^\circ$) are especially sensitive in the low distortion regime, because the lattice vectors undergo angular rotations which are comparable to the size of the moiré rotation angle ($\theta$) and have large distortions in supercell length.

Spectroscopy of the local density of states in a magnetic field on multilayer epitaxial graphene has shown the graphene monolayer behavior. The $dI/dV$ spectra provide a direct measurement of the magnetic quantization expected for massless Dirac fermions. This implies that the topmost layer of epitaxial graphene closely approximates an isolated sheet of graphene, and can be attributed to the rotational misorientation between the layers, which preserves sublattice symmetries over the moiré superlattice cell.

We extended this measurement over two dimensions and observed spatial variations of the $N = 0$ LL. $\mathrm{LL}_0^{av}$ mostly follows the drift state picture, with the presence of localized and extended states found in maps at the tails and center of $\mathrm{LL}_0^{av}$, respectively. Closer analysis also revealed a subtle interaction from the moiré stacking. High magnetic fields can activate spatially separated gaps in the density of states when two stacked layers are rotationally stacked. This only arises when the magnetic field is high enough to reduce the size of the

wavefunctions below the size of the AB/BA-like regions. While for most rotation angles, this threshold magnetic field is relatively high, the large area moiré patterns ($\geq$ 50 nm) should produce gaps at magnetic fields accessible in ordinary quantum Hall measurements (5 – 10 T).

## *5.2 Further Considerations*

Our experimental evidence for spatially periodic lifting of the valley degeneracy in graphene's zero–Landau level has important implications for transport phenomena. This imposed periodicity could lead to a complex energy spectrum (*cf.,* the Hofstadter butterfly), and perhaps accounts for prior observations of fractal-like structure in magnetoresistance measurements of this material [Berger 2006]. The underlying physics discovered here may apply to other atomically-flat substrates or overlayers, and suggests that strain and accidental layer slip (e.g., at contacts) may be important to consider in measurements of nominally graphite-stacked graphene bilayers. The alternating pattern of AB- and BA-aligned regions in the moiré also implies that bands of the same energy have different valley symmetry in neighboring valley-split patches. With gate control of the carrier density, one could position the Fermi energy between the valley-split levels to create an interleaved graphene-like pattern of orthogonal Fermi fluids. The physics of both single-layer and interlayer correlations and coherence in such a system would be interesting.

# REFERENCES


[Alicea 2006] Jason Alicea and Matthew P. A. Fisher. *Graphene integer quantum Hall effect in the ferromagnetic and paramagnetic regimes*. Phys. Rev. B, vol. 74, no. 7, page 075422, 2006. 111

[Amidror 2003] I. Amidror. *Moire patterns between aperiodic layers: quantitative analysis and synthesis*. J. Opt. Soc. Am. A, vol. 20, no. 10, pages 1900–19, 2003. 66

[Ando 1984] Tsuneya Ando. *Electron Localization in a Two-Dimensional System in Strong Magnetic Fields. II: Long-Range Scatterers and Response Functions*. J. Phys. Soc. Jpn., vol. 53, no. 9, pages 3101–3111, 1984. 89

[Ando 1998] Tsuneya Ando, Takeshi Nakanishi and Riichiro Saito. *Berry's Phase and Absence of Back Scattering in Carbon Nanotubes*. J. Phys. Soc. Jpn., vol. 67, no. 8, pages 2857–2862, 1998. 5, 9

[Aoki 1985] Hideo Aoki and Tsuneya Ando. *Critical localization in two-dimensional Landau quantization*. Phys. Rev. Lett., vol. 54, no. 8, pages 831–834, Feb 1985. 99

[Ashcroft 1976] Neil W. Ashcroft and David N. Mermin. Solid state physics. Thomson Learning, Toronto, 1 édition, January 1976. 3

[Bae 2010] Sukang Bae, Hyeongkeun Kim, Youngbin Lee, Xiangfan Xu, Jae-Sung Park, Yi Zheng, Jayakumar Balakrishnan, Tian Lei, Hye Ri Kim, Young Il Song, Young-Jin Kim, Kwang S. Kim, Barbaros Ozyilmaz, Jong-Hyun Ahn, Byung Hee Hong and Sumio Iijima. *Roll-to-roll production of 30-inch graphene films for transparent electrodes*. Nature Nano, vol. 5, no. 8, pages 574–578, August 2010. 13

[Bardeen 1961] J. Bardeen. *Tunnelling from a Many-Particle Point of View*. Phys. Rev. Lett., vol. 6, no. 2, pages 57–59, Jan 1961. 24

[Berger 2004] Claire Berger, Zhimin Song, Tianbo Li, Xuebin Li, Asmerom Y. Ogbazghi, Rui Feng, Zhenting Dai, Alexei N. Marchenkov, Edward H. Conrad, Phillip N. First and Walt A. de Heer. *Ultrathin epitaxial graphite: 2D electron gas properties and a route toward graphene-based nanoelectronics*. J. Phys. Chem. B, vol. 108, no. 52, pages 19912–19916, 2004. 14

[Berger 2006] Claire Berger, Zhimin Song, Xuebin Li, Xiaosong Wu, Nate Brown, Cecile Naud, Didier Mayou, Tianbo Li, Joanna Hass, Alexei N. Marchenkov, Edward H. Conrad, Phillip N. First and Walt A. de Heer. *Electronic Confinement and Coherence in Patterned Epitaxial Graphene*. Science, vol. 312, no. 5777, pages 1191–1196, 2006. 14, 16, 17, 113

[Biasetto 2008] L. Biasetto, M. Manzolaro and A. Andrighetto. *Emissivity measurements of opaque gray bodies up to 2000 C by a dual-frequency pyrometer*. The European Physical Journal A - Hadrons and Nuclei, vol. 38, no. 2, pages 167–171, November 2008. 61

[Biedermann 2009] Laura B. Biedermann, Michael L. Bolen, Michael A. Capano, Dmitry Zemlyanov and Ronald G. Reifenberger. *Insights into few-layer epitaxial graphene growth on 4H-SiC(000[overline 1]) substrates from STM studies*. Phys. Rev. B, vol. 79, no. 12, page 125411, 2009. 64

[Binnig 1987] Gerd Binnig and Heinrich Rohrer. *Scanning tunneling microscopy—from birth to adolescence*. Rev. Mod. Phys., vol. 59, no. 3, pages 615–625, Jul 1987. 21

[Bolotin 2008] K.I. Bolotin, K.J. Sikes, Z. Jiang, M. Klima, G. Fudenberg, J. Hone, P. Kim and H.L. Stormer. *Ultrahigh electron mobility in suspended graphene*. Solid State Commun., vol. 146, no. 9-10, pages 351 – 355, 2008. 12, 13, 79

[Bolotin 2009] Kirill I. Bolotin, Fereshte Ghahari, Michael D. Shulman, Horst L. Stormer and Philip Kim. *Observation of the fractional quantum Hall effect in graphene*. Nature, vol. 462, no. 7270, pages 196–199, November 2009. 13, 90

[Bommel 1975] A.J. Van Bommel, J.E. Crombeen and A. Van Tooren. *LEED and Auger electron observations of the SiC(0001) surface*. Surf. Sci., vol. 48, no. 2, pages 463 – 472, 1975. 14

[Bostwick 2007] Aaron Bostwick, Taisuke Ohta, Thomas Seyller, Karsten Horn and Eli Rotenberg. *Quasiparticle dynamics in graphene*. Nature Phys., vol. 3, no. 1, pages 36–40, January 2007. 83

[Brar 2010] Victor W. Brar, Regis Decker, Hans-Michael Solowan, Yang Wang, Lorenzo Maserati, Kevin T. Chan, Hoonkyung Lee, Caglar O. Girit, Alex Zettl, Steven G. Louie, Marvin L. Cohen and Michael F. Crommie. *Gate-Controlled Ionization and Screening of Cobalt Adatoms on a Graphene Surface*, 2010. 97

[Brewer 1990] L. Brewer and R.H. Lamoreaux. Binary alloy phase diagrams. Materials Information Soc., Materials Park, Ohio, 1990. 57

[Bromley 1956] R H Bromley. *Two-dimensional Strain Measurement by Moiré*. Proc. Phys. Soc. B, vol. 69, no. 3, pages 373–381, 1956. 69

[Cambaz 2008] Z. Goknur Cambaz, Gleb Yushin, Sebastian Osswald, Vadym Mochalin and Yury Gogotsi. *Noncatalytic synthesis of carbon nanotubes, graphene and graphite on SiC*. Carbon, vol. 46, no. 6, pages 841 – 849, 2008. 73

[Castro Neto 2009] A. H. Castro Neto, F. Guinea, N. M. R. Peres, K. S. Novoselov and A. K. Geim. *The electronic properties of graphene*. Rev. Mod. Phys., vol. 81, no. 1, page 109, 2009. for a recent review. 108

[Checkelsky 2008] Joseph G. Checkelsky, Lu Li and N. P. Ong. *Zero-Energy State in Graphene in a High Magnetic Field*. Phys. Rev. Lett., vol. 100, no. 20, page 206801, 2008. 90

[Checkelsky 2009] Joseph G. Checkelsky, Lu Li and N. P. Ong. *Divergent resistance at the Dirac point in graphene: Evidence for a transition in a high magnetic field*. Phys. Rev. B, vol. 79, no. 11, page 115434, 2009. 90

[Chen 1993] C. Julian Chen. Introduction to scanning tunneling microscopy. Oxford University Press, Inc., 1993. 24, 32

[Chen 2008] Jian-Hao Chen, Chaun Jang, Shudong Xiao, Masa Ishigami and Michael S. Fuhrer. *Intrinsic and extrinsic performance limits of graphene devices on SiO2*. Nature Nano, vol. 3, no. 4, pages 206–209, April 2008. 1, 12

[Chhabra 1989] Ashvin Chhabra and Roderick V. Jensen. *Direct determination of the f($\alpha$) singularity spectrum*. Phys. Rev. Lett., vol. 62, no. 12, pages 1327–1330, Mar 1989. 99

[Chung 2001] Yip-Wah Chung. Practical guide to surface science and spectroscopy; electronic version. Elsevier, San Diego, CA, 2001. 54

[Cisternas 2008] Eduardo Cisternas, Marcos Flores and Patricio Vargas. *Superstructures in arrays of rotated graphene layers: Electronic structure calculations*. Phys. Rev. B, vol. 78, no. 12, page 125406, 2008. 69

[Davies 1998] John H. Davies. The physics of low-dimensional semiconductors : An introduction. Cambridge University Press, Cambridge, UK, 1998. 89

[de Heer 2007] Walt A. de Heer, Claire Berger, Xiaosong Wu, Phillip N. First, Edward H. Conrad, Xuebin Li, Tianbo Li, Michael Sprinkle, Joanna Hass, Marcin L. Sadowski, Marek Potemski and Grard Martinez. *Epitaxial graphene*. Solid State

Commun., vol. 143, no. 1-2, pages 92 – 100, 2007. Exploring graphene - Recent research advances. 14, 17, 81, 108

[Deacon 2007] R. S. Deacon, K.-C. Chuang, R. J. Nicholas, K. S. Novoselov and A. K. Geim. *Cyclotron resonance study of the electron and hole velocity in graphene monolayers*. Phys. Rev. B, vol. 76, no. 8, page 081406, Aug 2007. 81

[DiVincenzo 1984] D. P. DiVincenzo and E. J. Mele. *Self-consistent effective-mass theory for intralayer screening in graphite intercalation compounds*. Phys. Rev. B, vol. 29, no. 4, pages 1685–1694, Feb 1984. 3, 8

[Dombrowski 1999] R. Dombrowski, Chr. Steinebach, Chr. Wittneven, M. Morgenstern and R. Wiesendanger. *Tip-induced band bending by scanning tunneling spectroscopy of the states of the tip-induced quantum dot on InAs(110)*. Phys. Rev. B, vol. 59, no. 12, pages 8043–8048, Mar 1999. 97

[Dresselhaus 2002] M. S. Dresselhaus and G. Dresselhaus. *Intercalation compounds of graphite*. Adv. Phys., vol. 51, no. 1, pages 1–186, 2002. 111

[Du 2009] Xu Du, Ivan Skachko, Fabian Duerr, Adina Luican and Eva Y. Andrei. *Fractional quantum Hall effect and insulating phase of Dirac electrons in graphene*. Nature, vol. 462, no. 7270, pages 192–195, November 2009. 13, 90

[Emtsev 2009] Konstantin V. Emtsev, Aaron Bostwick, Karsten Horn, Johannes Jobst, Gary L. Kellogg, Lothar Ley, Jessica L. McChesney, Taisuke Ohta, Sergey A. Reshanov, Jonas Rohrl, Eli Rotenberg, Andreas K. Schmid, Daniel Waldmann, Heiko B. Weber and Thomas Seyller. *Towards wafer-size graphene layers by atmospheric pressure graphitization of silicon carbide*. Nature Mater., vol. 8, no. 3, pages 203–207, March 2009. 16

[Enachescu 1999] M. Enachescu, D. Schleef, D. F. Ogletree and M. Salmeron. *Integration of point-contact microscopy and atomic-force microscopy: Application to characterization of graphite/Pt(111)*. Phys. Rev. B, vol. 60, no. 24, pages 16913–16919, Dec 1999. 63

[Evers 2001] F. Evers, A. Mildenberger and A. D. Mirlin. *Multifractality of wave functions at the quantum Hall transition revisited*. Phys. Rev. B, vol. 64, no. 24, page 241303, Nov 2001. 99

[Fasolino 2007] A. Fasolino, J. H. Los and M. I. Katsnelson. *Intrinsic ripples in graphene*. Nature Mater., vol. 6, no. 11, pages 858–861, November 2007. 13

[Feldman 2009] Benjamin E. Feldman, Jens Martin and Amir Yacoby. *Broken-symmetry states and divergent resistance in suspended bilayer graphene*. Nature Phys., vol. 5, no. 12, pages 889–893, December 2009. 90

[First 2010] Phillip N. First, Walt A. de Heer, Thomas Seyller, Claire Berger, Joseph A. Stroscio and Jeong-Sun Moon. *Epitaxial Graphenes on Silicon Carbide*. MRS Bulletin, vol. 35, no. 4, pages 296–305, APR 2010. 14, 15, 81, 108

[Forbeaux 1998] I. Forbeaux, J.-M. Themlin and J.-M. Debever. *Heteroepitaxial graphite on* $6H-SiC(0001)$ *: Interface formation through conduction-band electronic structure*. Phys. Rev. B, vol. 58, no. 24, pages 16396–16406, Dec 1998. 14

[Fratini 2008] S. Fratini and F. Guinea. *Substrate-limited electron dynamics in graphene*. Phys. Rev. B, vol. 77, no. 19, page 195415, May 2008. 13

[Fuchs 2007] J. N. Fuchs and P. Lederer. *Charge density wave in graphene: Magnetic-field-induced Peierls instability*. Eur. Phys. J. Spec. Top., vol. 148, no. 1, pages 151–158, September 2007. 111

[Geim 2007] A. K. Geim and K. S. Novoselov. *The rise of graphene*. Nature Mater., vol. 6, no. 3, pages 183–191, March 2007. 12

[Goerbig 2009] M. O. Goerbig. *Quantum Hall Effects*, 2009. 7, 9, 89

[Guinea 2009] F. Guinea, Baruch Horovitz and P. Le Doussal. *Gauge fields, ripples and wrinkles in graphene layers*. Solid State Commun., vol. 149, no. 27-28, pages 1140 – 1143, 2009. Recent Progress in Graphene Studies. 13

[Hashimoto 2008] K. Hashimoto, C. Sohrmann, J. Wiebe, T. Inaoka, F. Meier, Y. Hirayama, R. A. Romer, R. Wiesendanger and M. Morgenstern. *Quantum Hall Transition in Real Space: From Localized to Extended States*. Phys. Rev. Lett., vol. 101, page 256802, 2008. 93

[Hass 2007] J. Hass, R. Feng, J. E. Millán-Otoya, X. Li, M. Sprinkle, P. N. First, W. A. de Heer, E. H. Conrad and C. Berger. *Structural properties of the multilayer graphene/4H-SiC(000[overline 1]) system as determined by surface x-ray diffraction*. Phys. Rev. B, vol. 75, no. 21, page 214109, 2007. 18

[Hass 2008a] J Hass, W A de Heer and E H Conrad. *The growth and morphology of epitaxial multilayer graphene*. J. Phys.: Condens. Matter, vol. 20, no. 32, page 323202, 2008. 15, 18, 110

[Hass 2008b] J. Hass, J. E. Millán-Otoya, P. N. First and E. H. Conrad. *Interface structure of epitaxial graphene grown on 4H-SiC(0001)*. Phys. Rev. B, vol. 78, no. 20, page 205424, Nov 2008. 16

[Hass 2008c] J. Hass, F. Varchon, J. E. Millan-Otoya, M. Sprinkle, N. Sharma, W. A. de Heer, C. Berger, P. N. First, L. Magaud and E. H. Conrad. *Why multilayer graphene on 4H-SiC(000$\bar{1}$) behaves like a single sheet of graphene*. Phys. Rev. Lett., vol. 100, no. 12, page 125504, March 2008. 19, 64, 91, 110

[Heinz 2000] K. Heinz, U. Starke, J. Bernhardt and J. Schardt. *Surface structure of hexagonal SiC surfaces: key to crystal growth and interface formation?* Applied Surface Science, vol. 162-163, pages 9 – 18, 2000. 16

[Henriksen 2008] E. A. Henriksen, Z. Jiang, L.-C. Tung, M. E. Schwartz, M. Takita, Y.-J. Wang, P. Kim and H. L. Stormer. *Cyclotron Resonance in Bilayer Graphene*. Phys. Rev. Lett., vol. 100, no. 8, page 087403, Feb 2008. 80

[Huckestein 1990] Bodo Huckestein and Bernhard Kramer. *One-parameter scaling in the lowest Landau band: Precise determination of the critical behavior of the localization length*. Phys. Rev. Lett., vol. 64, no. 12, pages 1437–1440, Mar 1990. 99

[Huckestein 1992] B. Huckestein, B. Kramer and L. Schweitzer. *Characterization of the electronic states near the centres of the Landau bands under quantum Hall conditions*. Surf. Sci., vol. 263, no. 1-3, pages 125 – 128, 1992. 99

[Huckestein 1995] Bodo Huckestein. *Scaling theory of the integer quantum Hall effect*. Rev. Mod. Phys., vol. 67, no. 2, pages 357–396, Apr 1995. 89, 98

[Jackson 1998] John D. Jackson. Classical electrodynamics third edition. Wiley, third édition, August 1998. 7

[Jiang 2007] Z. Jiang, Y. Zhang, H. L. Stormer and P. Kim. *Quantum Hall States near the Charge-Neutral Dirac Point in Graphene*. Phys. Rev. Lett., vol. 99, no. 10, page 106802, 2007. 89, 90

[Katsnelson 2006] M. I. Katsnelson, K. S. Novoselov and A. K. Geim. *Chiral tunnelling and the Klein paradox in graphene*. Nature Phys., vol. 2, no. 9, pages 620–625, September 2006. 5

[Kawai 2009] Shigeki Kawai and Hideki Kawakatsu. *Surface-relaxation-induced giant corrugation on graphite (0001)*. Phys. Rev. B, vol. 79, no. 11, page 115440, Mar 2009. 63

[Khveshchenko 2001] D. V. Khveshchenko. *Magnetic-Field-Induced Insulating Behavior in Highly Oriented Pyrolitic Graphite*. Phys. Rev. Lett., vol. 87, no. 20, pages 206401–, October 2001. 111

[Kindermann 2010] M. Kindermann and P. N. First. *Local sublattice-symmetry breaking in rotationally faulted multilayer graphene*. Phys. Rev. B, 2010. Submitted. 111

[Kittel 1996] Charles. Kittel. Introduction to solid state physics. John Wiley and Sons, New York, NY, USA, 7th édition, 1996. 70

[Krithivasan 2006] R. Krithivasan, Yuan Lu, J.D. Cressler, Jae-Sung Rieh, M.H. Khater, D. Ahlgren and G. Freeman. *Half-terahertz operation of SiGe HBTs*. IEEE Electron Device Letters, vol. 27, no. 7, pages 567 – 569, jul. 2006. 1

[Kubista 2011] Kevin Kubista. *Kubista Thesis*. PhD thesis, Georgia Institute of Technology, 2011. 83, 93

[Kuwabara 1990] M. Kuwabara, D. R. Clarke and D. A. Smith. *Anomalous superperiodicity in scanning tunneling microscope images of graphite*. Appl. Phys. Lett., vol. 56, no. 24, pages 2396–2398, 1990. 63, 66

[Kwon 2009] Soon-Yong Kwon, Cristian V. Ciobanu, Vania Petrova, Vivek B. Shenoy, Javier Bareño, Vincent Gambin, Ivan Petrov and Suneel Kodambaka. *Growth of Semiconducting Graphene on Palladium*. Nano Letters, vol. 9, no. 12, pages 3985–3990, December 2009. 13

[Lang 1986] N. D. Lang. *Spectroscopy of single atoms in the scanning tunneling microscope*. Phys. Rev. B, vol. 34, no. 8, pages 5947–5950, Oct 1986. 24

[Latil 2007] Sylvain Latil, Vincent Meunier and Luc Henrard. *Massless fermions in multilayer graphitic systems with misoriented layers: Ab initio calculations and experimental fingerprints*. Phys. Rev. B, vol. 76, no. 20, page 201402, 2007. 110

[Lee 2008] Changgu Lee, Xiaoding Wei, Jeffrey W. Kysar and James Hone. *Measurement of the Elastic Properties and Intrinsic Strength of Monolayer Graphene*. Science, vol. 321, no. 5887, pages 385–388, 2008. 2

[Li 2007] Guohong Li and Eva Y. Andrei. *Observation of Landau levels of Dirac fermions in graphite*. Nature Phys., vol. 3, no. 9, pages 623–627, September 2007. 19, 78, 80

[Li 2009a] Guohong Li, A. Luican, J. M. B. Lopes dos Santos, A. H. Castro Neto, A. Reina, J. Kong and E. Y. Andrei. *Observation of Van Hove singularities in twisted graphene layers*. Nature Phys., vol. advance online publication, pages –, November 2009. xiv, 74, 75, 95, 110

[Li 2009b] Xuesong Li, Weiwei Cai, Jinho An, Seyoung Kim, Junghyo Nah, Dongxing Yang, Richard Piner, Aruna Velamakanni, Inhwa Jung, Emanuel Tutuc, Sanjay K. Banerjee, Luigi Colombo and Rodney S. Ruoff. *Large-Area Synthesis of High-Quality and Uniform Graphene Films on Copper Foils*. Science, vol. 324, no. 5932, pages 1312–1314, 2009. 13

[Li 2010] X. Li, X. Wu, M. Sprinkle, F. Ming, M. Ruan, Y. Hu, C. Berger and W. A. de Heer. *Top- and side-gated epitaxial graphene field effect transistors*. Phys. Stat. Sol. (a), vol. 207, no. 2, pages 286–290, 2010. 15

[Lopes dos Santos 2007] J. M. B. Lopes dos Santos, N. M. R. Peres and A. H. Castro Neto. *Graphene Bilayer with a Twist: Electronic Structure*. Phys. Rev. Lett., vol. 99, no. 25, page 256802, Dec 2007. 19, 74, 83, 110

[Lui 2009] Chun Hung Lui, Li Liu, Kin Fai Mak, George W. Flynn and Tony F. Heinz. *Ultraflat graphene*. Nature, vol. 462, no. 7271, pages 339–341, November 2009. 2, 13

[Luican 2010] A. Luican, Guohong Li, A. Reina, J. Kong, R. R. Nair, K. S. Novoselov, A. K. Geim and E. Y. Andrei. *Single Layer Behavior and Its Breakdown in Twisted Graphene Layers*, 2010. 83, 84

[Luk'yanchuk 2008] Igor A. Luk'yanchuk and Alexander M. Bratkovsky. *Lattice-Induced Double-Valley Degeneracy Lifting in Graphene by a Magnetic Field*. Phys. Rev. Lett., vol. 100, no. 17, page 176404, 2008. 108

[Lundeberg 2010] Mark B. Lundeberg and Joshua A. Folk. *Rippled Graphene in an In-Plane Magnetic Field: Effects of a Random Vector Potential*. Phys. Rev. Lett., vol. 105, no. 14, page 146804, Sep 2010. 2

[MacDonald 1984] A. H. MacDonald and P. Středa. *Quantized Hall effect and edge currents*. Phys. Rev. B, vol. 29, no. 4, pages 1616–1619, Feb 1984. 88

[Marchini 2007] S. Marchini, S. Günther and J. Wintterlin. *Scanning tunneling microscopy of graphene on Ru(0001)*. Phys. Rev. B, vol. 76, no. 7, page 075429, 2007. 13

[Martin 2008] J. Martin, N. Akerman, G. Ulbricht, T. Lohmann, J. H. Smet, K. von Klitzing and A. Yacoby. *Observation of electron-hole puddles in graphene using a scanning single-electron transistor*. Nature Phys., vol. 4, no. 2, pages 144–148, February 2008. 12

[Martin 2009] J. Martin, N. Akerman, G. Ulbricht, T. Lohmann, K. von Klitzing, J. H. Smet and A. Yacoby. *The nature of localization in graphene under quantum Hall conditions*. Nature Phys., vol. 5, no. 9, pages 669–674, September 2009. 93, 108

[Matsui 2005] T. Matsui, H. Kambara, Y. Niimi, K. Tagami, M. Tsukada and Hiroshi Fukuyama. *STS Observations of Landau Levels at Graphite Surfaces*. Phys. Rev. Lett., vol. 94, no. 22, page 226403, Jun 2005. 78, 80

[McCann 2006] Edward McCann. *Asymmetry gap in the electronic band structure of bilayer graphene*. Phys. Rev. B, vol. 74, no. 16, page 161403, Oct 2006. 6

[Mele 2010] E. J. Mele. *Commensuration and interlayer coherence in twisted bilayer graphene*. Phys. Rev. B, vol. 81, no. 16, page 161405, Apr 2010. 20, 83, 110

[Miller 2009] David L. Miller, Kevin D. Kubista, Gregory M. Rutter, Ming Ruan, Walt A. de Heer, Phillip N. First and Joseph A. Stroscio. *Observing the Quantization of Zero Mass Carriers in Graphene*. Science, vol. 324, no. 5929, pages 924–927, May 2009. 3, 19, 82, 93, 110

[Miller 2010a] David L. Miller, Kevin D. Kubista, Gregory M. Rutter, Ming Ruan, Walt A. de Heer, Phillip N. First and Joseph A. Stroscio. *Structural analysis of multilayer graphene via atomic moiré interferometry*. Phys. Rev. B, vol. 81, no. 12, page 125427, Mar 2010. xix, 64, 109, 110

[Miller 2010b] David L. Miller, Kevin D. Kubista, Gregory M. Rutter, Ming Ruan, Walt A. de Heer, Markus Kindermann, Phillip N. First and Joseph A. Stroscio. *Real-space mapping of magnetically quantized graphene states*. Nature Phys., vol. 6, no. 10, pages 811–817, October 2010. 111

[Moon 2009] Moon. *Epitaxial-Graphene RF Field-Effect Transistors on Si-Face 6H-SiC Substrates*. IEEE Electron Device Letters, vol. 30, page 650, 2009. 15

[Morgenstern 2003a] M Morgenstern. *Probing the local density of states of dilute electron systems in different dimensions*. Surf. Rev. Lett., vol. 10, no. 6, pages 933–962, DEC 2003. 32

[Morgenstern 2003b] M. Morgenstern, J. Klijn, Chr. Meyer, D. Haude and R. Wiesendanger. *Visualizing the Influence of Interactions on the Nanoscale: Simple Electron Systems*. In P. M. Koenraad and M. Kemerink, editeurs, Scanning Tunneling Microscopy/Spectroscopy and Related Techniques: 12th International Conference, volume 696 of *AIP Conference Proceedings*, pages 11–19, Melville, NY, 2003. AIP. 78, 93

[Morgenstern 2003c] M. Morgenstern, J. Klijn, Chr. Meyer and R. Wiesendanger. *Real-Space Observation of Drift States in a Two-Dimensional Electron System at High Magnetic Fields*. Phys. Rev. Lett., vol. 90, no. 5, page 056804, Feb 2003. 93, 99, 100

[Nair 2008] R. R. Nair, P. Blake, A. N. Grigorenko, K. S. Novoselov, T. J. Booth, T. Stauber, N. M. R. Peres and A. K. Geim. *Fine Structure Constant Defines Visual Transparency of Graphene*. Science, vol. 320, no. 5881, pages 1308–, 2008. 1

[Nazin 2010] G. Nazin, Y. Zhang, L. Zhang, E. Sutter and P. Sutter. *Visualization of charge transport through Landau levels in graphene*. Nature Phys., vol. advance online publication, pages –, August 2010. 98

[N'Diaye 2008] Alpha T N'Diaye, Johann Coraux, Tim N Plasa, Carsten Busse and Thomas Michely. *Structure of epitaxial graphene on Ir(111)*. New J. Phys., vol. 10, no. 4, page 043033 (16pp), 2008. 13

[Niimi 2009] Y. Niimi, H. Kambara and Hiroshi Fukuyama. *Localized Distributions of Quasi-Two-Dimensional Electronic States near Defects Artificially Created at Graphite Surfaces in Magnetic Fields*. Phys. Rev. Lett., vol. 102, no. 2, page 026803, 2009. 93

[Nomura 2009] Kentaro Nomura, Shinsei Ryu and Dung-Hai Lee. *Field-Induced Kosterlitz-Thouless Transition in the N = 0 Landau Level of Graphene*. Phys. Rev. Lett., vol. 103, no. 21, page 216801, 2009. 108

[Novoselov 2004] K. S. Novoselov, A. K. Geim, S. V. Morozov, D. Jiang, Y. Zhang, S. V. Dubonos, I. V. Grigorieva and A. A. Firsov. *Electric Field Effect in Atomically Thin Carbon Films*. Science, vol. 306, no. 5696, pages 666–669, 2004. 12

[Novoselov 2005] K. S. Novoselov, A. K. Geim, S. V. Morozov, D. Jiang, M. I. Katsnelson, I. V. Grigorieva, S. V. Dubonos and A. A. Firsov. *Two-dimensional gas of massless Dirac fermions in graphene*. Nature, vol. 438, no. 7065, pages 197–200, November 2005. 12, 89, 90

[Novoselov 2007] Kostya Novoselov. *Graphene: Mind the gap*. Nature Mater., vol. 6, no. 10, pages 720–721, October 2007. 6

[Orlikowski 2000] Daniel Orlikowski, Marco Buongiorno Nardelli, J. Bernholc and Christopher Roland. *Theoretical STM signatures and transport properties of native defects in carbon nanotubes*. Phys. Rev. B, vol. 61, no. 20, pages 14194–14203, May 2000. 74

[Orlita 2008] M. Orlita, C. Faugeras, P. Plochocka, P. Neugebauer, G. Martinez, D. K. Maude, A.-L. Barra, M. Sprinkle, C. Berger, W. A. de Heer and M. Potemski. *Approaching the Dirac Point in High-Mobility Multilayer Epitaxial Graphene*. Phys. Rev. Lett., vol. 101, no. 26, pages 267601–4, December 2008. 14, 80

[Owman 1996] Fredrik Owman and Per Martensson. *The SiC(0001)*$6\sqrt{3} \times 6\sqrt{3}$ *reconstruction studied with STM and LEED*. Surf. Sci., vol. 369, no. 1-3, pages 126 – 136, 1996. 16

[Paillard 1998] Bruno Paillard, Ran Tang and Paul Rowntree. *Digital linearization and cancellation of capacitive coupling for a scanning tunneling microscope*. Review of Scientific Instruments, vol. 69, no. 4, pages 1770–1780, 1998. 44

[Pan 1999] S. H. Pan, E. W. Hudson and J. C. Davis. *[sup 3]He refrigerator based very low temperature scanning tunneling microscope*. Review of Scientific Instruments, vol. 70, no. 2, pages 1459–1463, 1999. 28

[Pan 2001] S. H. Pan, J. P. O'Neal, R. L. Badzey, C. Chamon, H. Ding, J. R. Engelbrecht, Z. Wang, H. Eisaki, S. Uchida, A. K. Guptak, K. W. Ng, E. W. Hudson, K. M. Lang and J. C. Davis. *Microscopic electronic inhomogeneity in the high-$T_c$ superconductor $Bi_2Sr_2CaCu_2O_{8+x}$*. Nature, vol. 413, no. 6853, pages 282–285, September 2001. 105

[Partoens 2006] B. Partoens and F. M. Peeters. *From graphene to graphite: Electronic structure around the K point*. Phys. Rev. B, vol. 74, no. 7, page 075404, 2006. 111

[Pong 2005a] Wing-Tat Pong, James Bendall and Colm Durkan. *Observation of Large-Scale Features on Graphite by Scanning Tunnelling Microscopy*. Jpn. J. Appl. Phys., vol. 44, no. 7B, pages 5443–5446, 2005. 64

[Pong 2005b] Wing-Tat Pong and Colm Durkan. *A review and outlook for an anomaly of scanning tunnelling microscopy (STM): superlattices on graphite*. J. Phys. D, vol. 38, no. 21, pages R329–R355, 2005. 19, 63, 65, 69, 91

[Poplavskyy 2009] O. Poplavskyy, M. O. Goerbig and C. Morais Smith. *Local density of states of electron-crystal phases in graphene in the quantum Hall regime*. Phys. Rev. B, vol. 80, no. 19, page 195414, 2009. 108

[Reddy 2006] C D Reddy, S Rajendran and K M Liew. *Equilibrium configuration and continuum elastic properties of finite sized graphene*. Nanotechnology, vol. 17, no. 3, page 864, 2006. 71

[Reich 2002] S. Reich, J. Maultzsch, C. Thomsen and P. Ordejón. *Tight-binding description of graphene*. Phys. Rev. B, vol. 66, no. 3, page 035412, Jul 2002. 4

[Reich 2004] S. Reich, C. Thomsen and Maultzsch J. Carbon nanotubes: Basic concepts and physical properties. Wiley, 2004. 5

[Reina 2009] Alfonso Reina, Xiaoting Jia, John Ho, Daniel Nezich, Hyungbin Son, Vladimir Bulovic, Mildred S. Dresselhaus and Jing Kong. *Large Area, Few-Layer Graphene Films on Arbitrary Substrates by Chemical Vapor Deposition*. Nano Letters, vol. 9, no. 1, pages 30–35, 2009. 14

[Riedl 2009] C. Riedl, C. Coletti, T. Iwasaki, A. A. Zakharov and U. Starke. *Quasi-Free-Standing Epitaxial Graphene on SiC Obtained by Hydrogen Intercalation*. Phys. Rev. Lett., vol. 103, no. 24, page 246804, Dec 2009. 17

[Rollings 2006] E. Rollings, G. H. Gweon, S. Y. Zhou, B. S. Mun, J. L. McChesney, B. S. Hussain, An. Fedorov, P. N. First, W. A. de Heer and A. Lanzara. *Synthesis and characterization of atomically thin graphite films on a silicon carbide substrate*. J. Phys. Chem Sol., vol. 67, no. 9-10, Sp. Iss. SI, pages 2172–2177, SEP-OCT 2006. 83

[Rong 1994] Zhao Y. Rong. *Extended modifications of electronic structures caused by defects: Scanning tunneling microscopy of graphite*. Phys. Rev. B, vol. 50, no. 3, pages 1839–1843, Jul 1994. 64

[Rutter 2007] G. M. Rutter, N. P. Guisinger, J. N. Crain, E. A. A. Jarvis, M. D. Stiles, T. Li, P. N. First and J. A. Stroscio. *Imaging the interface of epitaxial graphene with silicon carbide via scanning tunneling microscopy*. Phys. Rev. B, vol. 76, no. 23, page 235416, Dec 2007. 16

[Rutter 2008] G. M. Rutter, J. N. Crain, N. P. Guisinger, P. N. First and J. A. Stroscio. *Structural and electronic properties of bilayer epitaxial graphene*. J. Vac. Sci. Technol., vol. 26, no. 4, pages 938–943, 2008. 30, 68

[Sadowski 2006] M. L. Sadowski, G. Martinez, M. Potemski, C. Berger and W. A. de Heer. *Landau Level Spectroscopy of Ultrathin Graphite Layers*. Phys. Rev. Lett., vol. 97, no. 26, page 266405, 2006. 82

[Sadowski 2007] M.L. Sadowski, G. Martinez, M. Potemski, C. Berger and W.A. de Heer. *Magnetospectroscopy of epitaxial few-layer graphene*. Solid State Commun., vol. 143, no. 1-2, pages 123–125, July 2007. 19, 83

[Saito 2000] R. Saito, G. Dresselhaus and M. S. Dresselhaus. *Trigonal warping effect of carbon nanotubes*. Phys. Rev. B, vol. 61, no. 4, pages 2981–2990, Jan 2000. 5

[Semenoff 1984] Gordon W. Semenoff. *Condensed-Matter Simulation of a Three-Dimensional Anomaly*. Phys. Rev. Lett., vol. 53, no. 26, pages 2449–2452, Dec 1984. 3

[Shen 2009] T. Shen, J. J. Gu, M. Xu, Y. Q. Wu, M. L. Bolen, M. A. Capano, L. W. Engel and P. D. Ye. *Observation of quantum-Hall effect in gated epitaxial graphene grown on SiC (0001)*. Appl. Phys. Lett., vol. 95, no. 17, page 172105, 2009. 17

[Slonczewski 1958] J. C. Slonczewski and P. R. Weiss. *Band Structure of Graphite*. Phys. Rev., vol. 109, no. 2, pages 272–279, Jan 1958. 5

[Somorjai 1980] G. A. Somorjai. *Auger Electron Spectroscopy*. In Presented as an invited paper at the EXXON Conference on Surface Science, 1980. 54

[Song 2010] Young Jae Song, Alexander F. Otte, Young Kuk, Yike Hu, David B. Torrance, Phillip N. First, Walt A. de Heer, Hongki Min, Shaffique Adam, Mark D. Stiles, Allan H. MacDonald and Joseph A. Stroscio. *High-resolution tunnelling*

*spectroscopy of a graphene quartet*. Nature, vol. 467, no. 7312, pages 185–189, September 2010. 84

[Sprinkle 2009] M. Sprinkle, D. Siegel, Y. Hu, J. Hicks, A. Tejeda, A. Taleb-Ibrahimi, P. Le Fèvre, F. Bertran, S. Vizzini, H. Enriquez, S. Chiang, P. Soukiassian, C. Berger, W. A. de Heer, A. Lanzara and E. H. Conrad. *First Direct Observation of a Nearly Ideal Graphene Band Structure*. Phys. Rev. Lett., vol. 103, no. 22, page 226803, 2009. x, 14, 19, 20, 83, 110

[Sprinkle 2010] M. Sprinkle. *Epitaxial Graphene on Silicon Carbide: Low-vacuum Growth, Characterization, and Device Fabrication*. PhD thesis, Georgia Institute of Technology, 2010. 65, 77

[Starke 1999] U. Starke, J. Schardt, J. Bernhardt, M. Franke and K. Heinz. *Stacking Transformation from Hexagonal to Cubic SiC Induced by Surface Reconstruction: A Seed for Heterostructure Growth*. Phys. Rev. Lett., vol. 82, no. 10, pages 2107–2110, Mar 1999. 16

[Starke 2009] U. Starke and C. Riedl. *Epitaxial graphene on SiC(0001) and SiC(000-1): from surface reconstructions to carbon electronics*. J. Phys.: Condens. Matter, vol. 21, no. 13, page 134016, 2009. 16, 17

[Stroscio 1993] J. A. Stroscio. Scanning tunneling microscopy. Academic Press, Inc., 1993. 24

[Sun 2003] Hai-Lin Sun, Quan-Tong Shen, Jin-Feng Jia, Qing-Zhe Zhang and Qi-Kun Xue. *Scanning tunneling microscopy study of superlattice domain boundaries on graphite surface*. Surf. Sci., vol. 542, no. 1-2, pages 94 – 100, 2003. 64

[Sun 2010] Dong Sun, Charles Divin, Claire Berger, Walt A. de Heer, Phillip N. First and Theodore B. Norris. *Spectroscopic Measurement of Interlayer Screening in*

*Multilayer Epitaxial Graphene*. Phys. Rev. Lett., vol. 104, no. 13, page 136802, Apr 2010. 18, 82

[Tersoff 1985] J. Tersoff and D. R. Hamann. *Theory of the scanning tunneling microscope*. Phys. Rev. B, vol. 31, no. 2, pages 805–813, Jan 1985. x, 24, 25

[Tőke 2006] Csaba Tőke, Paul E. Lammert, Vincent H. Crespi and Jainendra K. Jain. *Fractional quantum Hall effect in graphene*. Phys. Rev. B, vol. 74, no. 23, page 235417, Dec 2006. 7, 9

[Torrance 2010] D. Torrance and P. N. First. *Kinetic growth modeling of epitaxial graphene on SiC*. 2010. In preparation. 16

[Trambly de Laissardiere 2010] G. Trambly de Laissardiere, D. Mayou and L. Magaud. *Localization of Dirac Electrons in Rotated Graphene Bilayers*. Nano Letters, vol. 10, no. 3, pages 804–808, 2010. PMID: 20121163. x, 18, 19, 83

[Trevisanutto 2008] Paolo E. Trevisanutto, Christine Giorgetti, Lucia Reining, Massimo Ladisa and Valerio Olevano. *Ab Initio GW Many-Body Effects in Graphene*. Phys. Rev. Lett., vol. 101, no. 22, page 226405, Nov 2008. 81

[Tromp 2009] R. M. Tromp and J. B. Hannon. *Thermodynamics and Kinetics of Graphene Growth on SiC(0001)*. Phys. Rev. Lett., vol. 102, no. 10, page 106104, Mar 2009. 16

[Van Hove 1953] Léon Van Hove. *The Occurrence of Singularities in the Elastic Frequency Distribution of a Crystal*. Phys. Rev., vol. 89, no. 6, pages 1189–1193, Mar 1953. 74

[Varchon 2008] François Varchon, Pierre Mallet, Laurence Magaud and Jean-Yves Veuillen. *Rotational disorder in few-layer graphene films on 6H-SiC(000-1): A*

*scanning tunneling microscopy study*. Phys. Rev. B, vol. 77, no. 16, page 165415, 2008. 64

[Wallace 1947] P. R. Wallace. *The Band Theory of Graphite*. Phys. Rev., vol. 71, no. 9, pages 622–634, May 1947. 2, 4

[Wu 2009] Xiaosong Wu, Yike Hu, Ming Ruan, Nerasoa K Madiomanana, John Hankinson, Mike Sprinkle, Claire Berger and Walt A. de Heer. *Half integer quantum Hall effect in high mobility single layer epitaxial graphene*. Appl. Phys. Lett., vol. 95, no. 22, page 223108, 2009. xvi, 17, 85, 88, 90

[Xhie 1993] J. Xhie, K. Sattler, M. Ge and N. Venkateswaran. *Giant and supergiant lattices on graphite*. Phys. Rev. B, vol. 47, no. 23, pages 15835–15841, Jun 1993. 63, 69

[Yang 2007] Kun Yang. *Spontaneous symmetry breaking and quantum Hall effect in graphene*. Solid State Commun., vol. 143, no. 1-2, pages 27–32, JUL 2007. 107

[Yoshioka 1998] D. Yoshioka. The quantum hall effect. Springer, 1998. 88

[Young 1966] Russell D. Young. *Field Emission Ultramicrometer*. Review of Scientific Instruments, vol. 37, no. 3, pages 275–278, 1966. x, 21, 22

[Young 1972] Russell Young, John Ward and Fredric Scire. *The Topografiner: An Instrument for Measuring Surface Microtopography*. Review of Scientific Instruments, vol. 43, no. 7, pages 999–1011, 1972. x, 21, 22

[Zhang 2005] Yuanbo Zhang, Yan-Wen Tan, Horst L. Stormer and Philip Kim. *Experimental observation of the quantum Hall effect and Berry's phase in graphene*. Nature, vol. 438, no. 7065, pages 201–204, November 2005. 12, 89, 90

[Zhang 2006] Y. Zhang, Z. Jiang, J. P. Small, M. S. Purewal, Y.-W. Tan, M. Fazlollahi, J. D. Chudow, J. A. Jaszczak, H. L. Stormer and P. Kim. *Landau-Level Splitting in*

*Graphene in High Magnetic Fields*. Phys. Rev. Lett., vol. 96, no. 13, page 136806, 2006. 90

[Zhao 2010] Y. Zhao, P. Cadden-Zimansky, Z. Jiang and P. Kim. *Symmetry Breaking in the Zero-Energy Landau Level in Bilayer Graphene*. Phys. Rev. Lett., vol. 104, no. 6, page 066801, Feb 2010. 90

# VITA

David Lee Miller was born in Akron, Ohio on the morning of April 20th, 1983. As a child, like most others his age, he was disinterested in academics. He preferred to spend his time building tree forts, lego castles, rubber band guns and tennis ball cannons; however, the spark of scientific curiosity was present at an early age. In class, he day-dreamed about what would happen if one continued to cut a piece of paper in half. Could a person continue to cut forever if they had small enough *scissors*? He was fascinated by images printed in his textbook from electron microscopes and the large size of the machines, often wondering what the world looked like on such small scales.

Eventually, his curiosity led him to excel in his high school physics course. His teacher, Dick Heckathorn, instructed the subject with excitement and the motivation to demonstrate all of the basic concepts of classical physics using hands-on experiments. Not knowing the career path of a physicist (other than teaching), he started an education in engineering the following year at Calvin College. While he enjoyed the subject, he aspired to understand the *why* behind many of the engineering practices and found himself back in physics as a major the following year. He learned from many great professors while at Calvin, and in 2005, graduated with honors with a Bachelors of Science in physics. He was given the opportunity to pursue graduate studies at the Georgia Institute of Technology starting in the fall semester of that same year.

It was after the first year of study at Georgia Tech that he joined the laboratory of Dr. Phillip First, finally gaining the opportunity to work with powerful microscopes like the ones he had learned about in elementary school. Later on, opportunity knocked and he spent several months at NIST, operating the low-temperature scanning tunneling microscope under the instruction of Dr. Joseph Stroscio. That time was extremely successful and

resulted in much of the data that is in this thesis.

After graduation, Lee will be accepting a postdoctoral fellowship from the National Research Council to pursue research with the Electronics and Electrical Engineering Laboratory (EEEL) at the National Institute of Standards and Technology (NIST) in Boulder, Colorado.